METHODOLOGIES AND APPLICATION DEVELOPMENT OF HIGH FIELD PELDOR FOR SPIN LABELLED PROTEINS

Johannes Erik McKay

A Thesis Submitted for the Degree of PhD
at the
University of St Andrews

2016

Methodologies and application development of high field PELDOR for spin labelled proteins

Johannes Erik McKay

University of
St Andrews

This thesis is submitted in partial fulfilment for the degree of PhD

at the

University of St Andrews

October 2015

ACKNOWLEDGEMENTS

This thesis has only been possible with the enthusiastic guidance of my supervisor Dr Graham Smith. He has challenged me to grow my understanding and research in an environment where no question was ever dismissed without thought. I would also like to thank Dr Hassane El Mkami and Dr David Norman for putting up with my questions, which often showed my Physicists understanding of Biology and Chemistry.

In this thesis two protein mutants are investigated, Vps75 and MscS. The sample chemistry and biology of the protein Vps75 was provided as part of a collaboration with the group of Dr David Norman and significantly by student Mr Michael Stevens at the University of Dundee. The sample chemistry and biology of the protein MscS was provided as part of a collaboration with the group of Prof James Naismith and significantly by post-doctoral researchers Dr Richard Ward and Dr Christos Pilotas. I give sincere thanks to all of the researchers who have allowed me to collaborate in their research, providing the samples and guidance which were vital to the work presented in this thesis.

Beyond the work presented in this thesis I have also been given the opportunity to expand my knowledge of millimetre wave instrumentation and for this I owe in addition to my supervisor huge thanks to Dr Duncan Robertson who has given excellent guidance.

I would like to thank those in the millimetre Wave & EPR group who made the last four years interesting, it will be hard to forget. They are owed thanks for putting up with my humour! In particular I would like to thank Dr Robert Hunter, Dr Scott Cassidy and Ms Claire Motion for letting me share an office and never severely objecting to my presence.

ABSTRACT

The function of a biological molecule is linked to its underlying structure, and determination of that structure can lead to significant insights into its function and how this is performed. There already exist a number of important tools in structural biology, however, the pulsed electron paramagnetic resonance (EPR) technique called pulsed electron-electron double resonance (PELDOR) is the only one capable of accurately measuring isolated distances between attached spin-labels over the range of ~2 to 10 nm, a range which is usually impossible to measure directly with other techniques such as nuclear magnetic resonance (NMR) and X-ray crystallography. This can provide constraints for refinement of structures determined from NMR and X-ray crystallography, or insights into protein docking and protein mechanics. With recent developments in EPR spectrometer instrumentation and spin-labelling it has become possible to conduct PELDOR experiments in the high field EPR regime (>3 Tesla) where measurement sensitivity is increased. These experiments can reveal relative orientations of nitroxide spin-labels in complement to their separation, however, analysis and interpretation of these results has been difficult to perform routinely.

This thesis presents a characterisation of the high field spectrometer HiPER showing that it is well suited when optimised for making PELDOR experiments. To perform analysis of PELDOR signals from this spectrometer custom signal simulation code has been written.

Two case studies are presented. The first relates to the use of the Rx spin label with the PELDOR experiment to derive orientation information from the spin labelled protein Vps75. The recently developed spin label Rx is proposed to attach more rigidly to underlying structure, offering potentially increased accuracy in determination of structure constraints and additional information about relative orientations of different structural features. An orientation selective PELDOR study is presented which compares molecular dynamics (MD) simulations of spin labels attached to sites on the α-helix of the protein Vps75. This has shown great potential for utilising the Rx spin label in a repeatable way on α-helix residue sites for determination of structural constraints.

The second case relates to orientation selective PELDOR measurements of spin labelled oligomeric membrane protein structures. High field PELDOR offers great potential in increasing measurement sensitivity and accuracy of structural constraints in oligomeric proteins. A methodology of signal analysis for this class of protein is presented along with measurements of the membrane channel protein MscS. Difficulties of PELDOR measurement on these labelled proteins are discussed and observed relaxation of the spin echo, relevant to pulsed EPR experiments, are investigated and possible mechanisms are presented.

Student's declaration

I, Johannes Erik McKay, hereby certify that this thesis, which is approximately 35,000 words in length, has been written by me, and that it is the record of work carried out by me, or principally by myself in collaboration with others as acknowledged, and that it has not been submitted in any previous application for a higher degree.

I was admitted as a research student in September 2011 and as a candidate for the degree of PhD in September 2012; the higher study for which this is a record was carried out in the University of St Andrews between 2011 and 2015.

Date 19/04/2015 signature of candidate ______________________

Supervisor's declaration

I hereby certify that the candidate has fulfilled the conditions of the Resolution and Regulations appropriate for the degree of PhD in the University of St Andrews and that the candidate is qualified to submit this thesis in application for that degree.

Date 19/04/2015 signature of supervisor ______________________

Permission for publication

In submitting this thesis to the University of St Andrews I understand that I am giving permission for it to be made available for use in accordance with the regulations of the University Library for the time being in force, subject to any copyright vested in the work not being affected thereby. I also understand that the title and the abstract will be published, and that a copy of the work may be made and supplied to any bona fide library or research worker, that my thesis will be electronically accessible for personal or research use unless exempt by award of an embargo as requested below, and that the library has the right to migrate my thesis into new electronic forms as required to ensure continued access to the thesis. I have obtained any third-party copyright permissions that may be required in order to allow such access and migration, or have requested the appropriate embargo below.

The following is an agreed request by candidate and supervisor regarding the publication of this thesis:

No embargo on print copy.
No embargo on electronic copy.

Date 19/04/2015 signature of candidate ____________________

Date 19/04/2015 signature of supervisor ____________________

TABLE OF ACRONYMS

CW: continuous wave

DEER: double electron-electron resonance

DQC: double quantum coherence

EIK: extended interaction klystron

EM: electro-magnetic

EPR: electron paramagnetic resonance

ESEEM: electron spin echo envelope modulation

FEP: fluorinated ethylene propylene

FID: free induction decay

GA: genetic algorithm

MD: molecular dynamics

MTSSL: methanethiosulfonate spin label

PELDOR: pulsed electron-electron double resonance

Q-factor: quality factor

SDSL:site directed spin labelling

Tm: spin echo phase memory time

W-band: waveguide band of 75 GHz to 110 GHz, with 94 GHz being the common centre frequency

X-band: waveguide band of 8.2 GHz to 12.4 GHz, with 9.4 GHz being the common centre frequency

Table of Contents

Chapter 1 INTRODUCTION

The function of a biological molecule is heavily linked to its underlying structure, and determination of that structure can lead to great insights into its function and how it is performed [1].

There already exist a number of tools, such as nuclear magnetic resonance (NMR), fluorescence resonance energy transfer (FRET) and X-ray crystallography to help understand or derive protein structures. However, the pulsed electron paramagnetic resonance (EPR) experiment pulsed electron-electron double resonance (PELDOR) is capable of accurately measuring separations between spin-labels attached to protein using site directed spin labelling (SDSL) techniques in the range of ~2 nm to 10 nm and in optimal conditions >10 nm.

This is a range which is usually impossible to measure directly and accurately with other techniques [2], with measurements being isolated to only the spin labels which are attached allowing for the targeting of particular structure components. This provides structure constraints that can refine existing models or give insights into protein docking or mechanics. The PELDOR technique has seen particular growth in application related to membrane protein structures, a challenging field where other techniques are often ineffective [3, 4].

The pulsed EPR experiment PELDOR method works by measuring the dipole-dipole coupling between clusters of paramagnetic electrons, in this work introduced by nitroxide spin labels. These spin labels can be attached by site specific labelling to protein molecules and the strength of the dipole-dipole interaction of these spin label has a separation and relative orientation dependence which can reveal information about the relative arrangement of the structure to which they are attached. However, these PELDOR experiments can only reveal relative orientation constraints of spin labels, in complement to the distance between them, when performed in the high magnetic field EPR regime (>3 Tesla) [5]. It is in the high field regime that the EPR spectrum of the spin label is broad enough, due to the anisotropic g-factor, that pulse excitations can excite particular orientations of the spin label in the magnetic field. Recent developments in EPR spectrometer instrumentation [6] and spin labelling techniques [7] mean it has become possible to conduct these experiments, with one such spectrometer being the W-band HiPER spectrometer at the University of St Andrews [8]. However, despite the improved measurement instrumentation and techniques the analysis and interpretation of PELDOR experiment results has been so far difficult to perform routinely.

In this work I have explored the application of the PELDOR experiment using high-field EPR for biological systems with the aim of better understanding the orientation information which can be obtained, and how best to routinely perform the experiments for reliably obtaining this information. The systems investigated include cases of the Rx spin label type attached to the dimer protein Vps75 and the MTSSL spin label attached to the oligomeric channel protein MscS.

1.1. CURRENT APPLICATIONS

1.1.1. EXPLORATION OF CURRENT PELDOR TECHNIQUES IN ANALYSIS OF SPIN LABEL DISTANCE AND ORIENTATION ANALYSIS OF TWO SPIN LABEL SYSTEMS

The first reported use of the PELDOR experiment was by Milov [9, 10] where the modulation of an electron spin echo from nearby dipole coupled radicals was achieved by the use of a secondary microwave field. Since that initial development there have been many experiments designed to measure the dipolar coupling between electron spins. The most widely used of these, and the pulse sequence used throughout this work, is the four pulse PELDOR sequence [11], and there have been several reviews and chapters discussing these pulse sequences and their development [2, 12, 13].

It has been of particular interest to characterise the application of the PELDOR experiment and refine analysis methods using model molecule systems. Model systems of two nitroxides have been measured using PELDOR to derive distances ranging from 1.4 nm to >5 nm corresponding to the molecular models with get accuracy [11, 14, 15]. It has also been shown that orientation selective PELDOR can reveal geometry of these model molecules

[16-18]. These measurements have validated the application of regularised fitting for distance distributions and also the general principle of deriving angle and distance geometry from the PELDOR signals.

Beyond model molecules the principle application of the PELDOR experiment has been the measurement of distances between spin label probes attached to protein molecules. The attachment of spin label probes to biomolecules has been advanced principally using nitroxide spin label [7, 19], principally using the spin label MTSSL [20], and has developed into the technique commonly referred to as SDSL. There are a wealth of other spin labels and labelling techniques developed which are working towards advancements in spin labelling biomolecules generally and to improve the quality of the EPR measurements, these have been discussed in several excellent reviews [7, 21-23]. Cases of particular interest to the author and this work include: increasing the spin echo coherence time [24-26], pulsed EPR measurement of spin labelled proteins at room-temperature [27-30], labelling of non-cysteine residues [31-34] and measurement of spin labelled protein in-cell [35-40].

There has also been significant interest and progress in developing rigid spin labels, where the spin label dynamics are dominated by the structure to which they are attached. These rigid labels have been developed for nucleic acid structure with EPR measurements showing the labels are rigid to their underlying structure [41]. For protein attachment spin labels based on the well-established MTSSL label have been developed [42, 43], with the Rx spin label being used in this work. The Rx spin label increases the spin label rigidity to the underlying structure by requiring two disulphide bonds to cysteine on the secondary structure.

Measurement of angles between spin labels with the PELDOR experiment has also become possible with the increased availability of high-field EPR spectrometers [44]. One particular challenge in developing a pulse EPR spectrometer for orientation selective PELDOR is the bandwidth needs to be comparable to the spectral width of the radical under study, which for a nitroxide spin label is ~400 MHz. This is difficult to achieve using a traditional EPR resonator, however, several techniques have been developed to overcome this by making the resonator have two tuneable resonances [45] or changing the magnetic field on a nanosecond timescale [46]. It is however also possible to use so-called non-resonant cavity based spectrometers [8, 47], with this work being conducted on the HiPER EPR spectrometer.

Orientation selective PELDOR measurements of biomolecules has been shown in the case of X-band, however, it was shown that the g-factor anisotropy was not well resolved at these fields and higher field studies are needed to solve for all of the relative angles [16, 48]. High field orientation selective PELDOR measurements and analysis showing orientation dependence has been made up to 263 GHz [17, 18, 49-53]. These orientation selective measurements have been made on model molecules, RNA, protein and membrane protein.

1.1.2. EXPLORATION OF CURRENT PELDOR TECHNIQUES IN ANALYSIS OF POLY SPIN LABELLED SYSTEMS IN DERIVING DISTANCES BETWEEN SPIN LABELS

The application of PELDOR measurements on clusters of >2 spins has been based on characterisation work on model molecules with up to 4 spins measured [54-56]. In a PELDOR study of a trimer model the relative angles between the spin labels were solved [57].

There has been several applications of PELDOR for the measurement of distances between multiple spin labels in proteins [3, 54, 58-61], particularly membrane proteins. Measurement of membrane proteins are often hindered by short phase memory times related to the model membrane, there has been interest in studying the influence of the model membrane on the relaxation times of the spin labels with studies comparing the different environments [62].

One problem with PELDOR measurement of poly spin molecules is the introduction of oscillations in the PELDOR signal which are mixing products of the dipolar coupling frequencies between the pairs within the system. These result in sum and difference frequencies which can cause significant artefacts in the analysis of these signals. It was found that by applying a power scaling correction to the signal proportional to the number of spins that these artefacts could be significantly reduced [63]. Other studies have shown that by careful measurement programs which reduce the fraction of spins in the molecule acted on by the pump pulse and purposely reducing the number of spins per molecule by under-labelling can also significantly suppress these artefacts [54, 64].

PELDOR studies of membrane proteins have despite the great difficulty of the PELDOR measurement and crystallisation have resolved the distances predicted in complement by x-ray crystallography [3, 65, 66], however, it has been observed that only the shortest distance could be resolved reliably in large oligomers inside membrane layers due to short phase memory times.

1.2. OVERVIEW

1.2.1. CHAPTER 2

This chapter provides an introduction to the fundamental EPR theory building up to a description of the PELDOR signals which are core to the work in this thesis. Presented also is an introduction to the hardware requirements and basic components needed for a high field pulsed EPR spectrometer suitable for the studies presented.

1.2.2. CHAPTER 3

To effectively analyse the PELDOR signals measured using the W-band EPR spectrometer HiPER [8] calibrations of the full bandwidth performance of the spectrometer needs to be made, and consideration made to the loading and arrangement of samples. A systematic exploration of the performance of the spectrometer was made, along with calibration measurements of the effective microwave magnetic field component across the full spectrometer bandwidth. Discussions and simulations of the performance of the sample tube materials and arrangements are presented, showing that fluorinated ethylene propylene (FEP) is a more effective material than standard EPR tubing made from quartz, which is more likely to introduce unpredictable reductions in the spectrometer's effective bandwidth.

1.2.3. CHAPTER 4

An overview of the PELDOR signal simulation codes used in the analysis of PELDOR experiments is presented, along with a generalised algorithm. Several optimizations were implemented to reduce computation time, and these are discussed.

1.2.4. CHAPTER 5

This chapter presents an investigation into modelling the conformation which the bipedal spin label Rx takes when attached to different attachment sites of the dimer protein Vps75. An analysis of molecular dynamics (MD) simulations of the spin label attached to the different sites was made to investigate suitability of the spin label for orientation selective PELDOR studies. W-band orientation PELDOR measurements were made and a model of the spin label conformation was fitted to these results. A comparison of the W-band PELDOR derived model was made to MD simulation models to provide insight into the predictability of the spin labelling along with validation of the measurement and analysis. The use of this orientation information as structural constraints is the important link between measurement and useful application to structural biology and is discussed

1.2.5. CHAPTER 6

The oligomeric protein systems MscS with 7 spin labels were measured and evidence of orientation information was revealed in the measurement, however strong relaxation and PELDOR signal distortions were observed. The effect and mitigation of the relaxation effect was explored by analysis of the signals compared to the fraction of the spin label spectrum excited and measurements of the spin echo phase memory time (Tm). Methodologies for the simulation and analysis of spin labelled cyclic symmetric oligomeric systems were developed and discussed. By applying these methods, in complement to experiment procedures which take into consideration the strong relaxation effects observed, it is possible to obtain orientation structural constraints from these systems.

Chapter 2 EPR THEORY AND INSTRUMENTATION

This chapter will overview the basic EPR theory building up to a fundamental description of the PELDOR experiment and the associated signal approximation used in the rest of the work. The origin of the orientation dependence on this signal will also be highlighted. There are many textbooks that explain in detail the principles of EPR and pulsed EPR spectroscopy, and the author finds particularly useful [13, 67, 68].

2.1. EPR BASICS

The origin of the resonance phenomenon that underpins EPR is the spin and angular momentum of the electron. This gives rise to a magnetic moment of an electron which can be expressed as

$$\boldsymbol{\mu} = \frac{q}{2m} \hbar \boldsymbol{S} \, .$$

Equation 2.1.1

The constant factors in this expression are often expressed as the Bohr magneton given by the expression

$$\beta_e = \frac{e\hbar}{2m_e} ,$$

Equation 2.1.2

this gives an expression for the magnetic moment of the electron

$$\boldsymbol{\mu_e} = -g\beta_e\boldsymbol{S}\,.$$

Equation 2.1.3

The factor g is a value given to relate the observed classical behaviour of the particle to its underlying quantum angular momentum quantum number. For a free electron this can be expressed as the constant g_e and is one of the most accurately determined physical constants. For an unpaired electron in a molecule the local environment can perturb this value from the constant g_e and is instead expressed as a g-tensor which is defined in its principal axis frame.

2.2. SPIN HAMILTONIAN

A brief overview and descriptions of the relevant spin Hamiltonian terms for this work will be presented here, however, a full description and treatment of the spin Hamiltonian can be found in many standard textbooks [13, 69].

Considering the interaction of the electron magnetic moment with a static magnetic field which will be expressed by the vector $\boldsymbol{B_0}$ the spin system energy can be described by the following static spin Hamiltonian

$$\boldsymbol{\mathcal{H}_0} = \beta_e\boldsymbol{B_0 g S}/\hbar + \tilde{\boldsymbol{S}}\boldsymbol{DS} + \sum_{k=1}^{m}\tilde{\boldsymbol{S}}\boldsymbol{A_k I_k} - \beta_n\sum_{k=1}^{m} g_{n\,k}\tilde{\boldsymbol{B}}_{\boldsymbol{0}}\boldsymbol{I_k}/\hbar + \sum_{I_k>1/2}\tilde{\boldsymbol{I}}_{\boldsymbol{k}}\boldsymbol{P_k I_k}$$

$$+\sum_{i\neq k}\tilde{\boldsymbol{I}}_{\boldsymbol{i}}\boldsymbol{d_{i,k} I_k}\,.$$

Equation 2.2.1

The first term in the Hamiltonian, $\beta_e \boldsymbol{B_0 g S}/\hbar$, is the electron Zeeman interaction, which relates to the interaction between the magnetic field $\boldsymbol{B_0}$ and the magnetic moment of the electron spin, where $\boldsymbol{S}$ is the electron spin operator.

The second term, $\boldsymbol{\tilde{S}DS}$, is the zero-field-splitting interaction of the electron spin system occurring when the electron spin system has a quantum number *S*>½ and to a first order relates to the dipole-dipole and exchange interaction between the electron spins in the same electron spin system. This interaction depends on whether the total spin number of unpaired electrons in the spin system is non-integer or integer. The resulting interaction is described by the zero-field-splitting interaction tensor $\boldsymbol{D}$.

The third term, $\sum_{k=1}^{m} \boldsymbol{\tilde{S}A_k I_k}$, is the electron-nuclear hyperfine interaction, which relates to the interaction couplings between the electron spin system to each of the connected nuclei $\boldsymbol{I_k}$, where $\boldsymbol{I_k}$ is the k'th nuclear spin operator, coupled by their associated hyperfine interaction tensor $\boldsymbol{A_k}$. The interaction has several mechanisms with the largest contributions being split into the isotropic Fermi contact and the dipole-dipole interaction. The isotropic part only has a significant contribution when the electron occupies the s orbital, where it has a probability of being at the same position as the nucleus, and is independent of the relative orientation relative to the magnetic field. The anisotropic dipole-dipole interaction has a dependence on the strength of their mutual dipole interaction meaning there will be a dependence on their relative orientation and distance separation.

The first three terms correspond to the electron spin interaction with: the surrounding static magnetic field, electron spins within the system and local nuclear spins. We can apply the same treatment to each of the local nuclei in the spin system.

Thus we find the fourth term, $\beta_n \sum_{k=1}^{m} g_{n\,k} \tilde{\boldsymbol{B}}_{\boldsymbol{0}} \boldsymbol{I_k}/\hbar$, is the nuclear Zeeman interaction relating to the interaction between each nuclei $\boldsymbol{I_k}$ and the magnetic field $\boldsymbol{B_0}$.

The fifth term, $\sum_{I_k>1/2} \tilde{\boldsymbol{I}}_{\boldsymbol{k}} \boldsymbol{P_k} \boldsymbol{I_k}$, is the nuclear quadrupole interaction which applies to each nuclear spin $\boldsymbol{I_k}$ that has a spin quantum number *I*>1 where the nuclei has an uneven charge distribution on its surface and the interaction is described by the interaction tensor $\boldsymbol{P_k}$.

The final term, $\sum_{i\neq k} \tilde{\boldsymbol{I}}_{\boldsymbol{i}} \boldsymbol{d_{i,k}} \boldsymbol{I_k}$, in the static spin Hamiltonian is the dipole-dipole interaction between each of the i'th and k'th nuclei, where the coupling is described by the interaction tensor $\boldsymbol{d_{i,k}}$.

Of particular interest in this work is the case of two electron spins which are weakly coupled to each other, ie not electron spins within the same spin system which would be described by an electron spin quantum number *S*>½ and require a description of the zero-field-splitting interaction mentioned - but rather unpaired electrons which are individually characterised by separate spin systems. In this case we designate the different electron spin vectors by subscripts $\boldsymbol{S_1}, \boldsymbol{S_2}, \boldsymbol{S_3}, \boldsymbol{etc}$ and their interactions are characterised by two interactions, exchange coupling with the interaction tensor $\boldsymbol{J}$ and electron-electron dipole-dipole coupling with the interaction tensor D_{ee}. We can now write a complete Hamiltonian for two weakly coupled electron spin systems as

$$\boldsymbol{\mathcal{H}_0(S_1, S_2)} = \boldsymbol{\mathcal{H}_0(S_1)} + \boldsymbol{\mathcal{H}_0(S_2)} + \boldsymbol{\mathcal{H}_J} + \boldsymbol{\mathcal{H}_{D_{ee}}} \, .$$

Equation 2.2.2

The Heisenberg exchange coupling interaction occurs when there is overlap in the electron orbitals such that the two electrons can exchange with each other and this can occur in molecules where the electrons are strongly delocalised or that the electrons are suitably close to each other, in the range of <1.5 nm. The exchange coupling Hamiltonian term can be written using the exchange coupling interaction tensor $\boldsymbol{J}$ as

$$\boldsymbol{\mathcal{H}_J} = \boldsymbol{S_1 J S_2} \, .$$

Equation 2.2.3

The electron-electron dipole-dipole coupling interaction is due to the interaction of the magnetic dipoles of each electron, and will be the dominant interaction under study in this work. The dipole-dipole coupling Hamiltonian term can be written using the dipole-dipole interaction tensor $\boldsymbol{D_{ee}}$ as

$$\boldsymbol{\mathcal{H}}_{\boldsymbol{D_{ee}}} = \boldsymbol{S_1 D_{ee} S_2}\ .$$

Equation 2.2.4

By considering the case of a classical magnetic dipole pair interacting we can derive the Hamiltonian for a pair of interacting magnetic dipoles. We begin with the classical expression for the vector potential of a magnetic dipole with the magnetic moment $\boldsymbol{\mu_1}$

$$\boldsymbol{A} = \frac{\mu_0}{4\pi}\frac{\boldsymbol{\mu_1} \times \boldsymbol{r}}{r^2}$$

Equation 2.2.5

From which we can then define the field that is associated with this potential by finding the gradient of the potential

$$\boldsymbol{B} = \boldsymbol{\nabla} \times \boldsymbol{A} = \frac{\mu_0}{4\pi}\frac{3(\boldsymbol{\mu_1}.\boldsymbol{r})\boldsymbol{r} - r^2\boldsymbol{\mu_1}}{r^5}\ .$$

Equation 2.2.6

This the interaction of another magnetic moment $\boldsymbol{\mu_2}$ with this field gives an interaction energy of

$$E_{dd} = -\boldsymbol{\mu_2}.\boldsymbol{B} = -\frac{\mu_0}{4\pi}\frac{3(\boldsymbol{\mu_1}.\boldsymbol{r})(\boldsymbol{r}.\boldsymbol{\mu_2}) - r^2(\boldsymbol{\mu_1}.\boldsymbol{\mu_2})}{r^5}\ .$$

Equation 2.2.7

We can then replace the magnetic dipole moments with the quantum mechanical operators such that we get the Hamiltonian for the electron-electron dipole-dipole interaction

$$\mathcal{H}_{D_{ee}} = -\frac{\mu_0\gamma_1\gamma_2\hbar}{4\pi r^3}\left(3(\boldsymbol{S_1}.\hat{\boldsymbol{r}})(\hat{\boldsymbol{r}}.\boldsymbol{S_2}) - (\boldsymbol{S_1}.\boldsymbol{S_2})\right).$$

Equation 2.2.8

The resulting Hamiltonian has a $1/_{r^3}$ dependence characteristic of the dipole-dipole interaction. If we were to now express the vector r in spherical coordinates $\boldsymbol{r} = (r_x, r_y, r_z) = (r\sin\theta\cos\phi\,, r\sin\theta\sin\phi\,, r\cos\theta)$ and simplify, we obtain the common result of the dipolar coupling term expressed using the 'dipolar alphabet'

$$\mathcal{H}_{D_{ee}} = \frac{\mu_0\gamma_1\gamma_2\hbar}{4\pi r^3}(\boldsymbol{A}+\boldsymbol{B}+\boldsymbol{C}+\boldsymbol{D}+\boldsymbol{E}+\boldsymbol{F})$$

Equation 2.2.9

$$\boldsymbol{A} = \boldsymbol{S_{1z}}\boldsymbol{S_{2z}}(1-3\cos^2\theta)$$

$$\boldsymbol{B} = -\frac{1}{4}[\boldsymbol{S_1}^+\boldsymbol{S_2}^- + \boldsymbol{S_1}^-\boldsymbol{S_2}^+](1-3\cos^2\theta)$$

$$\boldsymbol{C} = -\frac{3}{2}[\boldsymbol{S_1}^+\boldsymbol{S_{2z}} + \boldsymbol{S_{1z}}\boldsymbol{S_2}^+]\sin\theta\cos\theta\, e^{-i\phi}$$

$$\boldsymbol{D} = -\frac{3}{2}[\boldsymbol{S_1}^-\boldsymbol{S_{2z}} + \boldsymbol{S_{1z}}\boldsymbol{S_2}^-]\sin\theta\cos\theta\, e^{i\phi}$$

$$\boldsymbol{E} = -\frac{3}{4}\boldsymbol{S_1}^+\boldsymbol{S_2}^+\sin^2\theta\, e^{-2i\phi}$$

$$\boldsymbol{F} = -\frac{3}{4}\boldsymbol{S_1}^-\boldsymbol{S_2}^-\sin^2\theta\, e^{2i\phi}$$

Equation 2.2.10

If we consider the Hamiltonian for the electron-electron dipole-dipole interaction in isolation, we can see the action of each of the letters of the alphabet. An energy level diagram is shown in **Figure 2.2.1** for two spin $^1/_2$ with dipole-dipole coupling using the basis set $|\boldsymbol{\alpha\alpha}\rangle$, $|\boldsymbol{\alpha\beta}\rangle$, $|\boldsymbol{\beta\alpha}\rangle$ & $|\boldsymbol{\beta\beta}\rangle$ which correspond to the two states which each electron can take $\boldsymbol{\alpha}$ and $\boldsymbol{\beta}$ corresponding to 'spin up' and 'spin down' and the four permutations of these states.

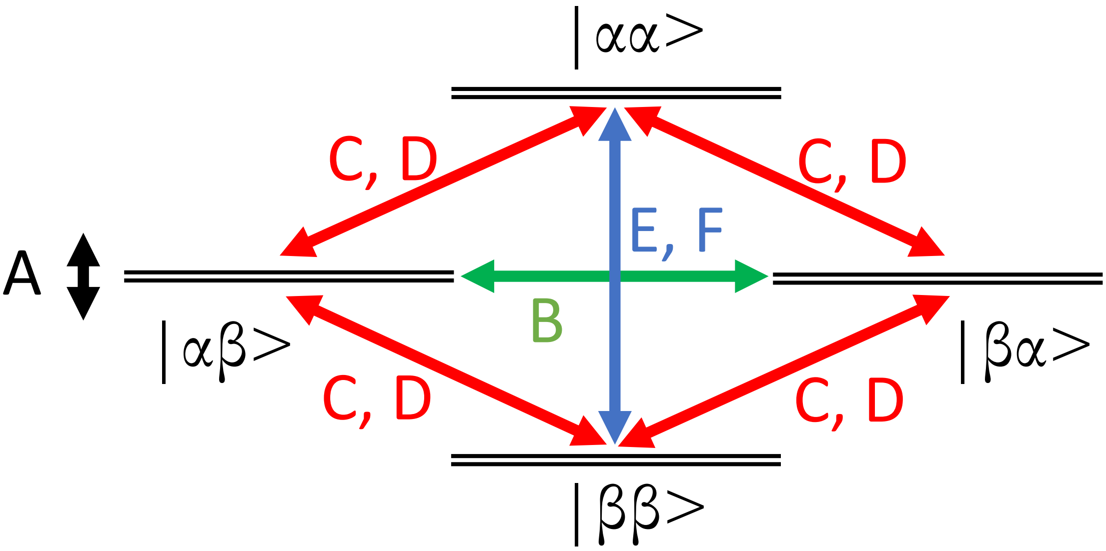

Figure 2.2.1 *Energy level diagram of two spin ½ with dipolar coupling. Each level is split according to the A term of the dipolar alphabet (**Equation 2.2.10**) and each of the other terms can lead to manipulation of the spin system as indicated by the arrows.*

The ***A*** term represents the dipolar coupling energy in the system, and each EPR line will split into a doublet with a separation equal to the energy ***A***. The ***B*** term as shown has the action of a mutual spin flip-flop where the states of each spin flips together. A measureable probability of this ***B*** term process requires a small difference in the Zeeman energies of each spin and a dipolar coupling energy comparable to this difference in Zeeman energies. For the case of dipole coupled nitroxide spin labels at W-band EPR (3.3 Tesla) this term is normally insignificant. This is due to the spectral width of nitroxide spin labels being ~400 MHz and a typical spin separation of >2 nm which corresponds to a dipolar coupling strength of <6 MHz. This makes the condition of dipolar coupling being comparable to the Zeeman energy difference unlikely. The $\boldsymbol{C}, \boldsymbol{D}$ terms lead to a spin flip of one or other of the spins and this process can only have a significant probability if the strength of the dipole-dipole coupling energy is close to the energy of the Zeeman interaction energy. The $\boldsymbol{E}, \boldsymbol{F}$ terms lead to spin flips of both the spins states, where again the process can only have significant probability if the strength of the dipole-dipole coupling energy is close to the energy of the Zeeman interaction. For the application of W-band EPR, the Zeeman energy is very much greater than the relevant dipolar coupling energies and the $\boldsymbol{C}, \boldsymbol{D}, \boldsymbol{E}, \boldsymbol{F}$ terms can be neglected. The $\boldsymbol{B}$ term can also be neglected in most cases of the nitroxide spin label, although careful consideration should be given to this term if there are spin labels with rigid orientation which can lead to comparable Zeeman interaction energies and cases where there is strong dipolar coupling energy.

In this work the systems studied have no electron orbital overlap and are weakly dipole coupled such that the Hamiltonian we are now left with is

$$\boldsymbol{\mathcal{H}_0}(\boldsymbol{S_1},\boldsymbol{S_2}) = \boldsymbol{\mathcal{H}_0}(\boldsymbol{S_1}) + \boldsymbol{\mathcal{H}_0}(\boldsymbol{S_2}) + \boldsymbol{\mathcal{H}_{D_{ee}}} \; .$$

Equation 2.2.11

The $\boldsymbol{\mathcal{H}_0}$ Hamiltonian will include any relevant electron-nuclear hyperfine coupling interactions. We can thus express a single Zeeman energy for each of the spins as ω_1 and ω_2. Based on the discussion so far we can write the dipolar coupling Hamiltonian as

$$\boldsymbol{\mathcal{H}_{D_{ee}}} = \frac{\mu_0\gamma_1\gamma_2\hbar}{4\pi r^3}(1-3\cos^2\theta)\left(\boldsymbol{S_{1z}}\boldsymbol{S_{2z}} - \frac{1}{4}[\boldsymbol{S_1}^+\boldsymbol{S_2}^- + \boldsymbol{S_1}^-\boldsymbol{S_2}^+]\right)$$

Equation 2.2.12

and the full relevant Hamiltonian as

$$\boldsymbol{\mathcal{H}_0}(\boldsymbol{S_1},\boldsymbol{S_2}) = \omega_1\boldsymbol{S_{1z}} + \omega_2\boldsymbol{S_{2z}} + \omega_{DD}\boldsymbol{S_{1z}}\boldsymbol{S_{2z}} - \frac{1}{4}\omega_{DD}[\boldsymbol{S_1}^+\boldsymbol{S_2}^- + \boldsymbol{S_1}^-\boldsymbol{S_2}^+]$$

Equation 2.2.13

where

$$\omega_{DD} = \frac{\mu_0\gamma_1\gamma_2\hbar}{4\pi r^3}(1-3\cos^2\theta)$$

Equation 2.2.14

We can also write this Hamiltonian in matrix form using again the basis set $|\boldsymbol{\alpha\alpha}\rangle$, $|\boldsymbol{\alpha\beta}\rangle$, $|\boldsymbol{\beta\alpha}\rangle$ & $|\boldsymbol{\beta\beta}\rangle$. We can calculate the different operators for the system of two spin ½ electrons by the application of tensor operators. First we express the Zeeman interaction with the following matrix

$$\boldsymbol{\mathcal{H}_0(S_1)} + \boldsymbol{\mathcal{H}_0(S_2)} = \frac{1}{2}\begin{pmatrix} \omega_1 + \omega_2 & 0 & 0 & 0 \\ 0 & \omega_1 - \omega_2 & 0 & 0 \\ 0 & 0 & -\omega_1 + \omega_2 & 0 \\ 0 & 0 & 0 & -\omega_1 - \omega_2 \end{pmatrix}$$

,

Equation 2.2.15

the dipolar coupling Hamiltonian with the following matrix

$$\boldsymbol{\mathcal{H}_{D_{ee}}} = \frac{1}{4}\begin{pmatrix} \omega_{DD} & 0 & 0 & 0 \\ 0 & -\omega_{DD} & -\omega_{DD} & 0 \\ 0 & -\omega_{DD} & -\omega_{DD} & 0 \\ 0 & 0 & 0 & \omega_{DD} \end{pmatrix},$$

Equation 2.2.16

and is combined to give the complete weak dipolar coupled Hamiltonian for two spin ½ electrons in matrix form

$$\boldsymbol{\mathcal{H}_0(S_1, S_2)} = \frac{1}{4}\begin{pmatrix} 2(\omega_1 + \omega_2) + \omega_{DD} & 0 & 0 & 0 \\ 0 & 2(\omega_1 - \omega_2) - \omega_{DD} & -\omega_{DD} & 0 \\ 0 & -\omega_{DD} & 2(-\omega_1 + \omega_2) - \omega_{DD} & 0 \\ 0 & 0 & 0 & 2(-\omega_1 - \omega_2) + \omega_{DD} \end{pmatrix}$$

Equation 2.2.17

There are several interesting observations which can be seen from this spin Hamiltonian matrix. First is the explicit illustration of the conditions for which the $\boldsymbol{B}$ term of the dipolar alphabet is contributing to the spin pair Hamiltonian. The $\boldsymbol{B}$ term of the dipolar alphabet contributes off-diagonal ω_{DD} terms, which when applying the secular approximation only remain if the value of ω_{DD} is comparable to the on-diagonal terms it is connecting, which in this case is the difference in Zeeman energies of the two spins $|\omega_1 - \omega_2|$ as discussed earlier. The second is that if we are only looking at allowed transitions, where the electron spin quantum number is only changing by ± 1, known as single quantum transitions, then we observe resonance lines at ω_1 and ω_2 which are both split into doublets where the splitting is $\pm\omega_{DD}$ as shown in **Figure 2.2.2**. It is often the case that the angle θ which is the angle between the vector connecting the two electrons and the static magnetic field, for which the value of ω_{DD} depends, is randomly orientated in the sample. This results in the splitting taking on a spherically averaged distribution commonly referred to as the Pake pattern rather than a simple doublet.

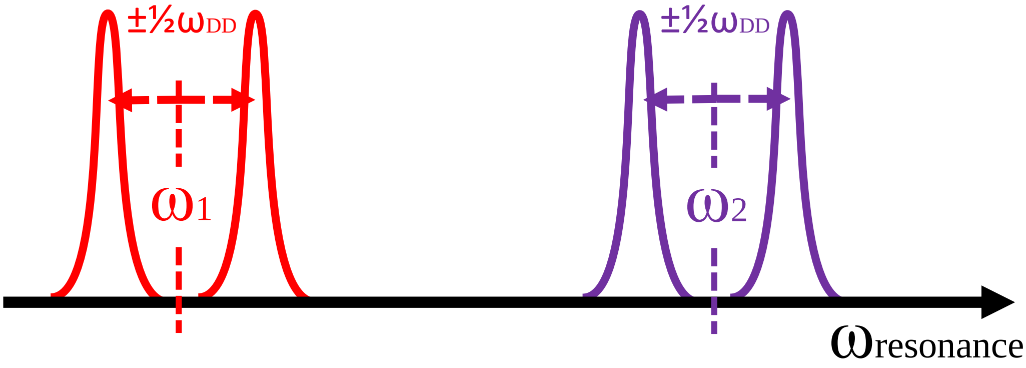

Figure 2.2.2 *Illustration of the doublet splitting of a single EPR line due to dipolar coupling.The resonances for two spin ½ are shown in red and purple, where they are split into a doublet by their mutual dipolar coupling.*

2.3. PULSED EPR EXPERIMENTS FOR MEASURING DIPOLAR COUPLING

We can observe from the dipole coupled spin pair Hamiltonian as derived in the previous chapter 2.2 that the dipolar coupling energy has a $1/_{r^3}$

dependence, such that if the ω_{DD} energy term can be measured we can obtain the distance between the electrons. It is the possibility to provide the distance between unpaired electrons in the 2-10 nm range that has particular interest for structural biology problems. Several pulsed EPR experiments have been developed to derive the dipolar coupling energy.

The most basic experiment is the use of continuous wave (CW) EPR to try to probe the dipolar broadening of the resonance lines, however for most dipolar coupling energies corresponding to inter-electron separations of over 2 nm the dipolar broadening is small compared with other broadening contributions to the resonance line width and the dipolar coupling broadening will be masked. These other broadening contributions can include an anisotropic g-factor tensor or hyperfine coupling tensor, which were introduced earlier. Thus the applicability of the CW dipolar coupling energy measurement is limited to electrons that are separated by less than 2 nm.

Pulsed EPR methodologies which overcome this restriction include the 2+1 experiment, the double quantum coherence (DQC) experiment and PELDOR also known as double electron-electron resonance (DEER). This work will concentrate on the application of the PELDOR experiment, however the other experiments will be introduced.

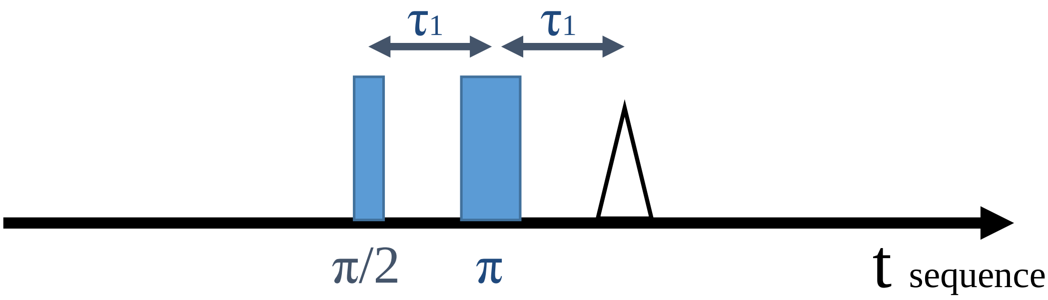

Figure 2.3.1 *Spin echo pulse sequence. The first $\pi/2$ pulse generates spin coherence which evolves for time τ_1 until a π pulse refocussed the coherence to produce a spin echo at a time τ_1 after the last pulse.*

It is also worth making the observation that the dipolar coupling ω_{DD} can sometimes be measured directly on the primary spin echo [70], **Figure 2.3.1**, under the conditions that both coupled electrons are excited by the pulses. The origin of the signal is due to dephasing of the spin packets contributing to the echo due to the mutual dipolar coupling of the spins. In this way we would expect to see a signal which has the form

$$V(t) = 2\cos(2\omega_{DD}\tau_1)\ .$$

Equation 2.3.1

However this direct measurement of the dipolar coupling in the primary echo requires that we excite many of the electron pairs with the same pulse sequence, and that any other effects contributing towards the dephasing of the electron spin does not mask the modulation effect. However, it is often the case that there are more significant dephasing mechanisms than the dipolar coupling such as coupling to surrounding nuclei, making the dipolar coupling contribution very difficult to measure from this experiment.

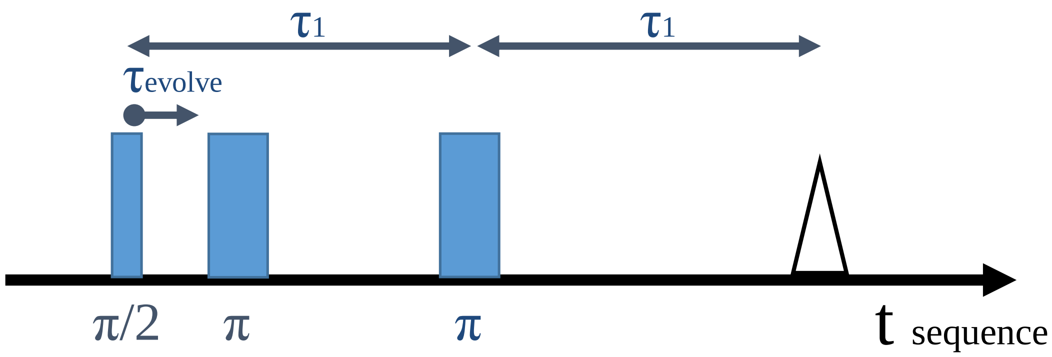

Figure 2.3.2 *2+1 pulse experiment sequence. The first π/2 pulse generates spin coherence which evolves for time* τ_{evolve} *until a π pulse causes spin flips which introduce a reversing of the dipolar coupling and introduces a dephasing of the spin echo proportional to* τ_{evolve} *and the dipolar coupling. The coherence continues to evolve until the final π pulse refocussed the coherence to produce a spin echo at a time* τ_1 *after the last pulse.*

The 2+1 experiment [71], **Figure 2.3.2**, is a single microwave frequency pulsed experiments which probes the dipolar coupling between electrons. The sequence uses a single common pulse frequency ω_{mw1} and has similarity to the primary spin echo sequence. The principle is to excite coherence in one of the electron spins with the initial π/2 pulse, which we will call the A spin. This spin is then allowed to evolve for some time, shown as τ_{evolve}, after which an additional π pulse is applied. Ideally this π pulse would only act on the partner electron spin to the one which the π/2 pulse acted, which we will call the B spin. However, because the sequence is applied at the same microwave frequency a compromise must be made and instead of a π pulse a smaller than π flip angle is commonly used. This results in an inefficient pulse operator acting on the A spin but still acting enough on the B spin such that the electron spin is 'flipped' and the dipolar coupling phase is reversed. To resolve the ω_{DD} coupling this pulse is stepped at small intervals relative to the initial π/2 pulse such that the dephasing accumulated due to the dipolar coupling is varied resulting in the final echo being modulated by the dipolar coupling as a function of the delay between the first and second pulse. The final π pulse is applied at a fixed time after the initial $\pi/2$ pulse and acts to refocus the coherence evolved in the A spin such that it can be observed as a spin echo $\tau1$ after the final pulse. The advantage of this sequence over the simple primary echo sequence is that the time between the $\pi/2$ coherence generating pulse and the final π refocus pulse is fixed, and this makes the modulation of the spin echo independent of other dephasing relaxation which was discussed as a hindrance to the detection of the dipolar coupling by the spin echo sequence. It has been shown that the optimal flip angles are for the first and third pulse to have the same flip angle and for the second pulse to be $2\pi/3$.

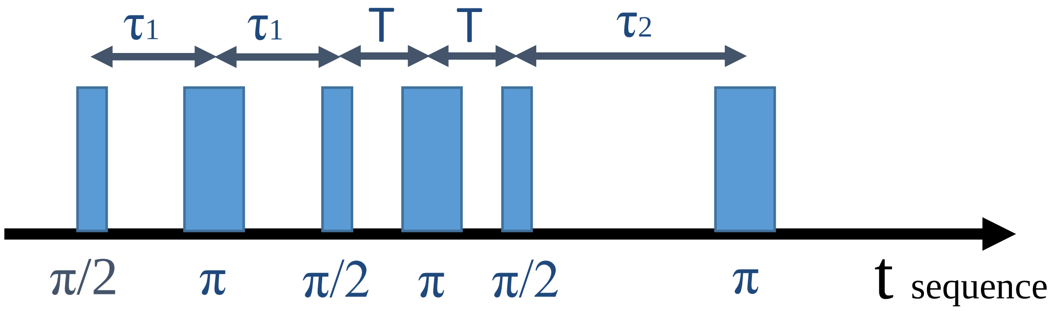

Figure 2.3.3 *DQC pulse experiment sequence. The pulse sequence is single frequency and transfers spin echo coherence into the double quantum transition where the evolution in higher order coherence filters other coherence pathways not created by the electron-electron dipole interation.*

The DQC experiment [72] is another single frequency pulsed experiment for probing dipolar coupling and is commonly performed as a 6 pulse EPR experiment where the microwave source with frequency ω_{mw1} is common to all of the pulses. The pulse sequence is shown in **Figure 2.3.3**. This sequence differs significantly from the previously mentioned experiments and the action of the different pulses will be discussed. The initial $\pi/2$ pulse generates coherence that is allowed to evolve for a time τ_1 before a π pulse is applied to refocus this coherence at a time τ_1 after the π pulse. After the refocussing $\pi/2$-π-$\pi/2$ pulses are applied and the action of these pulses is to transfer coherence generated by the first $\pi/2$ pulse to the double quantum transitions, between the spin states $|\boldsymbol{\alpha\alpha}\rangle$ & $|\boldsymbol{\beta\beta}\rangle$, the π pulse refocuses this evolution and the following $\pi/2$ pulse transfers this coherence back into detectable single quantum coherence again. The coherence will continue to evolve as single quantum coherence until a π pulse is applied to refocus the coherence as an observable echo. The $\pi/2$- π- $\pi/2$ sequence acts as a double quantum filter which isolates the electron spin pair dipolar coupling contribution from other single quantum signal contributions.

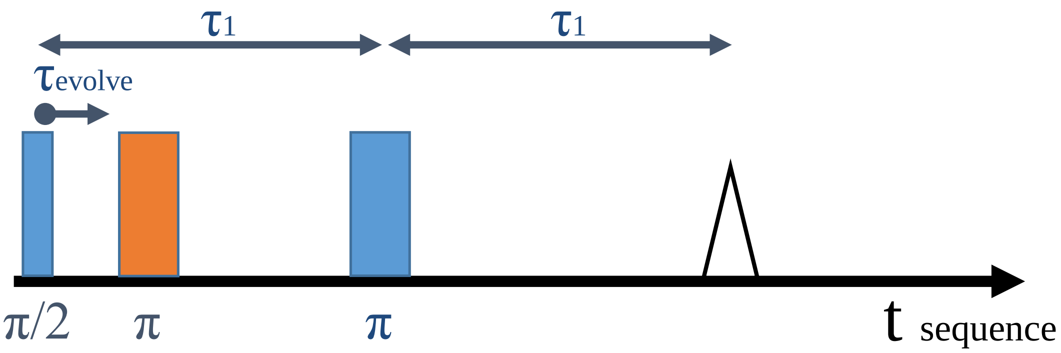

Figure 2.3.4 *3-pulse PELDOR experiment sequence. The first $\pi/2$ pulse generates spin coherence which evolves for time τ_{evolve} until a π pulse causes spin flips which introduce a reversing of the dipolar coupling and introduces a dephasing of the spin echo proportional to τ_{evolve} and the dipolar coupling strength. The coherence continues to evolve until the final π pulse refocussed the coherence to produce a spin echo at a time τ_1 after the last pulse.*

In the 2+1 sequence, where the dipolar coupling interaction is isolated by keeping the spin echo π/2 and π pulse sequence fixed and introducing an additional π dephasing pulse, the π dipolar dephasing pulse had the problem that it acts on both the spin A and spin B. This problem is addressed with the 3-pulse PELDOR experiment [73], **Figure 2.3.4**, where the π dipolar dephasing pulse is now applied at a separate microwave frequency from the spin echo sequence. Provided that the resonance of the two electron spins spectrum is broader than the pulse excitation bandwidth such that the resonance of the electron spin A different from spin B then in most cases individual pulses will excite different spins with reasonable probability. If the spin resonance between the two spins is uncorrelated such that there is an occasion when the pulses act on different combinations of spin A and B then the experiment can be more complicated, and this has been discussed extensively in recent publications [74, 75].

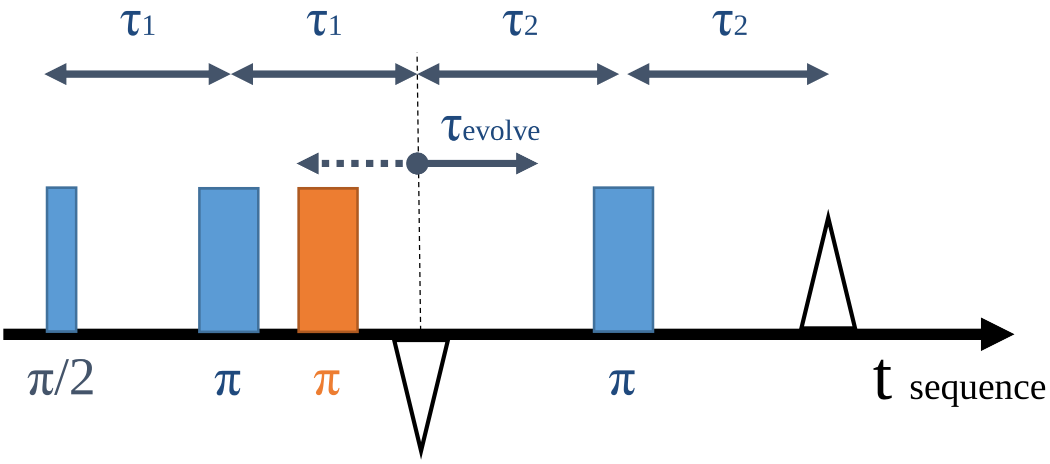

Figure 2.3.5 *4-pulse PELDOR experiment sequence. The first $\pi/2$ pulse generates spin coherence of spin A which evolves for time τ_1 until a π pulse refocuses the coherence at a time τ_1 after the pulse which moves the 'zero time of coherence evolution'. Another π pulse generated at another microwave frequency causes selective spin flips on spin B which introduce a reversing of the dipolar coupling on the coherence of spin A and introduces a dephasing of the spin A echo proportional to τ_{evolve} away from 2 τ_1 and the dipolar coupling strength. The coherence continues to evolve until the final π pulse refocussed the coherence to produce a spin echo at a time τ_2 after the last pulse.*

The 4-pulse PELDOR experiment [11], **Figure 2.3.5**, is a further expansion upon the 3-pulse PELDOR experiment where there is an additional refocus π pulse placed such that the time of 'zero' evolution is moved from being immediately after the initial π/2 pulse to being τ1 after the first refocus π pulse. This makes the sequence 'dead-time free', as the simpler 3-pulse sequence suffers from not being able to measure the very initial dipolar modulated evolution times due to technical and experimental problems of having the initial π/2 and 'pump' π pulse close together.

As the main concentration of this work is the application of the four pulse PELDOR experiment, hereafter referred to as the PELDOR sequence, and this experiment will now be discussed in more detail.

2.4. PELDOR EXPERIMENT AND ORIENTATION EFFECTS

The PELDOR signal arises from the echo of one electron spin, generated by the observer echo sequence, being modulated by the dipolar coupling between that spin and any other nearby electron spin which is excited by the pump pulse. The modulation of the echo is due to the change in magnetic field seen by the observer spin, caused by the dipolar field between the two spin being reversed by flipping of the pump spin, causing a dephasing of the echo and reducing the echo amplitude proportional to the time of the pump pulse after zero time of the echo evolution. It is common, and for simplified analysis it is preferable, for each molecule in a sample to have only two unpaired electrons with a defined dipolar coupling. In a dilute sample there will be a concentration of pairs in a volume which defines how many molecules there are in a given volume, often given in the unit of μmol/L. The concentration is sometimes given as a so called spin-concentration where it is the total number of unpaired electron spin in a given volume, again often given in the unit of μmol/L. Thus for a given sample of electron spin pairs with a particular concentration there will be a PELDOR signal associated with the defined dipolar coupling between the spin pairs but also from the distribution of dipolar couplings between spins in each of the near-by molecules. This distribution of dipolar couplings will depend on the concentration of electron spins and the geometry of the wider system, where the geometry is often simplified to a given dimensionality, e.g. planar or homogenous in three-dimensions. We can thus express our PELDOR signal as a product of these two components

$$I_{PELDOR}(t) = I_{inter}(t) \times I_{intra}(t) \ ,$$

Equation 2.4.1

where $I_{inter}(t)$ is the signal component from inter-molecule (between molecules) dipolar couplings and $I_{intra}(t)$ is the signal component from intra-molecule (each single molecule) dipolar couplings.

Considering first the signal $I_{intra}(t)$ which arises from the intra-molecule coupling, the electron spin pair signal. It is useful at this point to revisit the pulse sequence and to investigate the action of each of the pulses.

The sequence requires the use of two microwave frequencies which we will call $\omega_{mw\ observe}$ and $\omega_{mw\ pump}$. It will be assumed at this point that we have the case of an isolated pair of electron spins with a defined dipolar coupling between them and that one of the spins will be resonant at the microwave frequency $\omega_{mw\ observe}$ and the other electron spin will be resonant at $\omega_{mw\ pump}$. We will label both of these spins as spin A and spin B respectively. We will also call the pulses acting on spin A the observer pulses and the pulse acting on spin B the pump pulse. In the sequence is a refocused echo pulse sequence which consists of a $\pi/2$ pulse (pulse 1 in the observer sequence) which will excite coherence in spin A, and this will be allowed to evolve for a time τ_1. At this point the action of a π pulse (pulse 2 in the observer sequence) at time τ_1 will reverse the evolution of spin A and it will begin to refocus after another time τ_1 has passed, and at this point we can say that spin A has refocussed its spin evolution and there will be a spin echo. We can then wait another time τ_2 after this zero evolution and again apply a π pulse (pulse 3 in the observer sequence), which will again reverse the evolution of spin A and refocus it after a time τ_2 has passed. It is at the time τ_2 after the last observer pulse in the sequence when we detect and record the refocused spin echo which is formed. So far we have not applied our π pump pulse and will simply be measuring a refocussed echo. If we now apply the π pump pulse, at the $\omega_{mw\ pump}$ microwave frequency, which will act on the spin B we will observe a change in the measured echo. The effect of the π pump pulse on the echo will depend in part on the timing of the pulse relative to the zero evolution time described previously and the strength of the dipolar coupling. The origin of the modulation effect can be considered in terms of the so called spin precession. Each spin in the pair will have a spin precession frequency, its resonance frequency, which in the isolated spin pair case will be $\omega_{resonance\ A,B} \pm \frac{1}{2}\omega_{DD}$. If we have spin A precessing at the frequency $\omega_{resonance\ A} + \frac{1}{2}\omega_{DD}$ but then apply the π pulse to its partner in the pair, spin B, then only the sign of the dipolar coupling component will reverse. This means that after the application of the π pulse on spin B the precession frequency of spin A will change to $\omega_{resonance\ A} - \frac{1}{2}\omega_{DD}$, and when the final refocusing pulse is applied to spin A its evolution will have accumulated a phase lag. This will be dependent on how long after the zero evolution time the sign of ω_{DD} changed, under the action of the π pump pulse, and also how strong the dipolar coupling is, which defines the value of ω_{DD}. This lag in the precession causes imperfect refocussing in the final echo such that the echo amplitude we measure will be modulated. If we apply the π pump pulse at different intervals we can map out through the echo amplitude the oscillation frequency ω_{DD}, which in turn depends on the separation distance between the two electron spins and the intersection angle of the vector joining the spins through the static magnetic field.

The signal which we can measure as a result of the described experiment will take the form

$$I_{intra}(t) = I_0 \cos(\omega_{DD} \tau_{evolve}) \ ,$$

Equation 2.4.2

where I_0 is the echo height without the dipolar coupling interaction, ω_{DD} is the dipolar coupling and τ_{evolve} is the time the π pump pulse is applied relative to the zero evolution time. It is worth noting that this expression makes the assumption that the observer pulses only act on spin A in the pair and the pump pulse only acts on the spin B.

It is often the case that we have little interest in the $I_{inter}(t)$ signal component as it usually does not contain any relevant structural information and in these cases is referred to as the PELDOR background signal. We can minimize this signal component by making the sample very dilute thus shifting the distribution of inter-molecule distances to being longer and this decreasing the dipolar couplings relative to the intra-molecule dipolar couplings. However, as the sample volume will be fixed by practical considerations of the spectrometer the number of spins contributing to the PELDOR signal will reduce with the concentration and thus the minimum sample concentration will be dictated by the sensitivity of the spectrometer and available measurement time. The $I_{inter}(t)$ signal component resulting from a 3-dimensionally homogeneous distribution of spin pairs in a glassy matrix, which is the relevant case for samples discussed in this work, can be described by the signal expression

$$I_{inter}(t) = \exp(-kCF_B|\tau - t|) \; .$$

Equation 2.4.3

Where C is the sample concentration, F_B is the fraction of spins excited by the pump pulse, τ is the time between the first and second pulse in the observer pulse sequence which is the zero evolution time of the observer spins and t is the time of the pump pulse relative to the zero evolution time. The value of the constant k is given by [76]

$$k = \frac{8\pi^2 {\mu_B}^2 g_A g_B}{9\sqrt{3}\hbar}$$

Equation 2.4.4

The work presented here, and a large amount of the PELDOR experiment applications, is to study the structure of bio-macromolecules. The sample will often not have any unpaired electron and will be EPR silent, and will be labelled with an electron spin using a technique called site directed spin labelling

(SDSL). SDSL targets particular residue sites on a molecule such that they will accept the chemical attachment of a small label molecules. A spin label is a relatively small and stable molecule which has an unpaired electron and several types of these molecules having been developed, a topic which has been discussed in several reviews [7, 21, 23]. What is of immediate relevance, however, is that SDSL will result in the same type of spin label being attached to each targeted site on the molecule and that there will be no differences between either of the attached spin labels. To a large extent this makes it impossible to specifically target any of the spins. This conflicts with the previous discussion of the PELDOR experiment where we stated that we should excite one of a pair of electron spins with the observer pulses to be a spin A and the other electron spin in the pair with the pump pulse to be a spin B. However, it is the case that the spectrum of the unpaired electron of the spin label is broader than the excitation bandwidth of the pulses. This has the direct result that for any pulse not all of the spin label spins will be excited, and we can make the assumption that the spin label has no preferential orientation relative to the magnet field, we will have some probability, which can be calculated, for the pulse acting on any given spin. This means that although we cannot individually select any spin to be a spin A or a spin B we can calculate that there will be some number of the available spins which are excited by the observer pulse as spin A and for those spins there will be some fraction of those spin A which will have a partner spin B excited by the pump pulse. For simplified analysis we often call the fraction of the spectrum excited by the pump pulse $\Delta\lambda$ and we can approximate this to be the fraction of spin A which have a partner spin B.

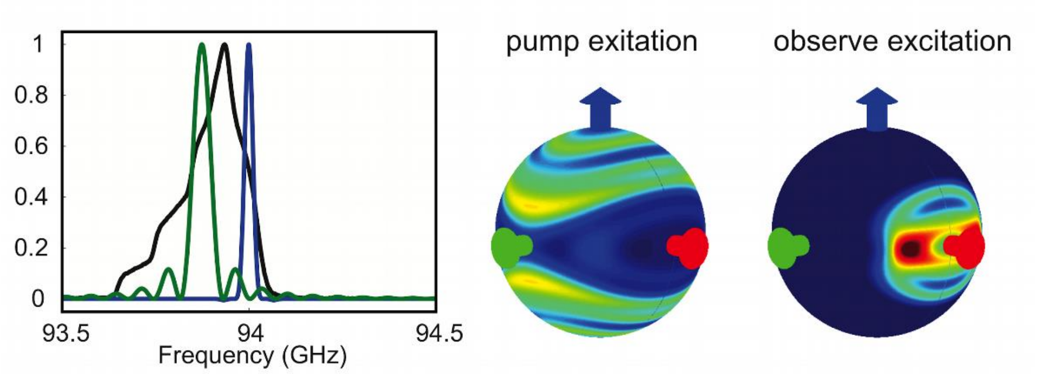

Figure 2.4.1 *Left: Nitroxide spin label spectrum for a magnetic field strength of 3.3435 T in black overlaid with pump pulse excitations (green) and observe pulse profile (blue) using π pulse lengths of 10 ns. The observer pulse sequence is shown using an excitation frequency of 94.000 GHz and the pump pulse is shown using an excitation frequency of 93.875 GHz. Right: The corresponding orientation selections of the spin label relative to the magnetic field direction.*

Shown in **Figure 2.4.1** is a diagram of a typical nitroxide spin label spectrum at 3.34 T or 94 GHz in black, where it is broadened from the case of a single resonance by the hyperfine interaction and anisotropy in the g-factor value. Shown overlaid is sketches of typical excitation bandwidths of the pump pulse in green and the observer pulses in blue. What can be seen is that at W-band we will often excite only a fraction ~20 % of the electron spins available in the sample with a given pump or observer pulses. Using these assumptions and experimental conditions we can expand expression **Equation 2.4.2** of the PELDOR sequence to give the well-known signal expression

$$I_{intra}(t) = 1 - \Delta\lambda(1 - \cos(\omega_{DD}\tau_{evolve})) \,,$$

Equation 2.4.5

where ω_{DD}will depend on the geometry of the spin pair. We can write this expression in a form which includes the dependence of these terms on the angle Θ_{AB}, which is the angle between the vector which connects the two spin and the unit vector of the magnetic field. We can then take the volume average to arrive at the expression

$$I_{intra}(t) = 1 - \int_0^{\pi/2} \Delta\lambda(\Theta_{AB})(1 - \cos(\omega_{DD}(\Theta_{AB})\,\tau_{evolve}))\,\sin(\Theta_{AB})\,d\Theta_{AB}\ .$$

Equation 2.4.6

Here it is important again to see that there is an orientation dependence on the dipolar coupling term $\omega_{DD}(\Theta_{AB})$, as previously discussed, but that there is also an orientation dependence on the fractional excitation, or so-called modulation-depth, term $\Delta\lambda(\Theta_{AB})$. The orientation dependence of the $\Delta\lambda(\Theta_{AB})$ term will only exist if there is sufficient angular correlation between the spins. The origin of the angular dependence is that there are anisotropic interactions in the individual spin Hamiltonians such that their resonance will depend on their orientation inside the main magnet field. This gives up the ability to select spins by setting our pulse microwave frequency to the resonance corresponding to particular orientations. We can then split the analysis of the PELDOR signal into two limiting cases, the case of random orientation of the spin where there is no, or weak, angular correlation and the case of strong angular correlation.

2.5. PELDOR SIGNAL ANALYSIS: WEAK ANGULAR CORRELATION

The most commonly used spin label is the methanethiosulfonate spin label (MTSSL) which in many cases has very weak angular correlation to either its attachment point on the biomolecule, and to the other spin labels attached to the molecule. This is then the weak angular correlation case, and the analysis which is often performed is based around regularized fitting [77, 78] of **Equation 2.5.1**. If we examine the previously presented signal expression

$$I_{intra}(t) = 1 - \int_0^{\pi/2} \Delta\lambda(\Theta_{AB})(1 - \cos(\omega_{DD}(r, \Theta_{AB})\, \tau_{evolve}))\, \sin(\Theta_{AB})\, d\Theta_{AB} \,,$$

Equation 2.5.1

we see that the without angular correlation of the spin labels the values of Θ_{AB} will have a uniform distribution of angles. This is because there is no preference when the spin labels have no angular correlation to each other. As such $\Delta\lambda(\Theta_{AB})$ will take an average value for the volume, which for a large enough volume of spin pairs, will approximately be determined by the fraction of total spins which were excited by the pump pulse. We also generalise the value of the dipolar coupling ω_{DD} to be a function of the spin separation which is valid if there is mutual orientation correlation between the spin labels, as discussed in earlier chapters. We can now simplify the analysis greatly by generating a so-called discrete kernel function which will be the uniform angle distribution averaged PELDOR signal for each discrete spin separation r. We can all this kernel function $K(r)$ which will return an angle averaged PELDOR signal for a given value of r. There will be a distribution of label separation r due to factors such as flexibility of finite length spin label relative to its attachment point and the flexibility of the biomolecule causing a distribution in the separation between the attachment points. This can be expressed as a distribution function $\rho(r)$.

We can state our problem as finding the correct distribution of spin separation distance $\rho(r)$ from our measured PELDOR signal. We can often define a limited range of r which we know will correspond to either the known physical limitations of the measured biomolecule or, more often, to the physical limitations of the experiment. For common PELDOR experiments this limits the range to between $2nm$ to $8nm$. A kernel K is generated for discrete values of r in this range and we define the least squares minimization problem as

$$\min \|K\rho - S\|_2 \,,$$

Equation 2.5.2

Where K is the discrete kernel, ρ is the positive value vector of the distance distribution, S is the measured PELDOR signal and $\| \quad \|_2$ is the Euclidean norm. This is suitable as long as S obeys the approximation of being in the weak angular correlation limit along with being free of noise and artefacts. This is not a common experimental condition and instead we cannot guarantee a unique solution to ρ such that the problem is said to be ill-posed. Mathematical methods have been developed to deal with such ill-posed problems and the appropriate choice for this problem was determined to be the so called Tikhonov difference regularized minimization. The basic principle is not to determine the solution ρ based solely on the smallest deviation from the measured signal S but to also include an additional penalty which is an operation performed on ρ. For the PELDOR experiment the additional penalty which produces the most physical and robust solutions of ρ is the second derivative operator penalty. We can rewrite the problem to include this extra penalty

$$\min \|K\rho - S\|_2 + \alpha \|D\rho\|_2 \ ,$$

Equation 2.5.3

where D is the second derivative operator acting on the guessed distribution ρ and α is a weighting of the derivative penalty. The choice of α is most commonly determined by the L-curve method [79], which tries to determine the optimal compromise between solution smoothness and goodness of fit.

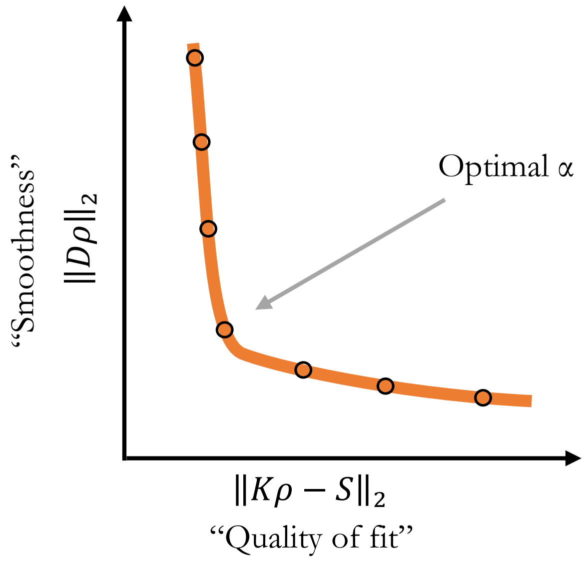

Figure 2.5.1 *Typical L-curve for a PELDOR distance analysis. The arrow indicates the point of largest gradient change, which corresponds to a mathematical optimum regularisation parameter.*

A sketch of a typical L-curve is shown in **Figure 2.5.1** where the two axes are log scale. It can be seen that there is a distinct corner which represents a good compromise between over regularized and poorly fitting solutions and under regularized but erratic solutions.

2.6. PELDOR SIGNAL ANALYSIS: STRONG ANGULAR CORRELATION

The distinct difference between analysis of the weak and the strong angular correlation case is that we can no longer assume that the angle Θ_{AB} will be uniformly averaged in every experiment. In other words the angle Θ_{AB}, the angle between the vector that connects the two spins and the magnetic field vector, will depend on the geometry of the spin labels. We had previously mentioned that the spin label spectrum can be broadened by g tensor and hyperfine anisotropy, and this is true for the nitroxide spin labels which will be discussed here. As discussed in the earlier Chapter 2 , the g-factor tensor orientation anisotropy is field dependent and difficult to resolve at lower fields. For the MTSSL and Rx spin labels used in this work fields of >3.3 T (W-band) are required to suitably resolve the g-factor anisotropy for the orientation selective PELDOR analysis which is presented. This field requirement has been discussed in previous studies [48]. The interest in having the g-tensor anisotropy resolved is such that resonances corresponding to different orientations of the spin label in the magnetic field are spread far enough apart that we can selectively excite them with our pulses. This requires special hardware as discussed in the later Chapter 2.8 and Chapter 3 .

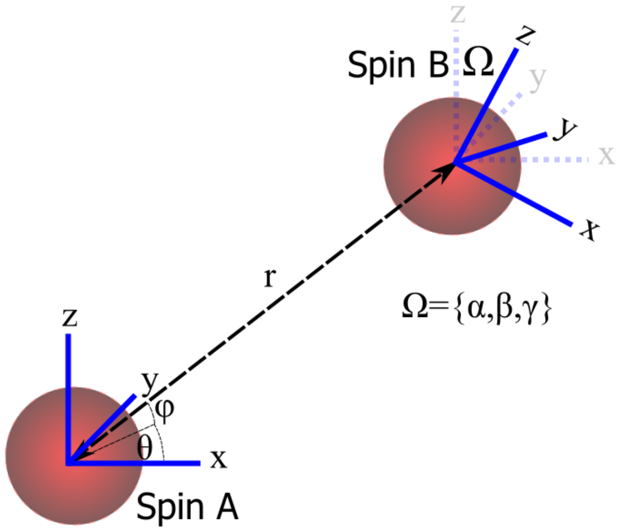

Figure 2.6.1 *Model of rigid spin pair. The model is parameterised with the position of Spin B relative to Spin A given by the spherical coordinates (r,ϑ,φ) and the relative rotation of the principal axes of Spin B relative to Spin A is given by the Euler rotation angles (α,β,γ).*

To express the orientation dependence of the spin label resonance and the resulting PELDOR signal we can define the relative angles and positions of the two spin labels, as shown in **Figure 2.6.1**. This description of the system specifies the axis frame of Spin B relative to the frame of Spin A by the Euler angles **Ω**. There are many mathematical definitions which can be used to specify 3-dimensional rotations, however, it is beneficial to use Euler angles as there are many computational tools and references for their use. As the resonance of Spin A and Spin B is each determined by how the frame is orientated relative to the magnetic field vector, we can imagine the rigid case where the Spin A x axis is aligned with the magnetic field vector and due to their defined relative rotation to each other the Spin B y axis is aligned with the magnetic field vector. The resonance of Spin A will correspond to the x component of the anisotropic g-tensor, and hyperfine tensor, and the Spin B resonance will correspond to the y components. The PELDOR modulated signal, as previously discussed, will only be observed in the cases where one of the two spins is excited by the observer pulses and the other spin is excited by the pump pulse. If the spin A is excited by the observer pulses but the spin B is not excited by the pump pulse then we observe an echo which is not modulated by the PELDOR effect. This contributes to the measured signal as a decrease in the depth of the modulated component. If only one spin is excited by the pump pulse then we do not observe a contribution to the measured signal from a single molecule although can have an effect on the background signal component.

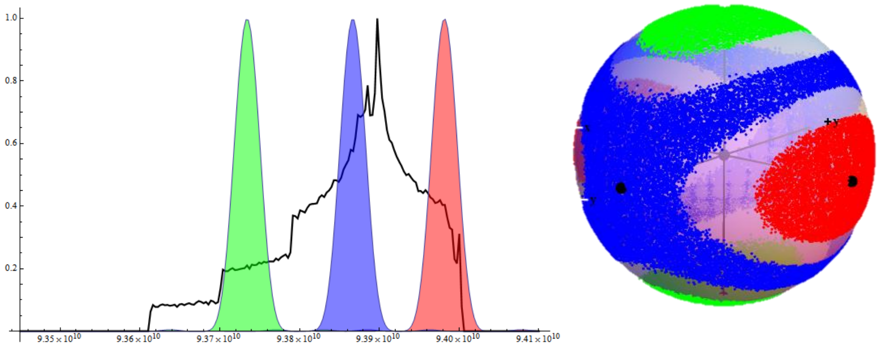

Figure 2.6.2 *Typical W-band Rx spin label spectrum showing example pulses on a sphere. The excitation profiles of the pulses*

A plot of the spectrum of a nitroxide spin label with example pulse excitations overlaid is shown in **Figure 2.6.2**, with the corresponding magnetic field vector direction in the spin label frame for each of the pulse excitations shown beside. This illustrates the example where the observer and pump pulses can be some combinations of the different excitation positions that correspond to orientations of the label. Further to this it emphasises the requirement for the spectrometer to operate with a bandwidth larger than or equal to the spectral width of the spin label so that all the orientation combinations can be excited.

As the sample often consists of a glassy matrix of individual molecules each with a random orientation relative to each other it is useful to consider this case inside the magnetic field. An example case is illustrated in **Figure 2.6.3**.

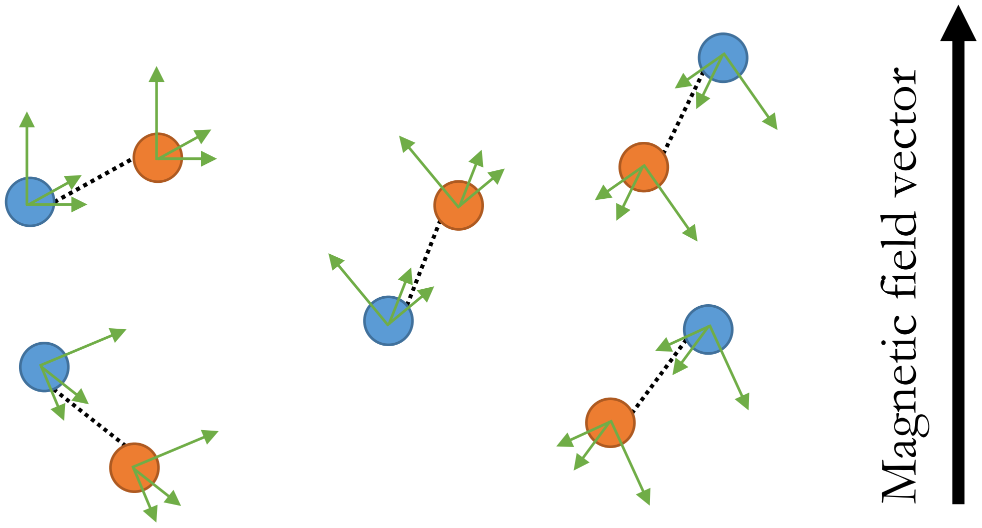

Figure 2.6.3 *Cartoon of a glassy matrix of spin pairs.*

In this figure there are pairs of spin labels and each spin label is orientated co-linear to each other, and each pair of labels has no angular or distance correlation to each other. If we apply pulses which are close to each other on the spectrum we will be exciting orientations which are collinear to each other and we would expect to see a strongly dipolar modulated PELDOR signal, whilst and excitation on spectral positions which correspond to non collinear orientation would result in a poorly dipolar modulated PELDOR signal.

The process of analysis in this work is the fitting of the model described above with distributions applied. This is done by using a global optimisation algorithm, in this case a genetic algorithm, and simulating the PELDOR signal response for that model and using the root mean square difference of the two signals as the minimisation penalty. It is worth at this point emphasising the fact that the experiment is insensitive to the orientation of the axes of the tensors relative to the magnetic field, such that is it is not possible to know if each axes is orientated with its positive, or negative, direction pointing with the direction of the magnetic field. This results in a number of symmetric solutions corresponding to the different combinations of the axes directions being inverted. The spin label can be rotated 180 degrees around any axis and give the same modulation depth and depending on the alignment of the nitroxide molecules can also return similar or the same oscillations. This means that when applying the orientation result of the PELDOR signal analysis to the underlying structure of a biomacromolecule we have to consider all of the possible symmetric solutions.

2.7. PELDOR SIGNAL OF MULTIPLE SPINS IN AN OLIGOMER

The PELDOR signal observed from a system containing multiple spins has been discussed for the case where there is no correlation between orientations or positions, which was the inter-molecule signal contribution to the spin label pair PELDOR signal. However there is the case where there are multiple, >2, spin labels in defined positions molecule or the cases where a molecule of interest is made up of several identical molecules assembled to be a larger molecule, this is termed an oligomer. In the case of an oligomer where a spin label is introduced in one position of one unit molecule it will appear for as many times as there are units in the oligomer, and the distances and orientations of each unit molecule to each other will be structured. The

PELDOR signal expression for these cases where there are multiple spins in a cluster will be

$$I_{intra}(t) = \sum_{probe\ spin}^{N} \prod_{\substack{pump\ spin \neq \\ probe\ spin}}^{N} 1 - \Delta\lambda(1 - \cos(\omega_{DD}\tau_{evolve}))\ .$$

Equation 2.7.1

This product factorisation can be made in the PELDOR experiment due to the fact that the pulse exciting the pump spin B is strong enough to excite the resonance doublet and that any ‘mixing’ of states between the pumped spins will not be recovered in the observer spin coherence which we are observing [80].

2.8. HIPER W-BAND SPECTROMETER

To make these measurements in a practical way specialised instrumentation is required and thus it is necessary to discuss the merits of the lab-built spectrometer, “HiPER”, which is used to make the experimental measurements presented. The spectrometer operates at W-band (94 GHz and 3.35 T for free electron g-factor) and is optimised for pulsed operations with a peak pulse output power of ~1 kW. Of particular value to this work is the large ~800 MHz instantaneous bandwidth of the instrument.

Instantaneous bandwidth refers to the 3 dB bandwidth of the instrument. This is important as the spectral width of a nixtroxide spin label radical at W-band is around ~400 MHz. Different frequency pulses can thus be applied to any part of its spectrum on fast time scales without having to move the magnetic field. The frequency separation of the relevant pulses can also be arbitrary within the 800 MHz bandwidth.

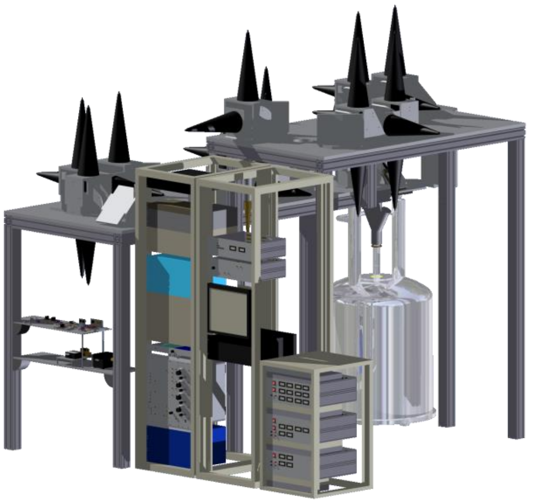

Figure 2.8.1 *CAD illustration of the HiPER spectrometer. Credit to Dr Robert I. Hunter for the CAD drawings.*

To achieve this large overall instantaneous bandwidth, all of the components in both the transmit and receive paths are required to individually operate over large bandwidths, which is technically difficult to achieve at these high frequencies. In particular commercial EPR spectrometers operating at X-band (~9.4 GHz) and W-band (~94 GHz) are normally limited in bandwidth by the amplifier and resonant sample holder used.

At X-band the requirement for large bandwidth is relaxed by the fact that EPR spectral widths are often narrower. For the case of nitroxide spin labels at higher frequencies such as W-band the anisotropies in the g-factor are well resolved and the spectral width is thus increased compared to lower frequency EPR.

Commercial spectrometers at W-band have much lower power output than what is available at lower frequencies with solid-state amplifiers usually operating with an output power of <1 W. The amplifier power output to some extent defines the sample holder used in the spectrometer as pulsed EPR operation requires the magnetic field component of the oscillating electro-magnetic (EM) wave to be large enough to change the state of the electron spin on a timescale much shorter than its relaxation. Further to this the length of the pulse also determines the bandwidth over which the pulse can affect electron spins and if this is too small then the number of spins contributing to an EPR resonance signal will be small making signal detection difficult. Thus pulse lengths at W-band will typically need to be 10's of nanoseconds.

For these reasons commercial EPR spectrometers tend to need resonant cavity sample holders with reasonably large quality factors (Q-factor) to increase the amplitude of the EM wave at its resonant frequency. However this Q-factor will have an associated bandwidth, which for the Q values required to achieve pulse lengths of 10's of nanoseconds with 1 W (Q~1000) will have a 3 dB bandwidth of ~100 MHz. These large Q-factor resonators will also have a sample volume typically only around 1μL, which is limited by the required resonator dimensions.

By having a large output power of 1 kW the HiPER spectrometer can use a sample holder with a much lower Q-factor and increase the 3 dB bandwidth significantly. The amplifier in the HiPER spectrometer is of the extended interaction klystron (EIK) type[1] which at 94 GHz has a peak pulsed output power of ~1 kW and a quoted operating full power bandwidth of ~1 GHz. The non-resonant sample holder used in the HiPER spectrometer supports a microwave field strength at the sample which corresponds to π pulse length of ~10 ns with a sample volume of 60μL. A cut-through diagram of the sample holder is shown in **Figure 2.8.2**.

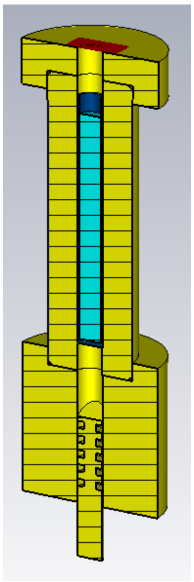

Figure 2.8.2 *CAD drawing of the HiPER spectrometer sample holder.*

The spectrometer operates in an induction mode, which has the characteristic of improved isolation over the commonly used reflection mode. The general principle of induction mode is that the EPR signal originates from the absorption of circularly polarised microwaves by the electron spin, and its

---

[1] There are currently very few alternatives to EIK type amplifiers which exhibit the operating stability and signal purity required at these high frequencies whilst still providing large output powers but it is noted that there is an ongoing collaboration between the University of St Andrews 'millimetre wave and EPR group' and the 'Atoms, Beams, and Plasmas group' at the University of Strathclyde to produce very high power large bandwidth amplifiers up to 400GHz for use in EPR spectrometers.

resonant emission is also emitted with circular polarisation. As circularly polarised light can be considered as the superposition of two linear polarizations it is possible to excite a resonant EPR signal of the electron spin with just one of these linear polarizations. If we set up our detector using polarization selective quasi-optical isolator components we can receive only the orthogonal polarization to the one which was transmitted to the sample. This means that one of the two polarizations of the circularly polarization resonant EPR signal can be received in near complete isolation of the transmitted signal. This has a number of relevant advantages to the spectrometer performance. The primary advantage is that the receiver can be made extremely sensitive for the small EPR signals without being damaged by the high power transmitted pulse signal. The so called 'dead-time', which is the time taken after the pulse before the receive can begin to detect a signal, can also be very small meaning that in pulsed EPR experiments which require detection very close to the end of a pulse, such as free induction decay (FID) detection and short time phase memory time experiments, can be made possible.

However there are some drawbacks to this configuration of non-resonant sample holder. Unlike a typical EPR resonator, which is designed such that the sample is dominantly exposed to only the oscillating magnetic field component, the non-resonant structure used in HiPER has the sample positioned in regions of both strong oscillating microwave magnetic field and electric field. The result of this is that the sample is now sensitive to dielectric losses resulting in an associated attenuation of the microwave signal propagating through the sample due to electric field interactions. It is also possible for wave scattering effects to occur which can cause increased difficulties in isolating the transmitted signal from the EPR signal. For the common biological sample cases of glassy water/glycerol samples cooled down to temperatures of around 60 K in plastic tubes this effect is largely negligible. If the sample is several wavelengths long the microwave magnetic field strength seen by the sample will vary across the length and in some experiments this will need to be taken into account. Although for the TE11 field distribution in the HiPER spectrometer, which is a Bessel in the plane across the waveguide and sinusoidal along the length of the waveguide, then the spins which are not in peak of the field strength will not evolve with sufficient spin magnetisation and coherence to contribute to the signal.

During the course of my study I have also been involved in development of high performance feeds for quasi-optical and antenna systems and patent application, pre-print and peer-reviewed first author publications have been included as an Appendix.

Chapter 3 HIPER SPECTROMETER FOR PELDOR MEASUREMENTS

The successful analysis and interpretation of the PELDOR experiment, particularly when trying to solve orientation selective problems requires the pulse spectrometer to be well characterised. Several of the previously described experiments require more than one microwave source operating at different frequencies, one of those experiments being the four pulse PELDOR sequence. As the spin system and thus the measured PELDOR signal will respond as a function of the B_1 field, the magnetic field component of the microwaves, strength it is particularly important to understand how B_1 varies as a function of the microwave frequency. To ensure that the spectrometer is performing as expected over a large bandwidth and allow for quantitative analysis of experiments using multiple frequency sources a number of characterisation measurements were made, and are presented here.

3.1. BANDWIDTH HIGH POWER CHARACTERISATION

A study of the full bandwidth characteristics of various transmit components in the output chain of the HiPER spectrometer was conducted by recording the voltage outputs of a number of fast responding power detectors. The transmit output chain of the HiPER spectrometer can be simplified to only the bandwidth limiting components and this is shown in **Figure 3.1.1**.

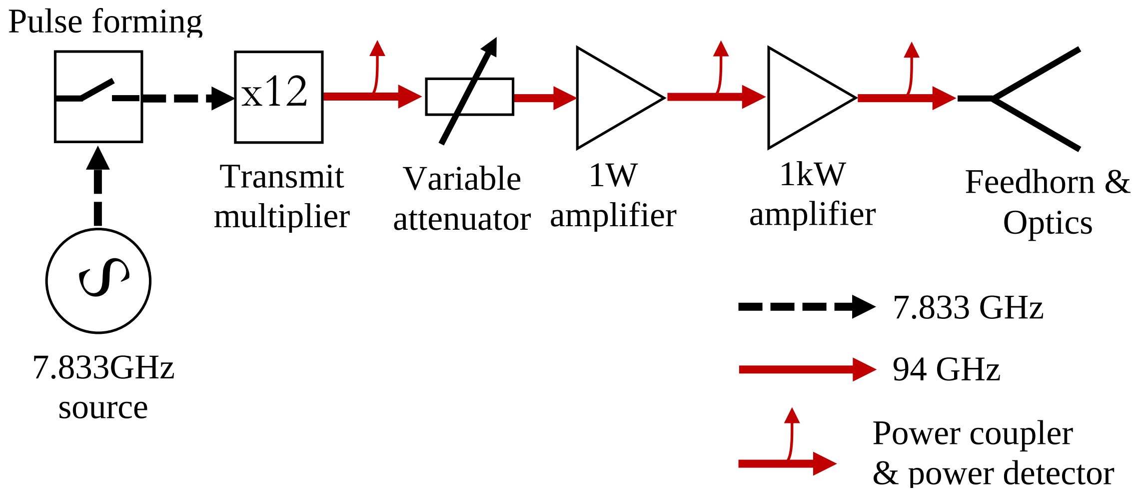

Figure 3.1.1 Schematic of the HiPER spectrometer transmit chain.

The basic principle of the transmit chain is to start with a 7.833 GHz source on which the pulses are formed via a wide band fast mixer switch. This signal is then fed through a x12 VDI[2] manufactured multiplier to give a 94 GHz output and the pulses are subsequently amplified to a peak power of 1 W using a QuinStar QPN amplifier[3] and then 1 kW using a CPII EIK amplifier[4]. Each of the components are connected to the next stage via power couplers such that their output powers can be monitored as shown in **Figure 3.1.1**. These detectors were calibrated using an HP437 power meter connected via appropriate power detector heads.

The output and input power levels of all the amplifiers was checked across the 1 GHz band around 94 GHz using the calibrated power detectors attached to

---

[2] Virginia Diodes Inc, 979 2nd Street SE, Suite 309, Charlottesville, VA 22902, United States

[3] Quinstar Technology Inc, 24085 Garnier St, Torrance, CA 90505, United States

[4] Communications & Power Industries LLC, 45 River Drive, Georgetown, Ontario, Canada

the couplers before and after each amplifier. Losses of the connecting waveguide sections and the couplers were taken into account during the calibration of the power detectors.

The VDI multiplier chain produces an output of 190 mW (22.8 dBm) at 94 GHz at the input of the initial Quinstar amplifier, after waveguide and coupler losses, which is enough input power to achieve the 1 W (30 dBm) saturated output power from the amplifier. Due to the internal arrangement of the multiplier chain its output power is effectively fixed at this level, although it is noted that the output power has a temperature dependence which requires the device to reach a thermal equilibrium before stable output is reached. A variable attenuator with 60 dB range is positioned between the multiplier output and the input of the Quinstar amplifier such that the amplifier can be operated within its uniform 25 dB gain region, the so called linear region. This input power was measured to be between approximately -30 dBm to 0 dBm and is shown in **Figure 3.1.2**. The attenuation level of the variable attenuator was set to provide the maximum allowed input power to the EIK amplifier of 50 mW (17 dBm) and adjusted to give saturated output from the EIK amplifier. To find the saturated output and the appropriate input power to achieve this a measurement of the power output was also conducted for the EIK amplifier and this is shown as **Figure 3.1.3**. Although it seems contrary to attenuate the 22.8 dBm multiplier output prior to a 25 dB gain Quinstar amplifier, the purpose of this amplifier is to provide, first a higher power CW source and second enough dynamic range to insert a second path with a variable attenuator prior to the EIK amplifier so that it is possible to have two power levels set and switched between during an experiment. This has particular application in experiments such as matched electron spin echo envelope modulation (ESEEM) [81].

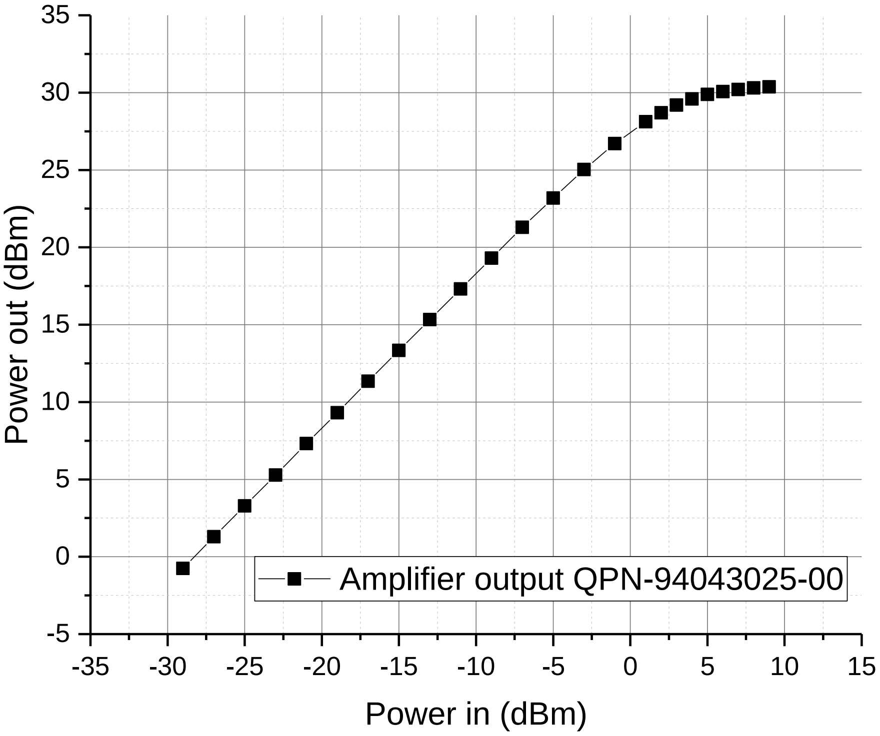

Figure 3.1.2 *Power input vs Power output of Quinstar solid state W-band amplifier*

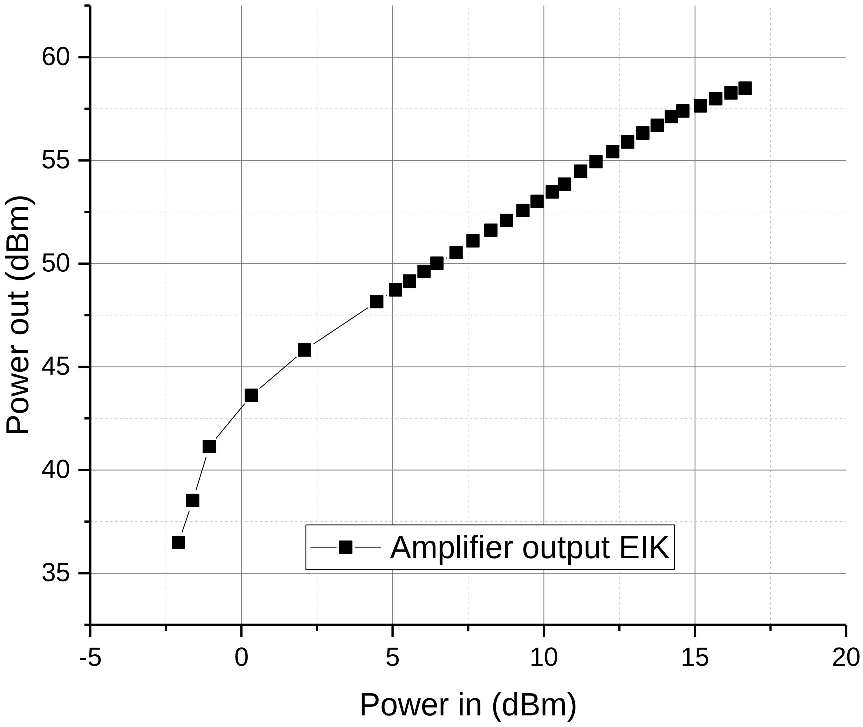

***Figure 3.1.3** Power in vs Power out of CPII EIK W-band amplifier*

These measurements allowed the power levels to be set to achieve maximum safe output from each of the amplifiers. Due to the difficulty of changing the level of attenuation of a variable attenuator on the nanosecond timescale, and only having the option of two output power levels, it is generally not possible to dynamically change the input power levels to the amplifiers during a pulsed EPR experiment. For this reason the power levels used in the bandwidth characterisation and experiments were the levels optimised for amplifiers at 94 GHz, and it is noted that these power levels may not be optimal across the whole bandwidth of the amplifier.

As an initial study the manufacturer specified bandwidths of all the components in the transmit chain were compared. The VDI manufactured x12 multiplier chain is specified to have a saturated power output of 240 mW, directly at its output, over a 4 GHz bandwidth around 95 GHz. The QuinStar QPN amplifier is specified to operate at continuous 1 W output over a 6 GHz bandwidth around 93 GHz. The CPI Extended Interaction Klystron (EIK) capable of 1 kW peak pulsed power with a 10% duty cycle and is specified to operate over a ~1 GHz bandwidth around 94 GHz. As such it is expected that the 1 kW EIK amplifier will be the bandwidth limiting device in the transmit chain.

At this point it has been assumed that the corrugated feedhorns and optics, which have the function of transmitting the microwave fields to the sample, have a wide bandwidth. However it is still is of interest to verify this assumption and as such the loss was measured between the transmit and receive feedhorns and optics using an Anritsu VectorStar ME7838A Vector Network Analyser. A reflecting mirror was placed in the sample position and optimised for maximum power transmission. The power losses, through both the transmitter and receiver optics, as a function of bandwidth (S21) is shown in **Figure 3.1.4**. The normalised losses shown in this figure are for a full round trip of the optics, both the transmit and detection paths, and will be an overestimate of the microwave losses from the source to the sample. These measurements confirm that the feedhorn and optics have a bandwidth larger than that of the preceding amplifiers.

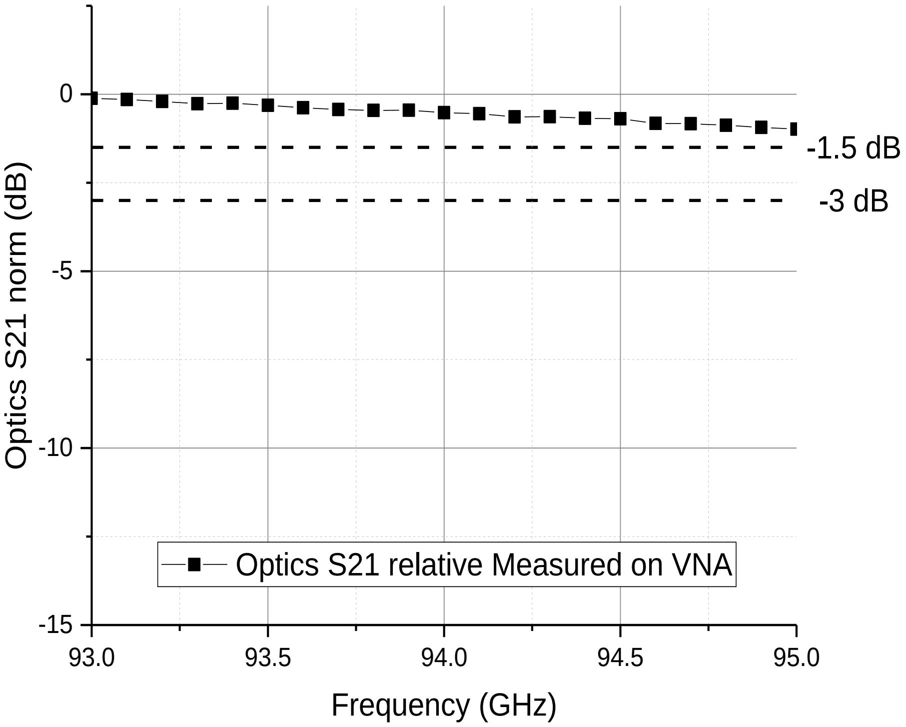

Figure 3.1.4 *A plot of the normalised to maximum VNA measurement of S21 HiPER transmit to receive quasi-optics characteristics. This measurement indicates the loss of the spectrometer optics, which varies by less than 1.5 dB across the measured band. The dashed lines indicate losses of 1.5 dB and 3 dB to aid interpretation of the plot.*

To investigate the effective bandwidth of the combined components all of the power monitors connected through the couplers were monitored whilst the primary spectrometer source was tuned to different frequencies. The variable attenuator was set to give saturated output power from the 1 kW EIK amplifier at 94 GHz as previously described and this level was used for all the different frequencies to best represent experiment conditions. A plot of the measured normalized power output for the multiplier chain, initial 1 W amplifier and the 1 kW amplifier as a function of frequency are shown in **Figure 3.1.5**. As the high power final stage EIK amplifier can only operate in pulsed operation with a maximum 10% duty cycle all measurements were taken by averaging the peak output of a 200 ns long pulse using a LeCroy WaveMaster 8620A for 2000 shots.

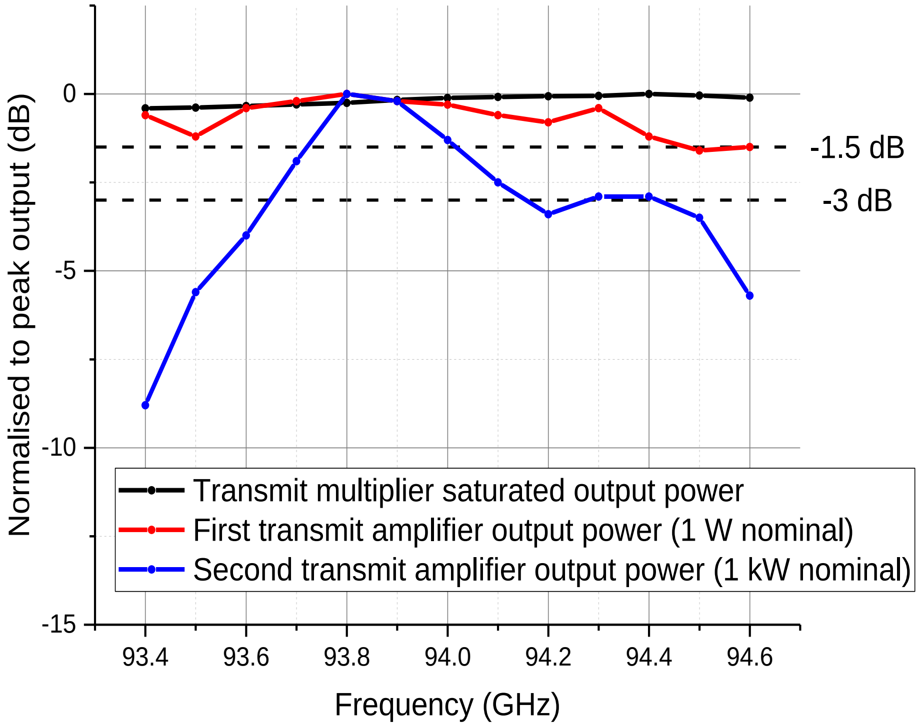

Figure 3.1.5 Overlaid comparison of output powers measured for each amplified stage of the HiPER transmit chain.

From this data it was confirmed that the bandwidth of the EIK 1 kW amplifier is the bandwidth limiting component, however, when this data was compared to the specification from 2010 it can be seen that the bandwidth of the amplifier was less than the expected 1 GHz, this comparison is shown in **Figure 3.1.6**. It was concluded that this is in part due to the way the HiPER spectrometer is configured for saturated power output at 94 GHz and it is assumed that the same input power level will produce saturated output power at the other frequencies. It may also be the case that the EIK amplifier tube is degrading, as might be expected for an amplifier of this type. Further work is required to confirm this hypothesis, and this effect would need to be taken into consideration for any ultra-wide bandwidth EPR experiments. It is also possible that the amplitude variation across the band could also be compensated by using an arbitrary waveform generator producing pulses designed to give a flatter output response from the spectrometer [82, 83]. This may require that the maximum power output is reduced by between 1-3 dB to flatten the overall output.

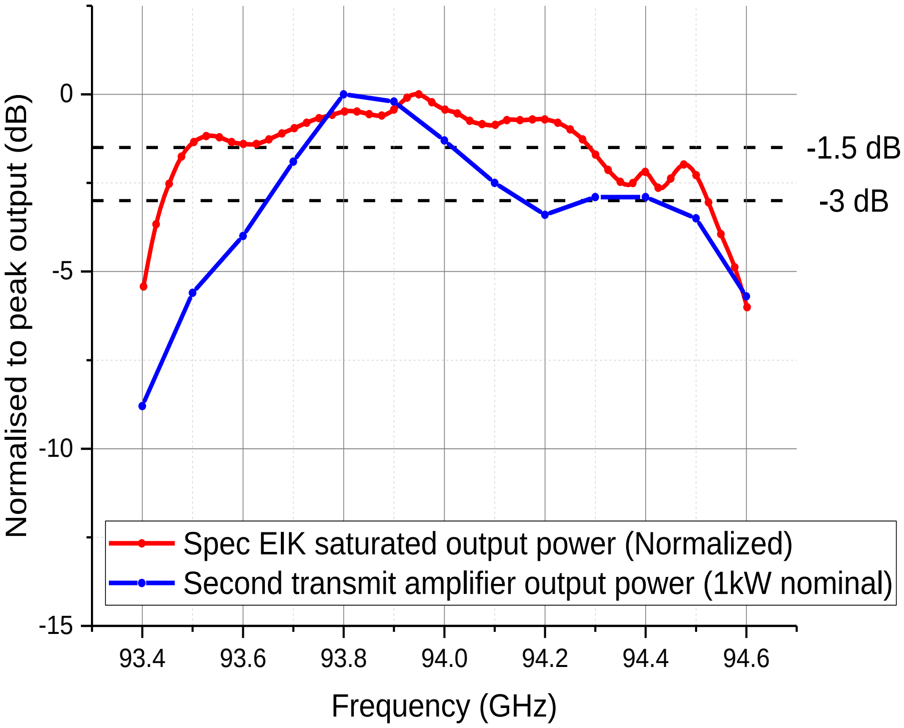

Figure 3.1.6 *Overlaid comparison of the EIK output power measured on the HiPER spectrometer and the saturated output power provided by the manufacturer.*

It is possible to verify the microwave field strength arriving at the sample by conducting a pulse EPR nutation experiment. This experiment measures the magnetisation of the spin which has been induced by an initial microwave pulse of varying length and this is done by monitoring a spin echo. As the initial pulse length is varied the spin echo amplitude will be modulated as the initial spin state is varied by the pulse. The correlation between the initial microwave pulse length and the measured magnetisation has a direct correspondence to the effective microwave magnetic field component, the B_1 field, and this can be directly compared with the expected field strength based on the spectrometer power calibrations. It is important to note that due to the type of sample holder used in the HiPER spectrometer the sample will see a distribution of B_1 field amplitudes, and the nutation experiment will measure an average of this distribution, a so called effective B_1 field strength.

Two nutation experiments were made, one made before the addition of the 1 W Quinstar amplifier and one measurement after, as a function of pulse excitation frequency with a sample volume of ~90 μL. The experiment was conducted using an EPR active coal sample. The pulse lengths for the echo sequence were optimised by maximising the signal. The initial nutation pulse length was varied from 0 ns length until 400 ns to fully sample the nutation cycle. The nutation pulse was made non coherent with respect to the echo sequence pulses by using an independent uncorrelated microwave source to minimise any spurious coherent EPR signals. The nutation signals were analysed by calculating the discrete Fourier transform (DFT) and picking the largest spectral component. A plot of two of these measurements is shown as **Figure 3.1.7**.

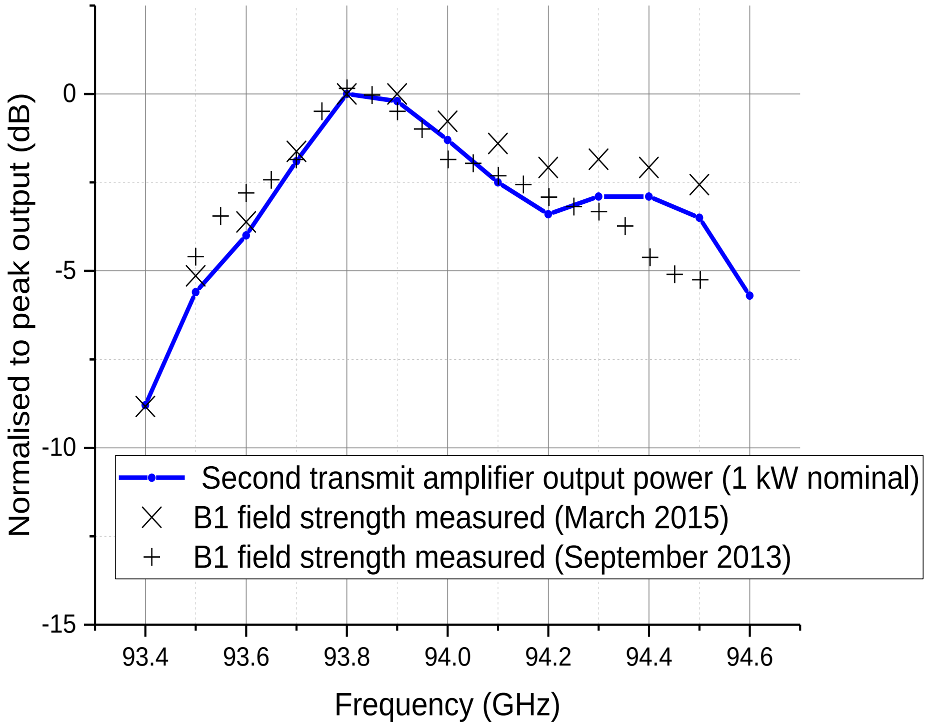

Figure 3.1.7 *Overlaid comparison of the* B_1 *field measured on the HiPER spectrometer and the measured amplifier power output of the EIK amplifier.*

The two measurements of the effective B_1 field were made during March 2015 and September 2013 respectively, and these represent the HiPER spectrometer before and after the 1 W QuinStar amplifier was installed. The results are very similar for both cases and closely match the power output measurement of the amplifier within 3 dB. Factors which could have an influence on the measured effective B_1 field other than the power output and the feedhorn and optics are sample tube and any dielectric interactions of the sample.

In several measurements of the B_1 field strength anomalous results were seen at spot frequencies and these results would change with different sample tubes. These results showed an increase in effective B_1 field and a signal reduction at other frequencies. It was found that the removal and replacement of the same sample and tube would sometimes not yield repeatable results. This was further investigated.

3.2. PROPERTIES OF EPR SAMPLE TUBE MATERIALS IN NON-RESONANT SAMPLE HOLDERS

Further to understanding the transmission characteristics of the spectrometer it is important to ensure the sample itself is not strongly interacting with the microwave field. This is a concern in low Q, non-resonant reflection spectrometers where small sample interactions can have a strong influence on the microwave response of the spectrometer. In this sample configuration the sample will not only be exposed to the magnetic field component of the microwaves, which is the common case for a simple mode cavity or loop gap resonator, but also the electric field component. Due to electric field interactions at the top and bottom interfaces of the sample there is potential for it to act as a weak Fabry-Perot resonator, which although will cause a reduction in the bandwidth will only have a very small effect compared with the bandwidth of the amplifiers due to the low Q of the effect. There is also potential for there to be dielectric signal losses in the sample, ie with imaginary dielectric constant components. For high dielectric loss samples the signal loss can be heavily reduced by modifying the sample configuration, such as a thin film of sample placed appropriately near a reflecting surface at the bottom of the transmission waveguide where the sample will see only the magnetic field component of the microwaves. For the work presented in this thesis it is relevant that the loss component of the dielectric constant is very small for ice and water/glycerol mixtures of ~50/50 and biological samples will in most cases be dissolved in a similar water/glycerol mixture. But the sample will need to be in some form of container prior to being placed in the sample holder, and this container can have a more significant dielectric interaction than the sample itself, and for this reason different tubes containing sample were investigated.

Commonly used sample tubes for EPR are composed of quartz, and the HiPER spectrometer was designed to be compatible with 3 mm outer diameter, 30 mm long quartz tubes. However, during the course of experiments it was noticed that EPR signals could have a very strong dependence on the microwave source frequency in a way not consistent with the calibration of the spectrometer power output and transmission characteristics. It was also noted that these signal anomalies would change for the same sample in different quartz tubes. Any reduction of bandwidth over which the spectrometer operates predictably is highly significant to this work a study to investigate this variation was conducted.

The sample holder is configured as shown in **Figure 3.2.1** where a sample volume is shown contained within a sample tube. As shown in the figure the microwaves enter the sample holder from the top and travel through the sample until they reach a waveguide mirror at the bottom as shown. This mirror acts as a waveguide short such that the fields are reflected at this point, and the mirror position can be adjusted to minimise off-resonant transmissions of undesired source polarisation.

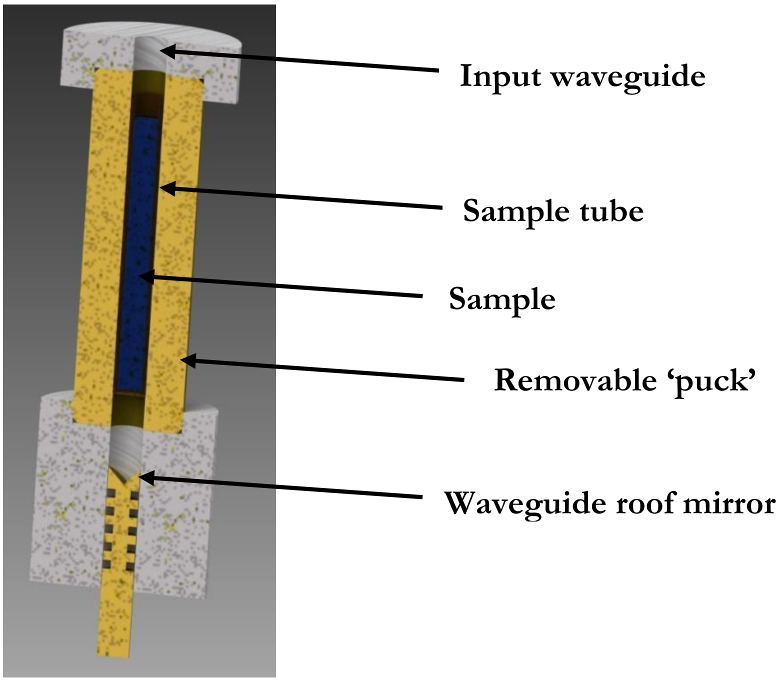

Figure 3.2.1 *Annotated CAD drawing of the HiEPR sample holder.*

The sample holder consists of input waveguide leading to a removable 'puck' which is a length of waveguide with a small and electromagnetically insignificant step at the bottom which holds any inserted sample tubes captive. At the other side of the puck waveguide is a further length of waveguide which contains the waveguide mirror.

With the advent of efficient and reliable 3D electromagnetic simulations packages it is possible to investigate the field interactions of the sample and the holder, looking for detrimental effects. As it is possible to change the materials quickly, it can be used to optimise the sample tube choice without having to make iterating physical measurements. The following simulations were conducted by taking the computer drawing of the sample holder, drawn to include the removable puck along with sample tube retaining the step and waveguide roof mirror. All of the sample holder simulations were conducted using the CST microwave studio[5] EM simulation package. All the simulations were conducted with the transient time domain solver and the mesh sizes were set to a size which included the smallest features within two mesh cells and sub-gridding was enabled to reduce the overall number of cells. The simulation was setup for the quartz tube and took into account the meniscus at the surface which will be present due to the water molecules being attracted to the glass surface as shown in **Figure 3.2.2 a**. A dielectric constant of 2 for the quartz tube, and 3for the water ice sample were used in the simulations [84].

---

[5] CST Computer Simulation Technology AG, Bad Nauheimer Str. 19, 64289 Darmstadt, Germany

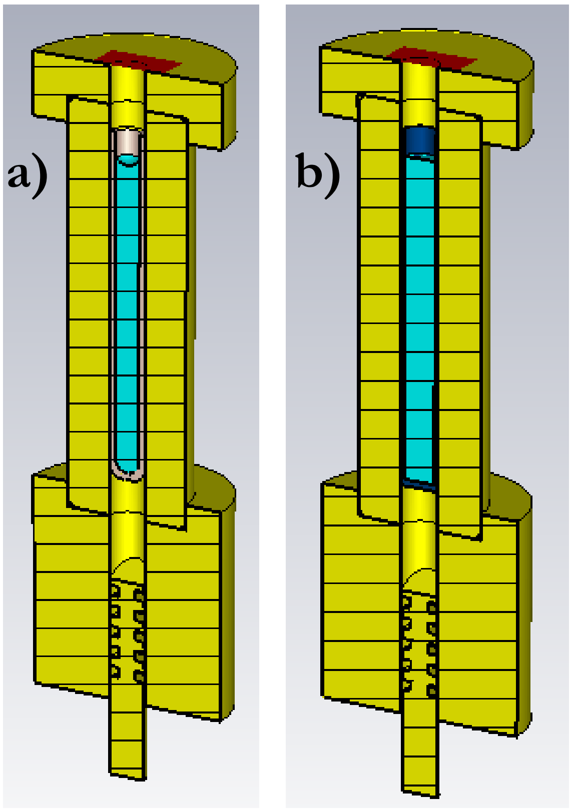

***Figure 3.2.2** CAD drawing of the HiPER sample holder for a) quartz tube b) FEP tube containing water ice sample with meniscus in the quartz tube case.*

Firstly the magnetic field component of the microwaves was modelled for the quartz tube setup to see how much of the field was being concentrated in the sample area and this is shown in **Figure 3.2.3 b**. When considering the fields propagating in a waveguide structure [85] it is useful to talk about the propagating fields in terms of waveguide modes. In smooth waveguide structure the natural mode set is the TE (transverse electric) and TM (transverse magnetic). In the empty waveguide region with 3 mm diameter only the fundamental TE11 mode can propagate, however once this waveguide becomes loaded with a dielectric material, in this case with a quartz tube and ice sample, higher order modes can propagate. When excited by the TE11 mode the next highest mode which can be efficiently scattered to is the TM11 mode. From EM simulations it is predicted that the TM11 can propagate in the sample holder with a 3 mm outside diameter, 2 mm inside diameter, quartz tube.

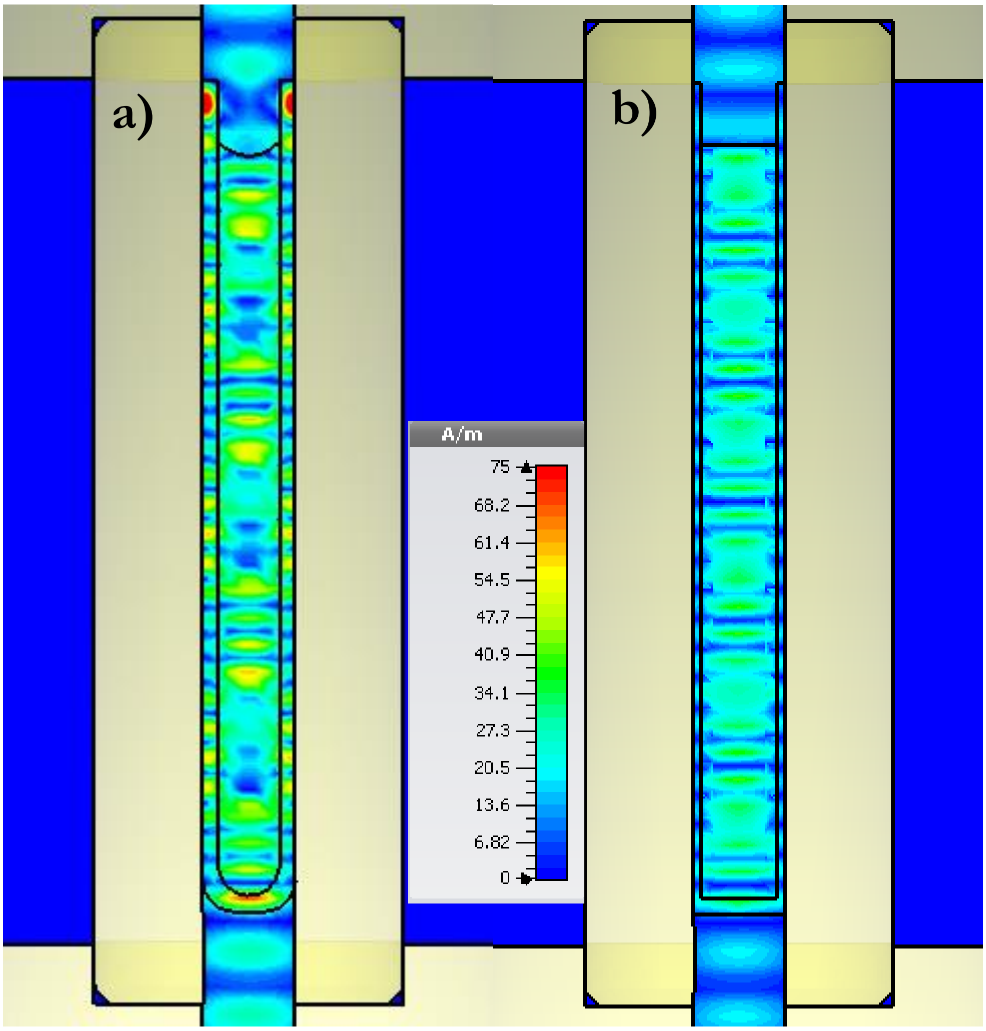

Figure 3.2.3 *EM simulation at 94 GHz of the HiPER sample holder showing magnetic field component for a) quartz tube b) FEP tube containing water ice sample.*

What was immediately apparent from the simulations is that the top of the quartz tubes present a dielectric discontinuity to the microwaves resulting in a significant field concentration at the entrance of the quartz tube, which cause a significant excitation of the TM11 mode. As this TM11 mode can only propagate efficiently inside of the sample tube region it becomes a trapped mode, and as the tube is several wavelengths long this mode can resonate at particular frequencies [86]. This resonance is evident in the EM simulation with a complicated field amplitudes across the sample area which has constructive and destructive nulls and peaks. A consequence of trapped modes is they can lead to modal resonances which lead to sharp increases in insertion loss at particular frequencies, and these resonances are highly sensitive to the exact physical structure of the tube and frozen sample and it is difficult to accurately predict their frequency. In an EPR spectrometer the resonances will result in a narrow band resonator which will reduce the desired flatness and effect the isolation between the orthogonal microwave polarisations, essential to the protection of the spectrometer and low dead time. This is consistent with the observations made on EPR samples contained in quartz sample tubes. To minimize the effect of these trapped modes there is significant benefit in using a tube constructed of a material with a lower dielectric constant, presenting a smaller dielectric discontinuity at the top of the tube and lowering the probability of exciting the TM11. One such material is FEP and tubing made with this material is readily available. FEP also has the advantage of being hydrophobic and having a negligible meniscus. The benefit of having reduced meniscus is in the sample freezing. Freezing a sample in a hydrophilic quartz tube may lead to micro cracks occurring in the frozen water/glycerol glass due to thermal stresses induced during cooling by differential material contraction between the sample and the tube in addition to the adhesive forces of the hydrophilic surface. A hydrophobic plastic tube will inherently reduce the stress on the sample by reduction in the adhesion forces between the sample and the tube, and reduction in the stresses on the water/glycerol glass will drastically reduce the occurrence of fracturing in the sample glass [87].

The second simulation of the magnetic field of the microwaves using the proposed FEP plastic tube as shown in **Figure 3.2.2 b**. The result of this simulation is shown in **Figure 3.2.3 b**.

In contrast to quartz the FEP tube has a much reduced interaction with the microwave field at the tube entrance due to the lowered dielectric constant and the microwave field in the sample area is significantly more uniform than in the quartz case. The field uniformity compared to the quartz tube case is due to the reduction of the TM11 mode excitation and modal resonance effects.

To compare the frequency dependence of modal resonance effects, which was the main concern in finding an alternative to quartz tubes, a simulation of the S11 parameter was made. S11 in this sample configuration is a measurement of the insertion loss of the sample holder, how much power is dissipated in the sample area. If a sample holder has an S11 value of 0 dB then there is no power lost relative to the power incident on the sample holder from the microwave source. This means the microwave power returns through the waveguide at the top of the sample holder. As the simulations considered the waveguide to be aluminium there will be some intrinsic microwave power loss in the sample holder even in the absence of the sample and tube. A plot of the S11 simulation for both the quartz and FEP plastic tube are shown in **Figure 3.2.4**.

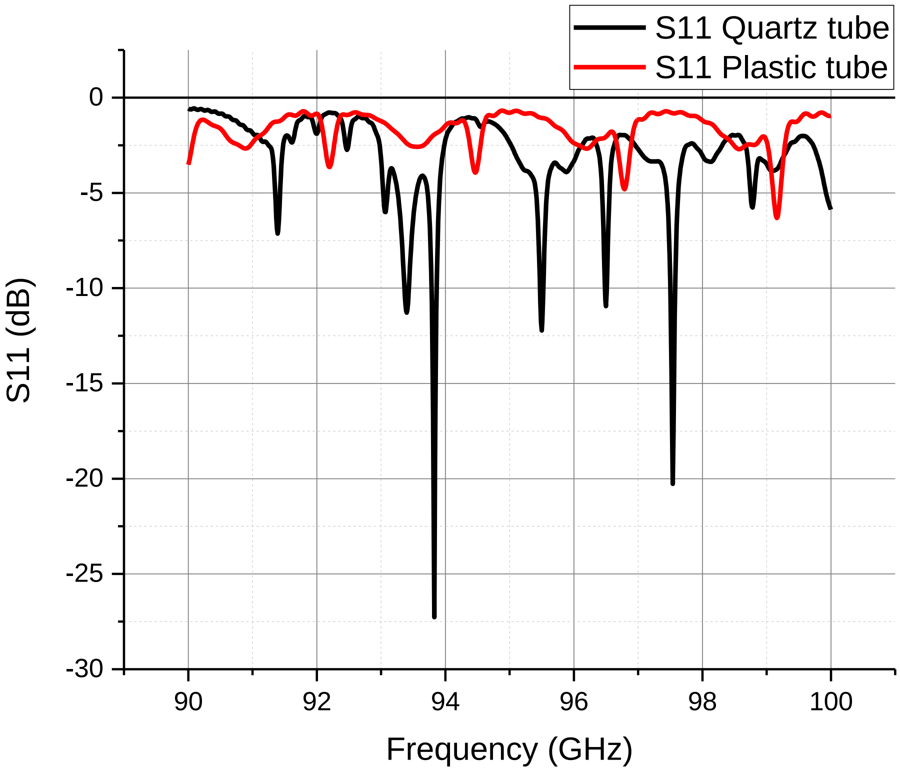

***Figure 3.2.4** Comparison of simulated S11 as a function of frequency for the HiPER sample holder with a quartz tube and FEP tube inserted, both containing water ice.*

As suggested by the field plots of the quartz tube there are strong field interactions and TM11 mode excitation which lead to trapped mode resonances in the sample area, which may cause the effective B_1 field at the sample to increase or decrease depending on the relative phase and amplitude combinations of the TE11 and TM11 modes, leading to unpredictable field patterns. The FEP plastic tubes by contrast have a relatively flat response with no strong resonances, again evidencing that they are more suitable material for the sample tubes and will lead to more predictable and reliable EPR measurements using the HiPER spectrometer.

3.3. MEASUREMENT PROTOCOL FOR PELDOR

All of the work presented in this chapter has the purpose of producing repeatable and reliable PELDOR measurement results which can be quantitatively analysed. Having investigated the relevant instrumentation the experimental protocol should also be optimised.

The process of loading sample tubes into the HiPER sample holder when at cryogenic temperatures differs from a more traditional EPR resonator based cryostat due to sample holder access. In the resonator based cryostat there is normally an access port to the sample area of the resonator and the sample can be placed removed and exchanged even when the cryostat has been cooled to cryogenic temperatures. However, in the HiPER sample holder configuration the only sample access is by removing the sample holder, and the attached waveguide, entirely from the cryostat. Any attempt to load a sample which has been flash frozen in liquid nitrogen to 77 K will inevitably be exposed to a jump in environment temperature before it is loaded even if the cryostat has been pre-cooled. It has been suggested that during the sample freezing process microscopic cracks to develop in the frozen glass sample which can interact with the electric field component of the microwave field and scatter into higher order evanescent modes, increasing sample loss or scatter to the TE11 mode with orthogonal polarisation. As previously mentioned the hydrophilic nature of quartz tubes is likely to exacerbate cracks developing during freezing compared with hydrophobic plastic FEP tubes. Literature of cryogenic storage of biological material [87] has suggested that an annealing process of raising the sample temperature to close to its glass transition and then cooling to the measurement temperature of 60 K allows the sample to stabilise and anneal cracks. The author is aware of evidence for the increase rate of micro cracks in quartz tubes compared with FEP tubes, where optical inspection of the samples after flash freezing in liquid nitrogen showed the sample in FEP tubes would freeze to be optically transparent, whilst the quartz tube would freeze to being opaque. Further experimental evidence of the influence of micro cracks developing may be possible by performing a large bandwidth VNA measurement of the sample holder in cryogenic conditions. However, this is a technically challenging experiment. Yet there has been an improvement in measurement repeatability of both the flatness in measured effective B_1 fields across the bandwidth. As such the developed procedure for loading glassy biological samples in the HiPER spectrometer for measurements at 60 K or lower is as follows:

1) The spectrometer cryostat containing the sample holder and the transmission waveguide is pre-cooled to 120 K prior to loading a sample in the holder.
2) The sample is flash frozen in liquid nitrogen inside a FEP tube in the desired mixture of water and glycerol.

3) Cooling of the cryostat is suspended once at 120 K.
4) A flow of helium gas is blown through the cryostat while the waveguide and is raised from the cryostat to allow access and the sample holder at the bottom of the waveguide, and the sample is quickly loaded to the sample holder. The helium gas reduces the amount of moist air entering the cryostat and freezing onto the piezo translation stages which control the waveguide mirror position.
5) The waveguide and sample holder are lowered back into the cryostat which is resealed and evacuated when the helium gas flow is shut off.
6) The cooling of the cryostat is resumed until a temperature just below the glass transition of the sample is reached (for 50/50 water glycerol ~110K is suitable) and the temperate is held until stable. At this temperature internal stresses of the sample solution may have built up and require annealing.
7) The cryostat temperature is returned to ~200 K or until there is evidence that the sample is absorbing the microwaves indicating that the sample is transitioning through the glass transition. This is the initial process of the sample annealing.
8) Once the sample has reached the glass transition cooling is resumed to the desired measurement temperature.

Once the cryostat has been cooled to the desired measurement temperature then the spectrometer microwave source is configured to transmit CW

94 GHz. One of the initial requirements is to carefully align the corrugated waveguide leading to the sample to maximise power being coupled from the quasi optic beam to the waveguide, and simultaneously minimising the amount of, non EPR, transmit signals being reflected into the orthogonal detection polarization. This improves the receiver sensitivity and protects the receiver front end. This receiver protection is very important in high power pulsed measurements where large power arriving at the receiver mixer and amplifiers can cause instant damage[6].

It is also necessary to measure the B_1 field for each microwave source frequency used during an experiment to account for different sample materials and quasi-optic alignment as well as monitoring the equipment for problems. However, measurements so far have not deviated significantly from the presented calibration results.

3.4. CONCLUSIONS

The characterisation of the spectrometer over its operating bandwidth, particularly the spectral bandwidth of nitroxide spin labels used in this work, are vital to quantitative studies of orientation selective PELDOR measurements. The spin system will respond differently depending on the strength of the microwave field and this can only be taken into account through prior measurement and characterisation.

---

[6] The author has observed this first hand.

This work shows FEP to be a suitable material to make EPR tubes for the non-resonant sample holder configuration where the tube and sample are exposed to both the electric and magnetic field components of the microwave source.

Analysis presented in later chapters takes this B_1 field strength distribution into account where relevant. Characterisation of the spectrometer and EM simulations of the sample holder has led to significant improvements in the experiment reliability and repeatability. Careful choice of tubing material can reduce modal resonances which might occur in non-resonant sample holders.

Chapter 4 HIGH FIELD EPR PELDOR SIGNAL SIMULATIONS

The PELDOR signals measured using orientation selective high field EPR, an example signal is shown in **Figure 3.4.1**, cannot be directly inverted to give the parameters which define the signal, instead requiring some form of model fitting to recover these parameters. To correlate the orientations of spin labels it is also required to make several orientation selective PELDOR measurements, usually 6 or more, correlating between the spin label principal axes by selective pulse excitation. Models can be constructed for the simpler case of two spins but also a cluster of many spins, describing their relative orientation to each other and their relative spatial position. Fitting models to experimentally obtained PELDOR signals requires an expression which allows for simple forward calculation for a given model, and these calculations have to be computationally efficient such that the fitting can be conducted in a useful timescale.

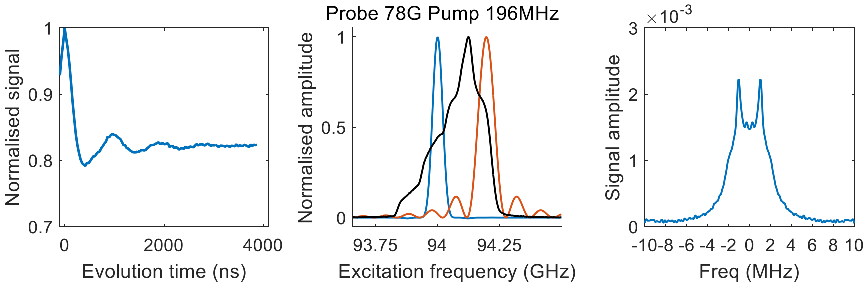

Figure 3.4.1 *A typical orientation PELDOR signal (left), with the pulse excitation profiles used for the PELDOR experiment (middle) and the frequency domain representation of the PELDOR signal (right).*

Although some currently available EPR spin simulation packages such as EasySpin and Spinach [88] can perform PELDOR signal simulations, they do not perform the simulations from first principle propagation of the spin system and can take considerable computational effort. These sample signals can be calculated instead by using approximate signal expressions which have been derived from the spin Hamiltonian assuming the simple spin ½ electrons and only a mutual dipole-dipole interaction. This takes considerably less computational effort, however, there are no obviously available simulation codes for orientation selective PELDOR signals. Even if such codes did exist, the particular bandwidth and B_1 field distributions of available high field pulse EPR spectrometers vary dramatically enough that codes would need to be highly customised. For this reason, as a precursor to the experimental work presented, a simulation code was written and optimised gradually over the course of its application.

This chapter will present the general PELDOR signal expressions used in this work and the computational framework used to simulate orientation selective PELDOR signals, highlighting some of the limitations and their applicability to this work. Models used in the studies presented in later chapters are built upon a general model which is described in this chapter.

4.1. PELDOR SIGNAL AND LIMITATIONS

A PELDOR signal expression for two spin labels can be derived from the spin ½ Hamiltonian presented in chapter 2.2 to give the PELDOR signal **Equation**

4.1.1 as presented in chapter 2.4, which would be observed for an isolated pair of electron spin, A and B, separately excited by the observer and pump pulses respectively.

$$I_{intra}(t) = I_0 \cos(\omega_{DD} T_{evolve})$$

Equation 4.1.1

$$\omega_{DD} = \frac{\mu_0 \gamma_1 \gamma_2 \hbar}{4\pi r^3}(1 - 3\cos^2\theta)$$

Equation 4.1.2

The PELDOR signal expression **Equation 4.1.1** is only for the optimal case of two spins excited by the pulses separately, but can be expanded to include efficiency of exciting the spins with each pulse, the pulse overlap and the interaction of multiple spins in the cluster. A detailed derivation of these terms has previously been made, but a brief discussion will be presented here.

The first consideration should be given to quantifying the spin echo magnetisation resulting from the action of observer and pump pulses [89]. The three observer pulses, π/2-> τ_1-> π-> τ_2-> π, produce the x-component spin echo magnetisation

$$Observer M_x = \frac{\gamma B_{1A}}{\Omega_A} \sin\left(\Omega_A t\pi/_{2}\right) \frac{\gamma^2 {B'_{1A}}^2}{2{\Omega'_A}^2} 1 - \cos\left(\Omega'_A t\pi/_{2}\right) \frac{\gamma B'_{1A}}{2\Omega'_A} 1 - \cos\left(\Omega'_A t\pi/_{2}\right)$$

Equation 4.1.3

$$B'_{1A} = 2B_{1A}$$

$$\Omega_A = \gamma^2 {B_{1A}}^2 + (\omega_{observer} - \omega_{resonance})$$

$$\Omega'_A = \gamma^2 {B'_{1A}}^2 + (\omega_{observer} - \omega_{resonance}).$$

Equation 4.1.4

Here the subscript A indicates the spin which the observer pulse is acting on. The strength of the microwave magnetic field component on the A spin is given by B_{1A}, γ is the gyromagnetic ratio for the electron, Ω_A is the Rabi frequency which is essentially the efficiency of the microwave magnetic field at changing the spin state. The pulse length in the expression is kept constant as $t\pi/_2$ the $\pi/2$ pulse length. As the final two pulses in the observer sequence are π pulses the B_1 in the expression is doubled such that the values of B'_{1A} and Ω'_A change for the field strength and Rabi frequency respectively.

The effect of the pump pulse in the PELDOR experiment is to flip the state of the spin B. An expression can again be found for the efficiency of the pump pulse on the spin

$$PumpM_z = \frac{\gamma^2 {B_{1B}}^2}{2{\Omega_B}^2} 1 - \cos(\Omega_B t_\pi)$$

Equation 4.1.5

$$\Omega_B = \gamma^2 {B_{1B}}^2 + (\omega_{pump} - \omega_{resonance}).$$

Equation 4.1.6

The terms in the expression have the same meaning as before, with the exception of the subscripts changing to correspond to spin B and the pulse length and B_{1B} field can be different from the values used in the observer pulses.

We can now assemble an expression of the dipolar coupling modulation on the PELDOR signal considering the efficiency of both pulses on a pair of spins A and B

$$u_{signal} = ObserverM_x(SpinA) \times PumpM_z(SpinB)\ .$$

Equation 4.1.7

However, if there is any pulse overlap this will destroy the coherence of the spin echo, and this is accounted for by weighting this contribution by the amount of overlap seen by each spin

$$u_{signal} = ObserverM_x(SpinA) \times (1 - PumpM_z(SpinA)) \times$$
$$PumpM_z(SpinB) \times (1 - ObserverM_x(SpinB)).$$

Equation 4.1.8

The value of u_{signal} gives the magnitude of the modulated PELDOR signal component and scales the oscillation, and this is added to the unmodulated echo amplitude to give

$$I_{PELDOR\ A,B}(t) = ObserverM_x(SpinA) + u_{signal}(\cos(\omega_{DD}T_{evolve}) - 1).$$

Equation 4.1.9

To calculate the signal for a sample the expression needs to be averaged over the case where spin A and spin B are swapped, all magnetic field directions (if calculating a powder average signal) and averaged overall all the conformations in the model.

It can be shown that this signal can be expanded to the case of N spins in a cluster and the PELDOR signal expression can be given as

$$I_{PELDOR\ A,B}(t) = \sum_{SpinA}^{N} \prod^{N}_{\substack{SpinB,\\ SpinB \neq SpinA}} \begin{matrix} ObserverM_x(SpinA) + \\ u_{signal}(\cos(\omega_{DD}T_{evolve}) - 1) \end{matrix},$$

Equation 4.1.10

where, again, spin A is the observer spin and spin B is the pump spin. The factorisation can be made for the signal expression when there are >1 pump spins due to the fact that the mutual dipolar coupling between pump spins do not manifest in the evolution of the observer spin coherence as long as the pump pulse length is short compared with the inverse of the pump spin dipolar coupling strengths [80].

This signal expression requires some other assumptions which must be met for it to be valid. A short discussion of relevant assumptions will be made. The work, and assumptions, presented in this chapter will consider the signal expression applied to systems of nitroxide spin labels, which are spin ½.

One assumption is that the observer pulse sequence should excite only one of the spins, if two spins are excited then the signal would be an echo which has a rapid decay relative to the timing of the observer pulses (this is normally kept static throughout the PELDOR experiment), modulated over this time by the dipolar coupling, according to instantaneous diffusion effects. The resulting signal from this case will have a small contribution to the total signal, however this can still distort the signal analysis if not taken into account. A discussion of this contribution has been presented in recent publications by Salikhov [74, 75]. However, this condition of exciting only one spin with the observer pulses is usually easily met for clusters of small numbers of spins in the orientation selective PELDOR experiments made at W-band where the percentage of spins excited by the pulses is limited by the pulse lengths and spectral width of the radical to being <20% of all spins. In the case of only one spin excited by the observer pulses, spin A, the signal will only be modulated by the dipolar coupling if the other spin B state is also flipped by the action of the pump pulse, giving the expected signal expression. If spin B is not flipped efficiently by the action of the pump pulse the contribution to the PELDOR signal will just be an unmodulated refocussed echo, and this should be taken into account in calculations of the PELDOR signal.

Another assumption which needs to be met is the dipolar coupling strength ω_{DD} should be weak relative to the difference in the resonances of the spins such that the pseudo-secular term of the electron-electron dipolar Hamiltonian can be neglected. A discussion of this term is given in chapter 2.2. This approximation can be safely made in nearly all experiments where the nitroxide spin label is used, as its spectral width is ~400 MHz, and typical dipolar coupling strengths are <5 MHz. However, if the spatial separation of the spin labels is very small resulting in a large dipolar coupling strength or the spin label spectrum is very narrow [90] then this term needs to be considered, particularly if the spin labels are have rigid relative orientations which would result in a higher probability of spins having similar resonances .

These assumptions apply in the same way to PELDOR signals observed from clusters of multiple spins, where the assumptions should be met between each spin and every other in the cluster. It should be noted that to excite only one spin in a larger cluster of spins will require the percentage of total spins excited by the observer pulses to be reduced, independent of the number of spins excited by the pump pulse. Although as discussed in Chapter 6 it is of benefit to reduce the fraction of pump spins excited by the pulse.

4.2. GENERAL MODEL OF RIGID ORIENTATION SPIN LABELS

A very general model for describing spin labels in a cluster for simulating the PELDOR signal will be briefly discussed. It is often useful to modify the model for specific problems and this has been done in the applications presented in this thesis. However, for the task of programming a PELDOR signal simulation code it is useful to parameterise using the most general model, and code new problem specific models to interface with this general case.

The model is specified as a group of spins which are indexed from 1 to N with each spin having a position and rotation relative to spin 1, **Figure 4.2.1**. The definition of the rotation has a number of possibilities, however in this work the Euler angle ZYZ convention will be used and its definition will be discussed in more detail in Chapter 5 . The simulation code input uses rotation matrices, such that the Euler angles need to be converted. Several well established MATLAB libraries exist for this task and the SpinCalc package [91] was used. There also needs to be a defined angle for the static magnetic field relative to the cluster of spins and this is defined by in spherical co-ordinates by angles (θ,φ).

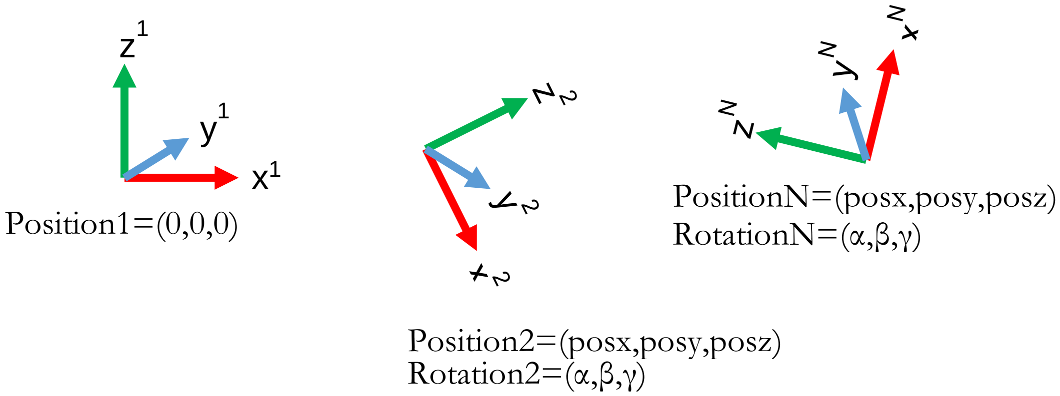

Figure 4.2.1 *Generalised model of spin labels parameterised with Cartesian positions and Euler rotation angles (α,β,γ).*

4.3. SIMULATION ALGORITHM

Using the presented PELDOR signal expression and the general model we can present the calculation of the signal as an algorithm. The algorithm is be presented as a block diagram, **Figure 4.3.1**, and was implemented for this work in MATLAB for quick development with extra routines written in C to improve calculation performance. The external matrix multiplication library MMX [92] was used and is discussed in a following chapter 4.4.

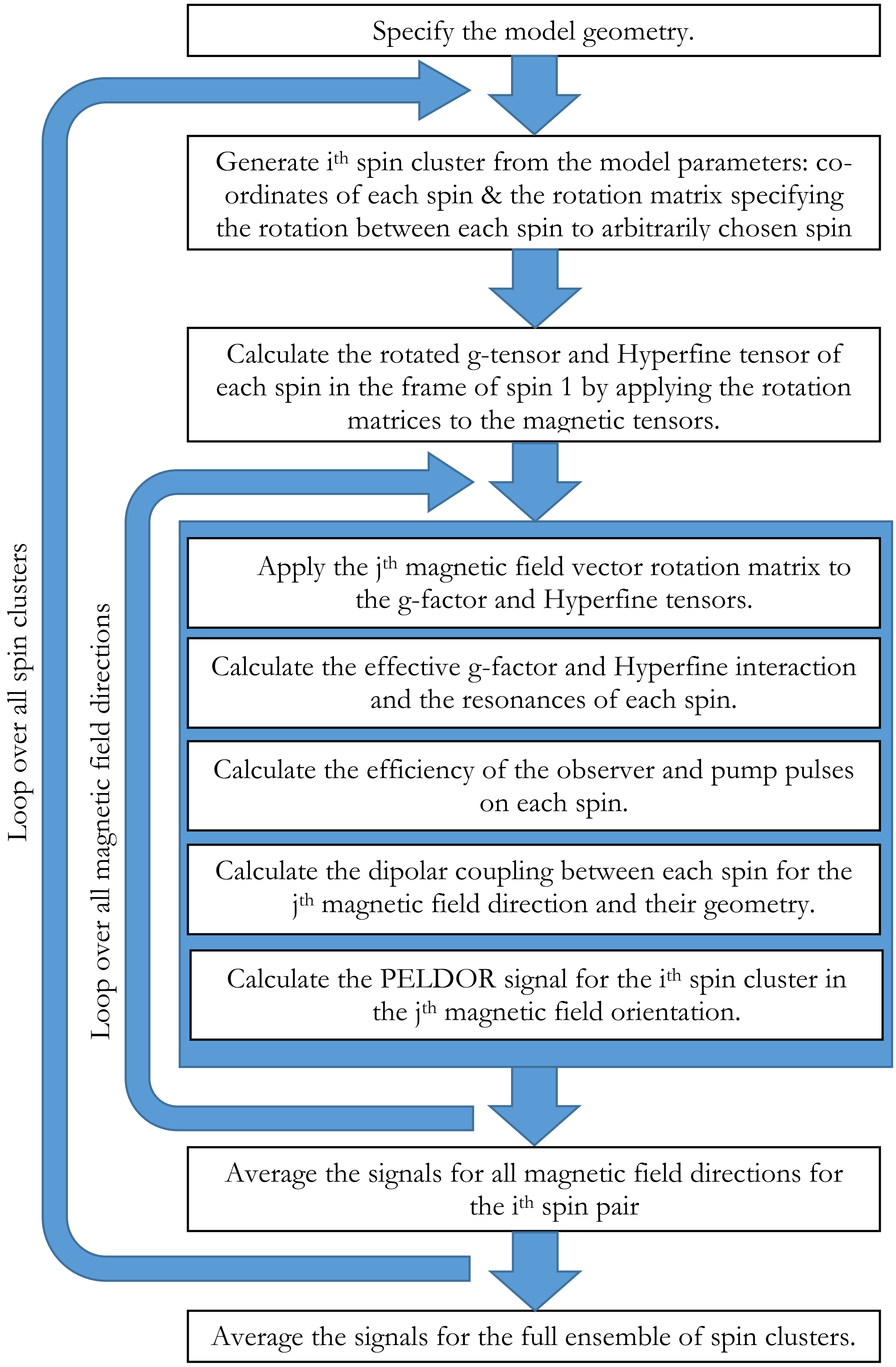

Figure 4.3.1 *Block diagram of the PELDOR simulation code algorithm.*

4.4. COMMENTS ON IMPLEMENTATION USING MATLAB

The simulation code developed for this work made use of several optimization routines which aimed to reduce the computation time of the forward calculation of PELDOR signals. Several of the key ideas which had a significant impact on the calculation time will be briefly discussed here.

4.4.1. Multi-dimension arrays and large scale matrix multiplication

The algorithm as shown in **Figure 4.3.1** has several loops, and within the PELDOR signal calculation there may be additional loops required to average over nuclear spin states or multiple spins in a cluster. Although some compiled programming languages, such as C, include optimizations where the compiler will look for loops and attempt to optimize them for multi-core CPU the MATLAB scripting language generally cannot optimize looping code at runtime. However, the underlying linear algebra libraries of MATLAB, namely LAPACK, have strong parallelized optimizations built-in. These optimizations can be taken advantage of by expanding all of the originally looping operations into large matrix operations expanded across a number of dimensions. However, the current implementation of the matrix operations in MATLAB at the time of writing do not include sensible support for large dimension arrays. Libraries of compiled matrix operation functions for large dimensions have been written and are freely available, with the best performing library being MMX, typically giving a 3 times performance improvement over native

MATLAB functions on the Intel i7 processor used in this work. These have been detailed previously in the MMX manual. The author observed an overall 5 times time reduction in PELDOR signal calculation by utilizing the MMX library.

4.4.2. Computation of time domain signals via the frequency domain

It was possible to achieve a further reduction in computation time by performing the PELDOR signal calculation in the frequency domain and transforming to the time domain in the last step. This is achieved by calculating the dipolar coupling frequency for each signal and an associated amplitude calculated from the pulse excitations, as shown in the block diagram. These components are then binned into frequency bins, chosen to give the desired number of time points in the final signal. The binned frequency components produce the total dipolar spectrum for the PELDOR signal and an inverse-FFT operation transforms this to the time domain PELDOR signal which is measured.

To further reduce the computation time the bin widths and number of bins can be chosen to correctly sample the dipolar modulation frequencies and then zero-padded to achieve the desired number of signal time points.

4.5. CONCLUSIONS

A description of the PELDOR simulator which was used in this work is given along with comments on the implementation of the algorithm using MATLAB.

The optimized code has enabled the use of global optimization to simultaneously fit several PELDOR experiments to models in a 24 hour timescale. Use of advanced MATLAB matrix operation library MMX for matrix multiplication and signal calculation using inverse FFT offer significant time reductions in calculation time, but this requires large memory to store the large matrices during the calculation. The general input to the signal simulation code allows for problem specific models to be built on top of the presented code, and these models will be presented in later application Chapter 5 and Chapter 6 .

Chapter 5 HIGH-FIELD EPR ORIENTATION STUDIES OF TWO SPIN LABEL SYSTEMS

The work presented in this section is based on a journal article manuscript accepted for publication in PCCP, DOI: 10.1039/C5CP04753F,

"The use of The Rx spin label in Orientation Measurement on Proteins, by EPR".

The first author manuscript was co-authored with:

Michael A. Stevens[a1], Johannes E. McKay[b1], James L.S. Robinson[a], Hassane EL Mkami[b], Graham M. Smith[b] and David G. Norman[a2]

[a]Nucleic Acid Structure Research Group, College of Life Sciences, University of Dundee, Dow Street, Dundee DD1 5EH, UK.

[b]School of Physics and Astronomy, University of St Andrews, St. Andrews, KY16 9SS UK

1 M.A.S. and J.E.M contributed equally as lead authors to this work

J.E.M contribution to this work was the high-field EPR measurements, analysis of the molecular dynamics simulations, all simulation of PELDOR signals, the analysis of high field PELDOR signals and construction of constraints for use with structure determination package XPLOR-NIH.

This chapter will present an investigation into PELDOR experiments of the Rx spin label attached to protein biomolecules for determination of relative orientation of the underlying structure. The structure and dynamics of the spin label Rx, in relation to the underlying protein Vps75, was examined in order to determine the feasibility and optimum conditions for distance and orientation measurement by PELDOR experiments. Analysis of molecular dynamics (MD) simulations were used to investigate the suitability of different labelling strategies for orientation selective PELDOR studies. W-band PELDOR measurements were used to demonstrate and determine the relative orientation of Rx spin labels at different labelling sites, demonstrating that Rx is a suitable spin label for generalized orientation measurements on proteins. These results were compared to the MD simulations and used in combination with the structure determination package XPLOR-NIH [93] to investigate the application of orientation PELDOR results for biomolecule docking and structure solving.

5.1. SPIN LABEL RX

The majority of current protein spin-labelling studies have used the MTSSL spin-label, **Figure 5.1.1**, which has proven to be an excellent choice for the measurement of distances between spin labels. Because the conformational distribution of a surface exposed MTSSL label can often be predicted and the distance measurement can be transferred to the underlying protein for use in the refinement of macromolecular structures. Recently there have been a number of studies in which the utility of a bipedal spin label Rx [62, 94-97], **Figure 5.1.1**, has been described. Having two attachment points to the underlying protein, the Rx spin label is intrinsically more restricted in relation to the underlying protein structure. The Rx label has been used to exploit the increased spatial definition, relative to the MTSSL label, such that it might provide more accurate distance measurements on difficult targets such as membrane proteins. It has been demonstrated that at high frequencies PELDOR could be used to measure not only distances but also relative label orientation, several studies have investigated the measurement of this spin-spin orientation and addressed some of the difficulties inherent in the measurement, both in proteins and DNA. Because the solvent exposed MTSSL spin label is normally highly dynamic at non cryogenic temperatures, and when flash frozen takes a large spread of conformations, it is infrequently a good subject for orientation measurements and its use in this way has been restricted to cases in which the spin-label is severely restrained by specific interactions [98]. Due to its more restricted mobility, the Rx label is a candidate for orientation measurements. Although restricted conformation would make orientation measurement potentially viable, even in fully solvent exposed positions, in order to use label-label orientations to define the underlying protein structure one must understand the conformation of the label, in relation to the protein structure to which it is attached.

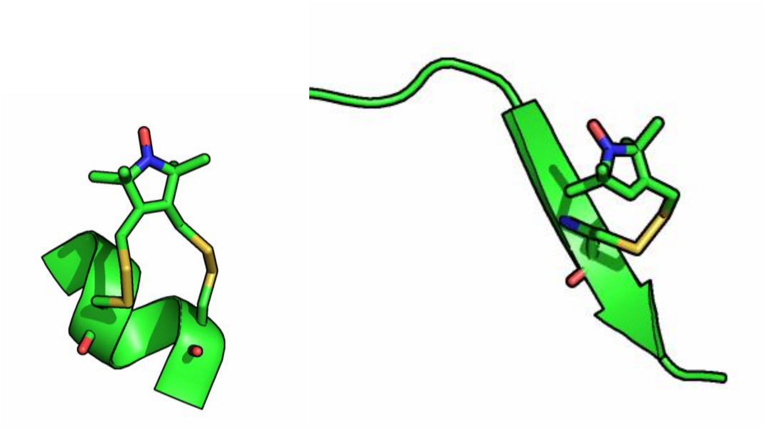

Figure 5.1.1 *Cartoon of Spin label Rx attached to alpha helix (left) and MTSSL attached to beta sheet secondary structure (right).*

5.2. ORIENTATION SELECTIVE PELDOR AT W-BAND

The general principle of orientation selective PELDOR measurements is to selectively excite electron spins which have a particular orientation relative to the magnetic field vector direction. This is possible when a molecule containing unpaired electron has an anisotropy in its g-factor, or other anisotropic couplings which introduces an inhomogeneous broadening, causing the g-factor and coupling strengths to depend on the orientation of the molecule relative to the magnetic field. These anisotropies will give the EPR resonance of the spin a dependence on its orientation. Suitable g-factor anisotropy occurs in commonly used nitroxide spin labels such as Rx for orientation selective experiments at W-band. By measuring the electron-electron dipolar coupling of these orientation selected spins using the PELDOR experiment as described in earlier chapters it is possible to access the relative geometric configuration of the spins in a region of ~2 nm to 10 nm.

Orientation PELDOR measurements have mainly been conducted with high field EPR (>3 Tesla), although several groups have shown in special cases the possibility of measuring the relative orientation of spin labels using lower field EPR measurements at X-band and Q-band [48, 99, 100] where the field independent nitrogen hyperfine coupling dominates over g-factor anisotropy. The low field orientation selective measurements were in all cases reducing the complexity of the model by solving only for the inter-spin-label vector direction and either one or two angles defining the relative orientation of the two spin-labels. To solve for all of the relative rotation angles it is required to go to high field measurement where the g-factor anisotropy is fully resolved. However, one significant difficulty when making PELDOR orientation selective measurements on commercially available high-field EPR spectrometers is limited bandwidth. The orientation selective PELDOR experiment requires to excite selectively on different resonances, corresponding to different relative orientations of the spin label molecule, in the same experiment and for each excitation microwave field to have relatively constant magnetic field amplitude. The Rx and MTSSL spin label molecules used in the work have spectral widths of ~400 MHz, requiring the spectrometer to have a bandwidth of this order to excite, and correlate, all molecule orientations. As described in Chapter 3 the HiPER spectrometer is very suitable for this experiment.

5.3. MODELLING OF TWO RIGID SPIN LABELS FOR ORIENTATION SELECTIVE PELDOR EXPERIMENTS

To recover geometric information from PELDOR measurements of coupled spin-labels it is necessary to perform some form of analysis on a series of experimental signals. It is the case that it is not possible to analytically derive a function which inverts the signal to give geometric parameters directly and therefore an analysis methodology was developed for solving the geometric parameters from the PELDOR measurements by fitting to a model. This methodology will be presented. A general description of the simulation code used in this work is discussed in Chapter 4 .

For a model to define the case of two rigid spin-labels on a molecule there are 6 parameters which can fully describe their relative position, 3 angles to describe their relative rotation and a further 2 angles and a scalar distance to describe their relative position in space. A graphical illustration of this model excluding the magnetic field orientation is shown in **Figure 5.3.1**. In this model the alignment of the main applied magnetic field B_0 is described by a further 2 polar angles relative to spin A (not shown in figure), as all of the samples under study in this work are in disordered glassy matrix the signal will be averaged uniformly over these 2 magnetic field angles in spherical co-ordinates using optimised angle sets.

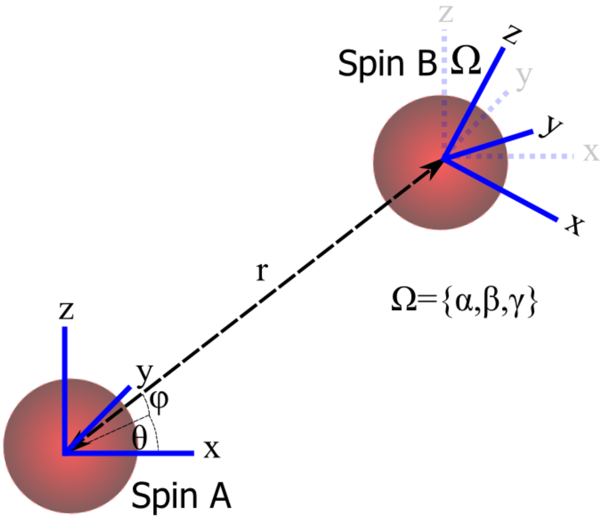

Figure 5.3.1 *Model of rigid spin pair. The model is parameterised with the position of Spin B relative to Spin A given by the spherical coordinates (r,θ,φ) and the relative rotation of the principal axes of Spin B relative to Spin A is given by the Euler rotation angles (α,β,γ).*

The 3 angles representing the relative orientation of the two spin-labels are denoted by **Ω**=(α, β, γ) where the angles are the 3 Euler angles given in the ZYZ convention respectively. A graphic of this rotation scheme is shown in **Figure 5.3.2**, according to this convention there are three consecutive rotations made to get from the initial frame, which will be called frame A and associated with spin A, to the final frame, which will be called frame B and associated with spin B. The three rotations are as follows:

A rotation is made around the z-axis counter-clockwise by the angle α such that the frame is rotated from $x^A,y^A,z^A \rightarrow x',y',z'$

A rotation is made around the new y'-axis counter-clockwise by the angle β such that the frame is rotated from $x',y',z' \rightarrow x'',y'',z''$

A final rotation is made around the new z”-axis counter-clockwise by the angle γ such that the frame is rotated from x”,y”,z” → A,B,C which will be referred to as x^B,y^B,z^B

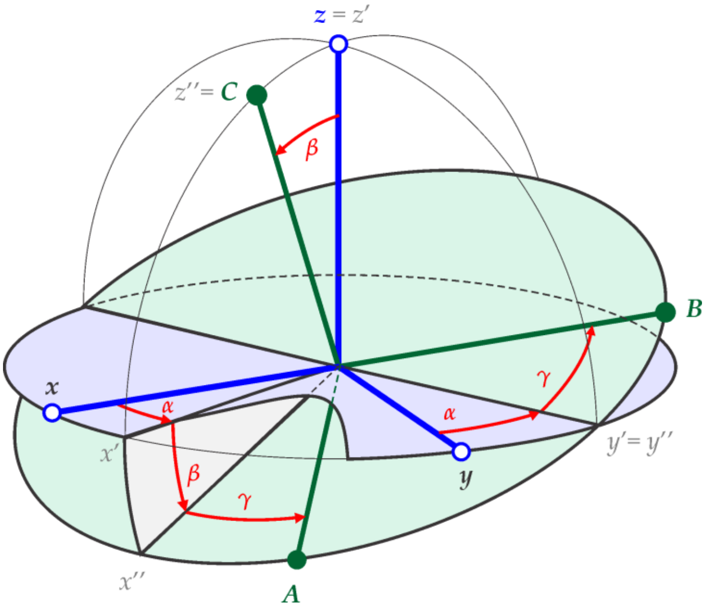

Figure 5.3.2 *Illustration of the ZYZ Euler angle rotation convention. Taken from EasySpin documentation Prof S Stoll [101].*

The two angles representing the relative position of the two spins (θ,φ), along with the distance separation r, specify the relative position of the two spin labels in space as shown in **Figure 5.3.1**. The angles (θ,φ) define the direction of the vector which connects the two spin labels in spherical co-ordinates. The frame used to define these angles is the frame x^A,y^A,z^A of spin A, with θ being the angle counter-clockwise from x^A in the x^A,y^A plane and φ being the angle away from the x^A,y^A counter-clockwise around y^A.

Often the case of fully rigid spin label pair will not actually exist for spin labelled biomolecules. To apply the presented model to these cases requires the addition of distributions around these values, such that each angle has an associated distribution width. In this work the normal distribution was used to describe the distributions of the different variables such that for the angles **Ω**=(α, β, γ), (θ,φ) and r there are the associated distribution widths (Δα, Δβ, Δγ), (Δθ, Δφ) and Δr.

It is note-worthy that there is a significant issue with the Euler angle rotation scheme there are cases of 'gimbal lock' which can create non unique angle cases. There arise for the cases when x^A, y^A and x^B, y^B are in the sample plane where there are combinations of two angles which can offer the same rotation. In the scheme of zyz euler angle notation $\beta=0$ when x^A, y^A and x^B, y^B are in the sample plane and α and β are not uniquely defined only $\alpha\pm\beta$. This situation is dealt with in this work by careful choice of the rotation library used in the analysis code which flags up the case of gimbal lock, requiring more careful inspection of the results.

5.4. SIMULATION AND FITTING ALGORITHM

All the analysis is based around orientation selection PELDOR signal simulation code which has been home-written using the MATLAB package described in Chapter 4 . The highly parallelized simulation code was used with 5000 orientation conformations and for each conformation of the spin label pair the B-Field orientations were averaged over a set of angles taken from the Repulsion 2-angle set [102] containing 700 angles. Where there was a uniform library of relative rigid spin label pair conformations the uniform ZCW 3-angle set [103-105] containing 6044 rotation angles was used.

The fitting algorithm used the genetic algorithm (GA) fitting functions included in the Global Optimization Toolbox MATLAB package toolbox. The fitting algorithm used the calculated RMSD between the experiment measured PELDOR signal and the current iteration PELDOR signal as a penalty function for fitting. The fitting algorithm was allowed to vary all of the angles in the model described through their full range, and the mean of the distance distribution was allowed to vary ±10Å from the starting value, which was derived from X-band measurements. Each of the angles and distance was given a distribution modelled as a normal distribution, which the fitting algorithm could vary up to a standard deviation of 90 degrees for the angles and 10Å for the distance distribution. The distance and angles were not correlated in the simulated model, it is assumed in this work that the spread in the orientation will result in a little variation between the distances for each conformer, although this will not be true in all cases.

5.5. CONSTRAINED SPIN LABEL RX STUDIED USING THE PROTEIN VPS75 AS A FRAMEWORK

A number of positions for attachment of Rx to proteins have been previously described. Six generic attachment positions, on protein secondary structure, that cover all available attachment types, that are restricted to defined secondary structure regions were identified and are shown in **Figure 5.5.1** and

Table 5.5.1. Defined secondary structures have several advantages as attachment points for spin labels in that they (β-sheets and α-helices) are relatively stable, providing a direct link between the spin-label and the body of the underlying protein. These regions are also predictable from amino-acid sequence data. Finally secondary structures in proteins maintain a reasonably constant distance relationship between side chains allowing the prediction of suitable attachment sites for Rx. The protein chosen for these studies was the histone chaperone Vps75. This protein is dimeric (at high salt concentration) [97] and contains suitable regions of α-helix and β-sheet. A number of crystal structures for Vps75 have previously been solved and the work reported here utilized the structure with PDB code 2ZD7.

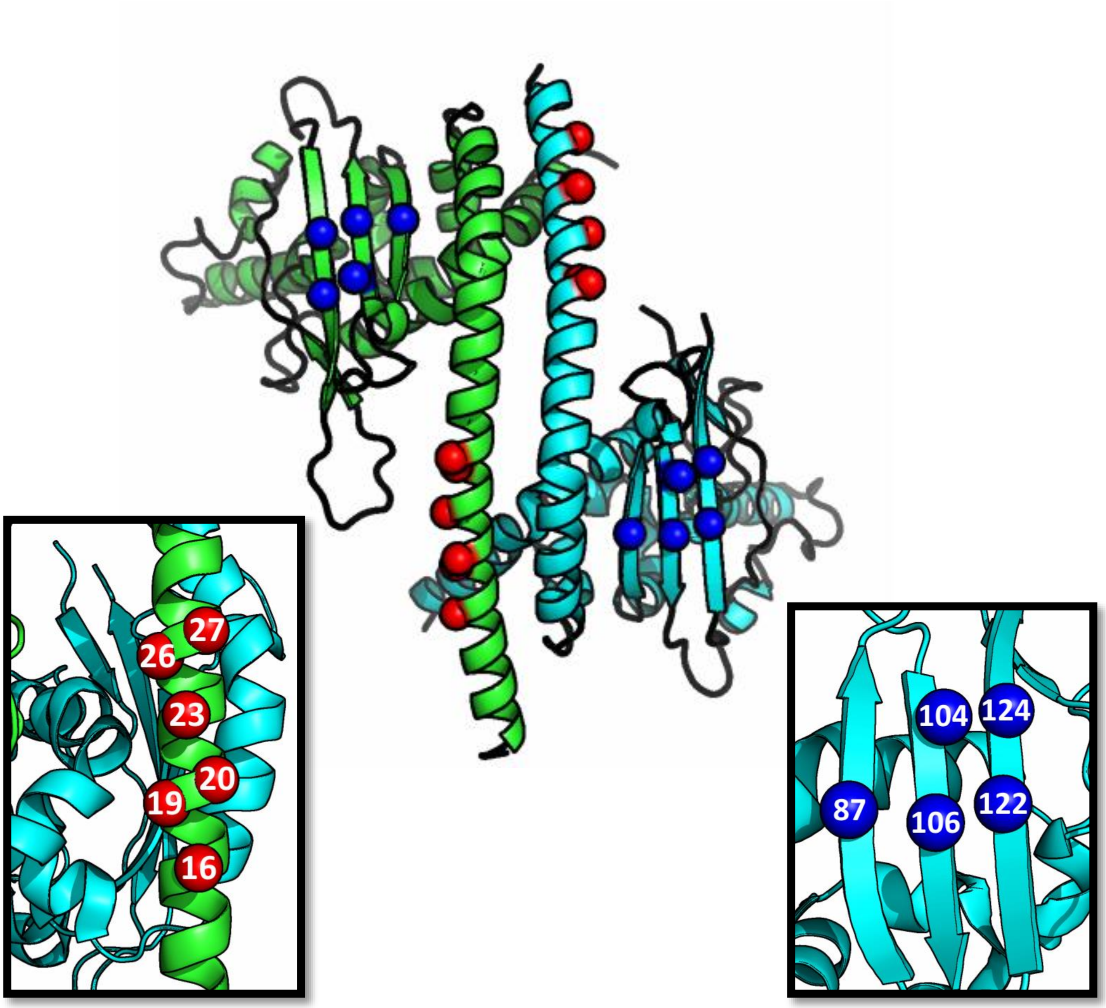

Figure 5.5.1 *Cartoon of the dimer protein Vps75 showing the two segments as green and light blue with labelling residues labelled. Labelling residue sites investigated in the study are shown in red for alpha helix and blue for beta sheet. Zoomed in boxes show the residue numbers of the sites for the crystal model (PDB 2ZD7).*

Secondary structure type	Residue sites labelled	Generic residue sites
α-helix	Residues 16 & 19 Residues 26 & 27	Residue i & Residue i+1
α-helix	Residues 16 & 19	Residue i & Residue i+3
α-helix	Residues 16 & 20 Residues 19 & 23	Residue i & Residue i+4
β-sheet	Residues 87 & 104 Residues 104 & 122	Residues diagonal across strands in a sheet
β-sheet	Residues 106 & 122 Residues 104 & 124	Residues perpendicular across strands in a sheet
β-strand	Residues 122 & 124	Residue i & Residue i+2

Table 5.5.1 *Table of labelling residue sites investigated in the study*

5.6. ANALYSIS OF RX SPIN LABEL MOLECULAR DYNAMICS SIMULATIONS FOR ORIENTATION SELECTIVE PELDOR EXPERIMENTS

To assess the suitability of the identified labelling sites for W-band EPR PELDOR orientation studies the results of molecular dynamics simulations were analysed for their orientation distribution. The molecular dynamic simulations were conducted by the Norman group at the University of Dundee using the XPLOR-NIH package, material and methods are supplied in Appendix. The MATLAB scripts used for analysis were written by the author and the analysis was performed by the author.

The angular distributions for each of the identified attachment sites were characterised by the relative rotation of the spin label to the secondary structure to which it is attached. Descriptions of the frame axes of the secondary structure used to define the rotations are shown in **Table 5.6.1** and in **Figure**

5.6.1. The origin of the spin label frame is the centre of the pyrroline ring. The axes of the spin label frame are the principal axes of the g tensor where the x-axis is collinear with the vector joining the nitrogen and oxygen atoms, the z-axis is perpendicular to the pyrroline ring with the y-axis being perpendicular to the x and z-axis.

	α-helix	**β-sheet**
origin	Average of the cα atom positions of each residue.	Average of the cα atom positions of each residue.
X-axis	Perpendicular to Y & Z-axis.	Perpendicular to Y & Z-axis.
Y-axis	Aligned along the cα atom positions of each residue.	Aligned along the cα atom positions of each residue.
Z-axis	Aligned on the plane defined by the cα atoms at the adjacent helix residues.	Aligned on the plane defined by the cα atoms of residues in the sheet pointing along the label direction.

Table 5.6.1

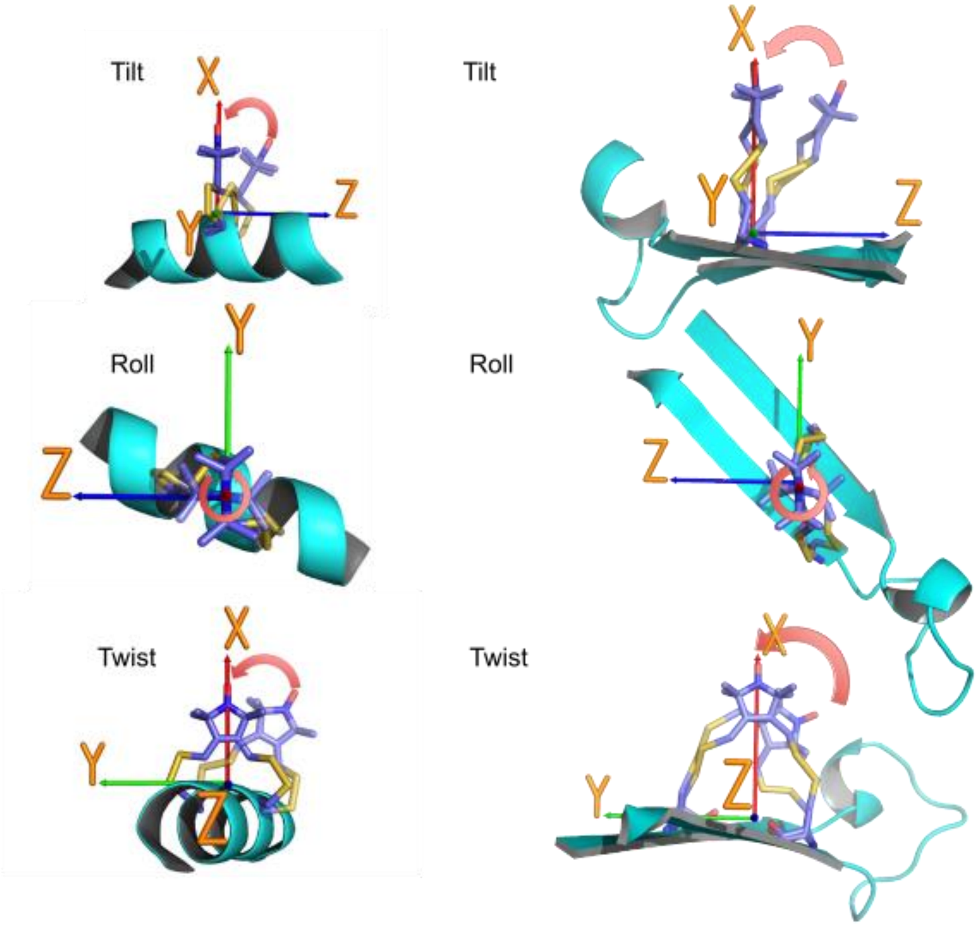

Figure 5.6.1 *A series of images representing the Tilt, Twist and Roll angles at the both the alpha-helix and beta-sheet sites. The arrows on the diagram show the angle and the motion of the spin label associated with each rotation.*

The angles were calculated by a MATLAB code written to automate the task. The code performed by calculating the rotation matrix which transforms the secondary structure frame to the spin label frame for each of the 2000 individual molecular dynamics simulation frames. These rotation matrices were then converted to the tilt-roll-twist angles (YXZ Euler angle format) which is shown in **Figure 5.6.1**. The resulting angles were then binned individually for the tilt, roll and twist angles to provide a density distribution. A Normal distribution was fitted to each case, where appropriate two Normal distributions were fitted to the density. The results of the binned angles and the fitted Normal distributions are shown in **Figure 5.6.2**.

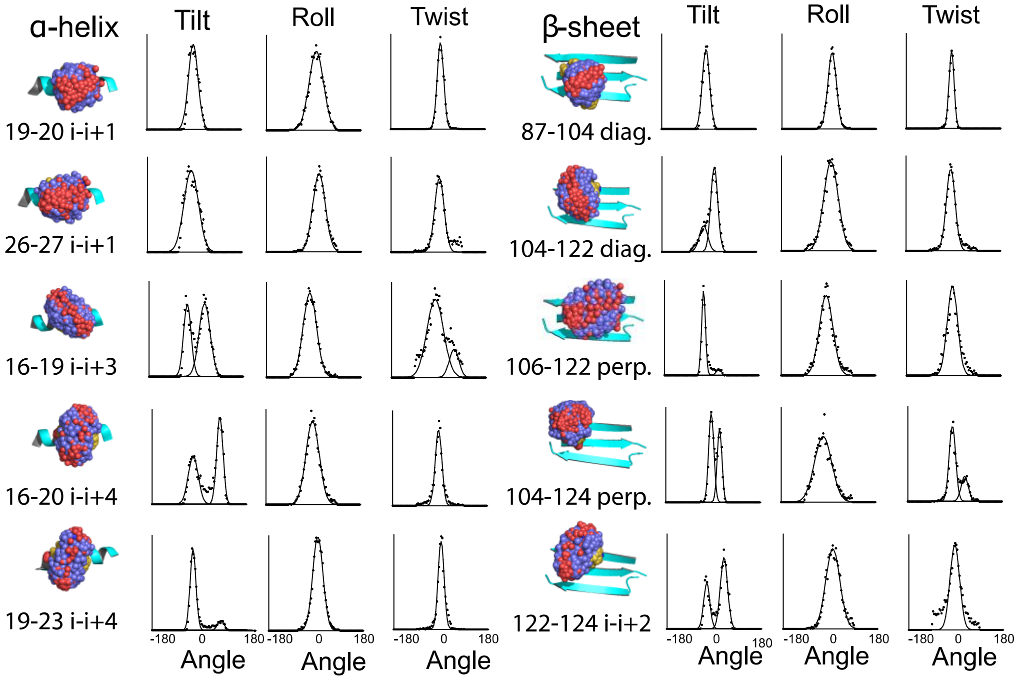

Figure 5.6.2 *Molecular dynamics angle distribution results of spin label Rx attached to different labelling sites on spin labelled protein Vps75. Underlying secondary structures shown as cyan coloured ribbons, oxygen of the nitroxide shown as red spheres, carbon atoms of the spin labels shown as blue spheres and sulphur atoms yellow spheres. The associated graphs show the extracted angle distributions for the spin labels in the order Tilt, Roll and Twist. Binned values are shown as dots and fitted Gaussian curves are shown as continuous lines. Angle distributions are shown from -180 to +180 degrees.*

The angle distributions for the α-helix attachment sites show that the attachments i-i+3 and i-i+4 are bi-modal, that is there are two distinct narrow populations of the spin label conformations suggesting that the label has a preferential state which has the spin label nitrogen-oxygen bond vector folding around the turns of the helix in each direction. In the case of the i-i+4 attachment sites these populations have a bias towards one population. This bias can be explained by clashes of the spin label with nearby residues, with residue L20 clashing in the 19-23 labelled simulation and residue A19 in the 16-20 labelled simulation. Figures of the label and adjacent residues for each case is shown in **Figure 5.6.3**. The clashes at each site are on opposite sides of the label hence the reverse in the bias shown in **Figure 5.6.2**.

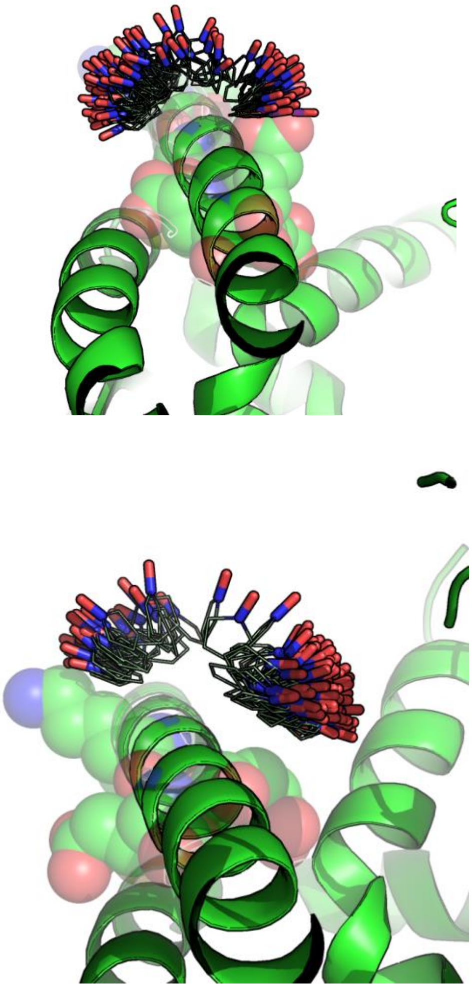

Figure 5.6.3 *Molecular dynamics frames of the spin label Rx attached using residue sites of type residue i to i+3 and residue i to i+4. Illustrating the effect of nearby residues restricting the available occupation of the Rx label.*

The α-helix attachment sites of the residues i-i+1, 19-20 and 26-27 are both mono-modal, having only one angle distribution, and have little variation between the two molecular dynamics simulations indicating that these sites would be most suitable α-helix attachment for orientation selective PELDOR experiments.

The β-sheet attachments sites had a lower consistency between the different simulations of the same site separation. The most mono-modal attachment sites are residues 87-104 and 104-122, which are diagonal residues on adjacent strands of the β-sheet.

The purpose of analysing the angular distribution from the molecular dynamics simulation of the Rx label at different sites is to assess their suitability for orientation selective PELDOR, where the experiment is measuring the relative rotation from one label to the other, along with their relative position. It is therefore useful to visualise the molecular dynamics results as the distribution of relative rotations from one label to its partner in the pair. This was achieved by taking each of the 2000 frames and calculating the rotation matrix from each label in one of the pairs to all of the positions simulated for the other spin label in the pair. This results in 4000000 different rotations which were then used to find the relative rotation of the x-axis (gxx) of the spin label principal axes in the pair and also the relative rotation of the z-axis (gzz). The x-axis in the case of the Rx spin label will be collinear with the vector of the nitrogen oxygen bond and the z-axis will be perpendicular to the pyrroline ring. The distribution of relative rotations of each axis for each attachment site is shown in **Figure 5.6.4**. The coordinate scheme used to plot the rotation angles is that of spherical coordinates, where Azimuth is the clockwise angle around the z-axis and elevation is the elevated angle away from the x-y plane.

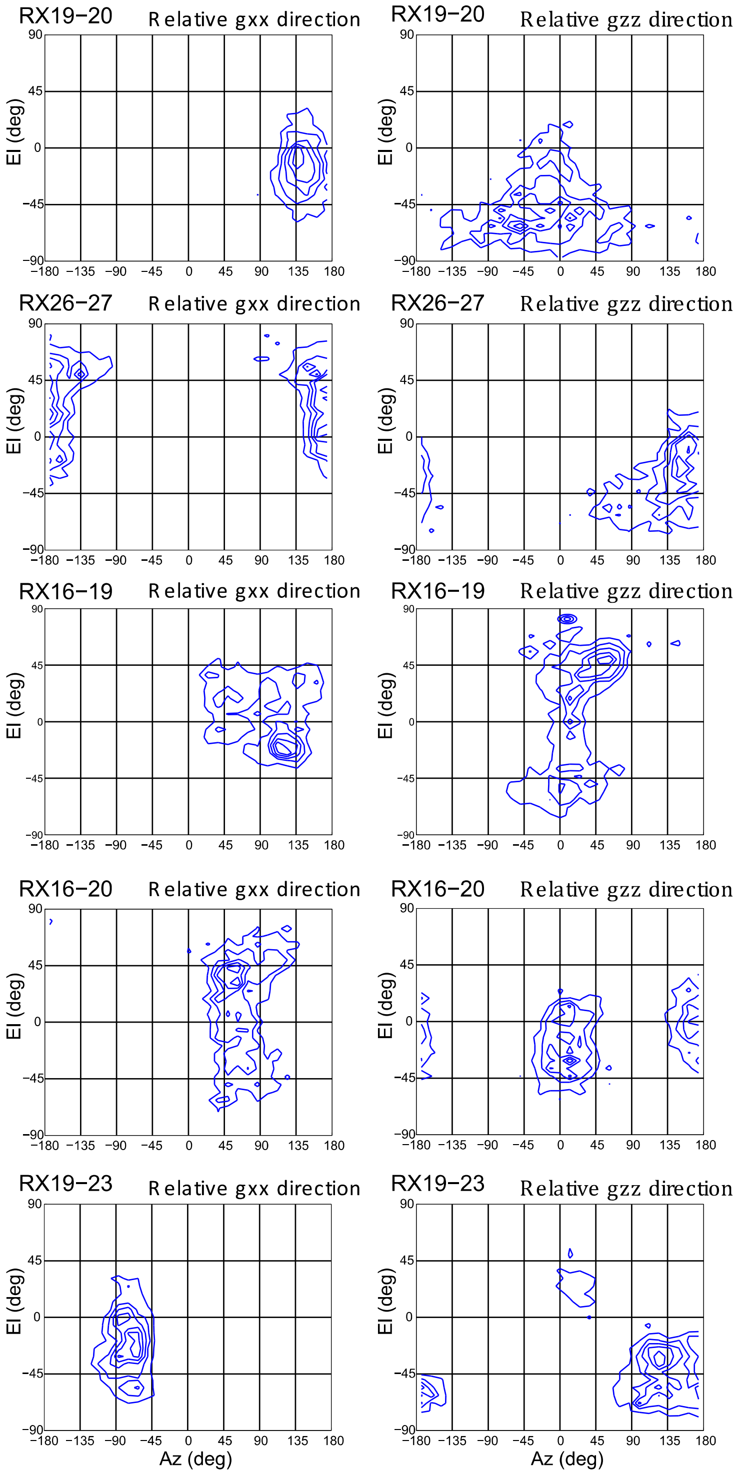
RX19−20
Relative gxx direction
RX19−20
Relative gzz direction
RX26−27
Relative gxx direction
RX26−27
Relative gzz direction
RX16−19
Relative gxx direction
RX16−19
Relative gzz direction
RX16−20
Relative gxx direction
RX16−20
Relative gzz direction
RX19−23
Relative gxx direction
RX19−23
Relative gzz direction
El (deg)
90
45
0
−45
−90
−180 −135 −90 −45 0 45 90 135 180
Az (deg)

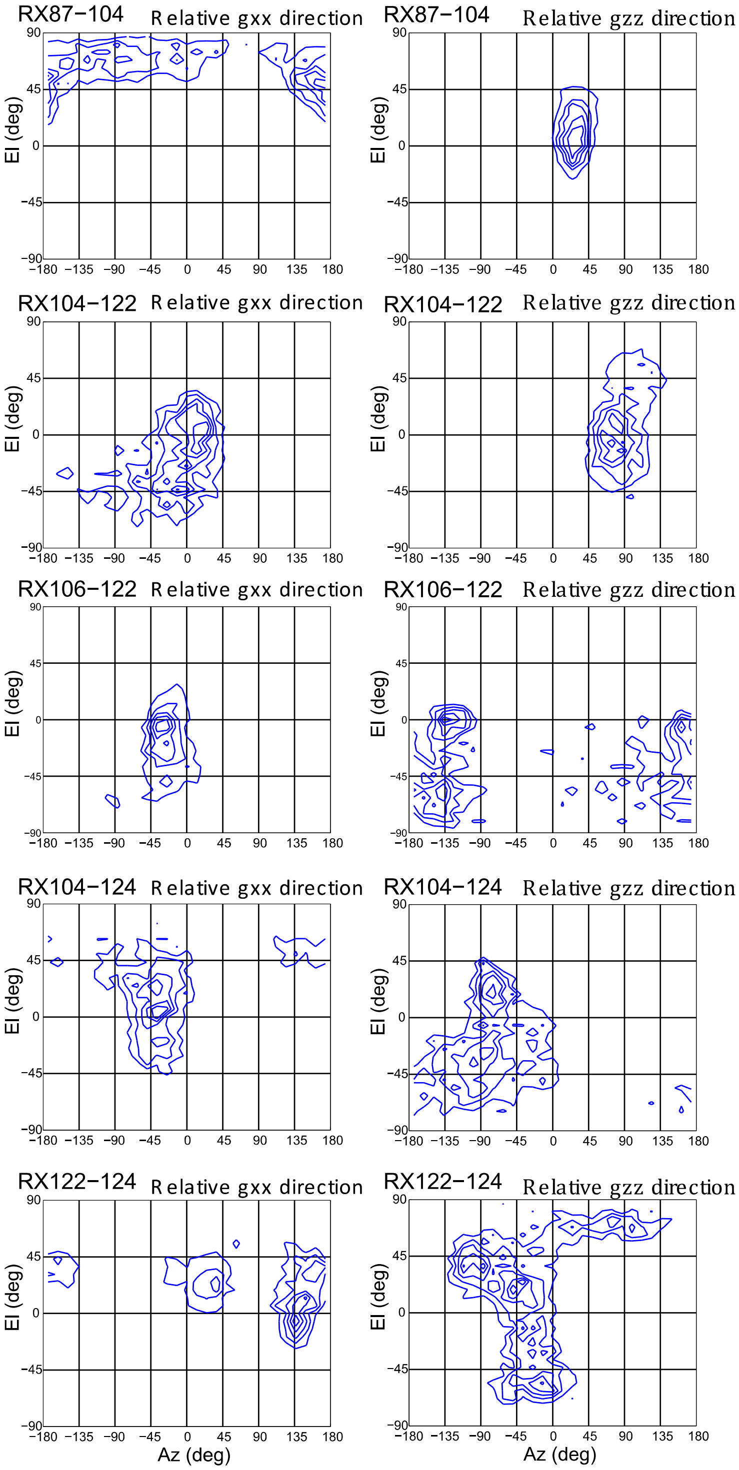

Figure 5.6.4 *Contour plots showing the relative rotation of the N-O vector of spin label pairs for different labelling sites, taken from molecular dynamics frames for all Rx constructs.*

From these plots it is again possible to see the bi-modal angular distribution of the α-helix i-i+3 and i-i+4 attachment sites, with i-i+1 sites being mono-modal. It is possible to see that the 19-20 i-i+1 attachment site has a narrower distribution in the gxx rotations compared to the 26-27 i-i+1 attachment site. The β-sheet attachment sites, agreeing with the tilt-roll-twist representation, are shown to be bi-modal in all but the diagonal sites. From this representation it is also possible to observe relative rotations of the perpendicular gzz axes, which reveal bi-modal angular distributions in the case of attachment sites 106-122 not apparent in the gxx rotations.

As part of this study was to develop an orientation selective PELDOR signal analysis the orientation PELDOR study was limited to the attachment sites which the molecular dynamics simulations suggested would have the most restricted and mono-modal angular distribution, the i-i+1 residue sites 19-20 and 26-27.

5.7. ORIENTATION PELDOR RESULTS OF RX RESIDUE I+1 HELIX SITES

Orientation PELDOR measurements were made using the W-band HiPER spectrometer described in Chapter 3 , using π pulse lengths between 7-10 ns depending on the optimal conditions for each sample. All measurements were made at 60 K were the sample was made by buffer exchanging the protein into a doubly concentrated D2O buffer followed by mixing in a 1:1 ratio with D8-glycerol, further details of the methods are given in Appendix.

High sensitivity is required to make orientation selective PELDOR measurements practical (typically six or more PELDOR experiments are required to derive accurate results). The most orientation selective positions for pump and observe are at the edges of the spectrum (gxx and gzz orientations) where the relative numbers of spins excited is very low. For gxx-gxx and gyy-gyy correlations it is also necessary to reduce the excitation bandwidth of both pump and observe pulses to get results that produce both useful angular information but do not result in overlap of pulses. Smaller excitation bandwidths can also have the added advantage of reducing instantaneous diffusion effects (especially in more concentrated samples), however this smaller bandwidth has to be compensated for by the use of a larger number of experiments.

Based on the analysis of the molecular dynamics simulations, as discussed in the previous chapter 5.6, the attachment sites chosen for the orientation selective PELDOR experiments were of the residue i and residue i+1 type. The prepared Rx spin labelled samples for this study had the spin label attached at residues 19-20 and 26-27 as shown in **Figure 5.7.1**. Measured PELDOR signals for residues 19-20 and 26-27 are shown in **Figure 5.7.2** and **Figure 5.7.3** and tables of the magnetic tensors and the magnetic fields used are shown in **Table 5.7.1** and **Table 5.7.2** respectively.

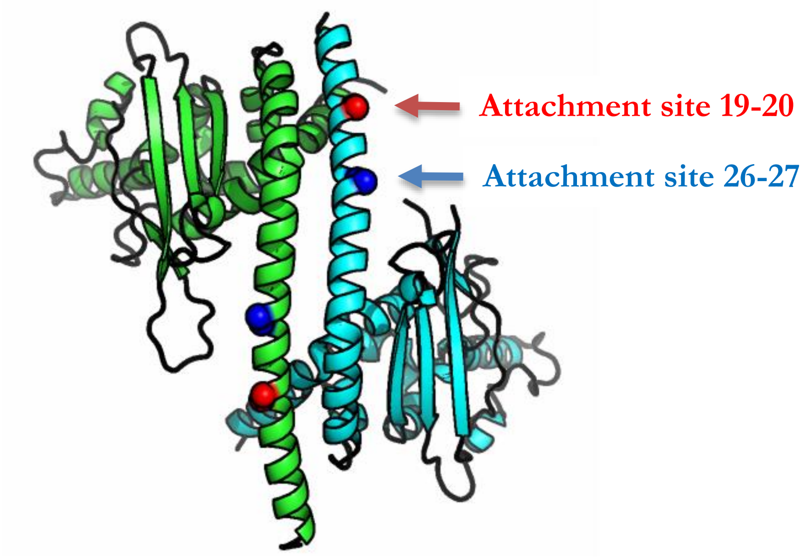

Figure 5.7.1 *Cartoon of the dimer protein Vps75 showing the two segments as green and light blue with the labelled residue sites selected for the orientation selective W-band PELDOR study indicated.*

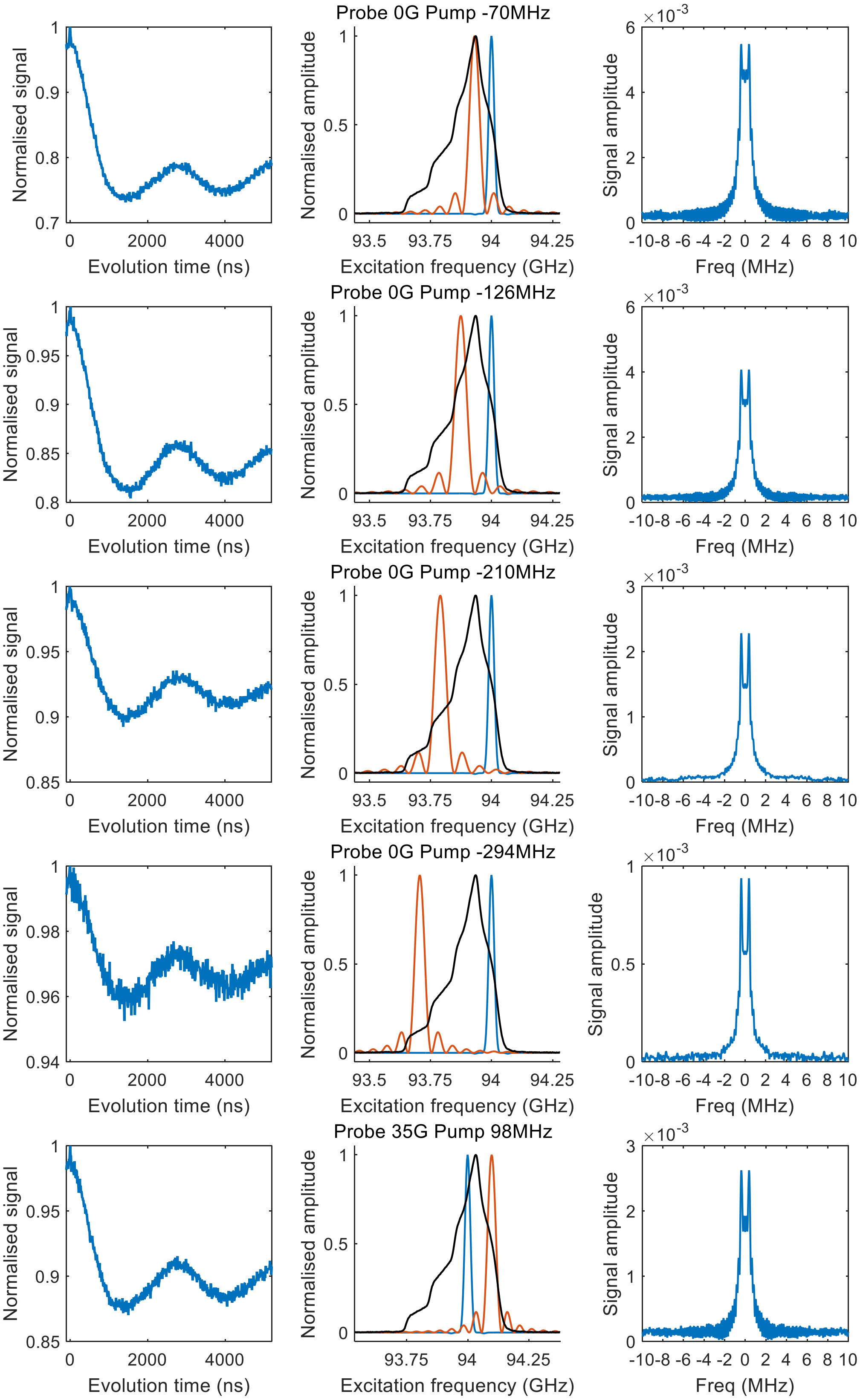
Probe 0G Pump -70MHz
Probe 0G Pump -126MHz
Probe 0G Pump -210MHz
Probe 0G Pump -294MHz
Probe 35G Pump 98MHz
Normalised signal
Evolution time (ns)
0
2000
4000
1
0.9
0.8
0.7
0.95
0.85
0.98
0.96
0.94
Normalised amplitude
Excitation frequency (GHz)
93.5
93.75
94
94.25
0
0.5
1
Signal amplitude
Freq (MHz)
×10^-3
-10 -8 -6 -4 -2 0 2 4 6 8 10
6
4
2
3
1
0.5

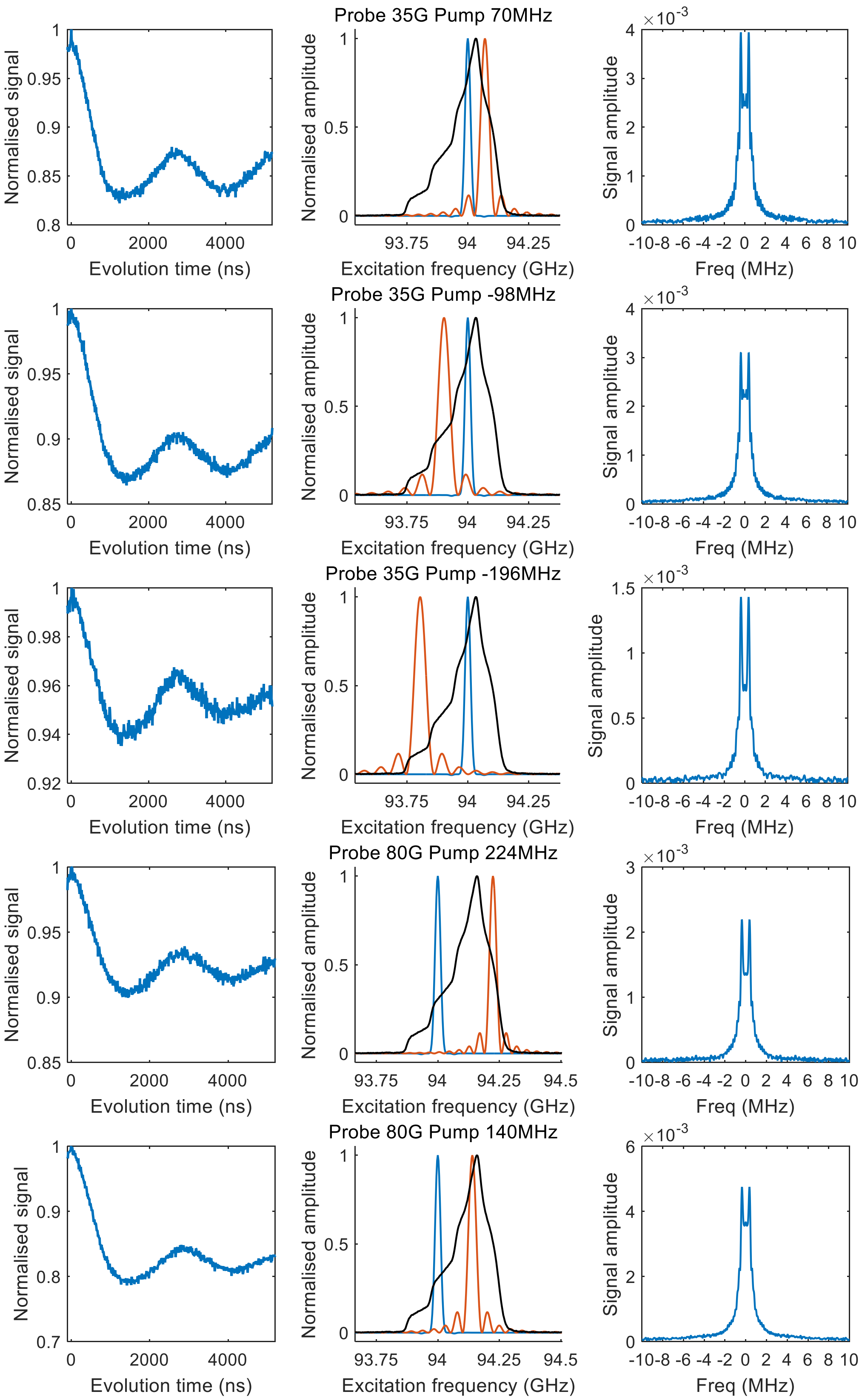
Probe 35G Pump 70MHz
Probe 35G Pump -98MHz
Probe 35G Pump -196MHz
Probe 80G Pump 224MHz
Probe 80G Pump 140MHz
Normalised signal
Evolution time (ns)
0
2000
4000
Normalised amplitude
Excitation frequency (GHz)
93.75
94
94.25
94.5
Signal amplitude
Freq (MHz)
-10 -8 -6 -4 -2 0 2 4 6 8 10
×10^-3

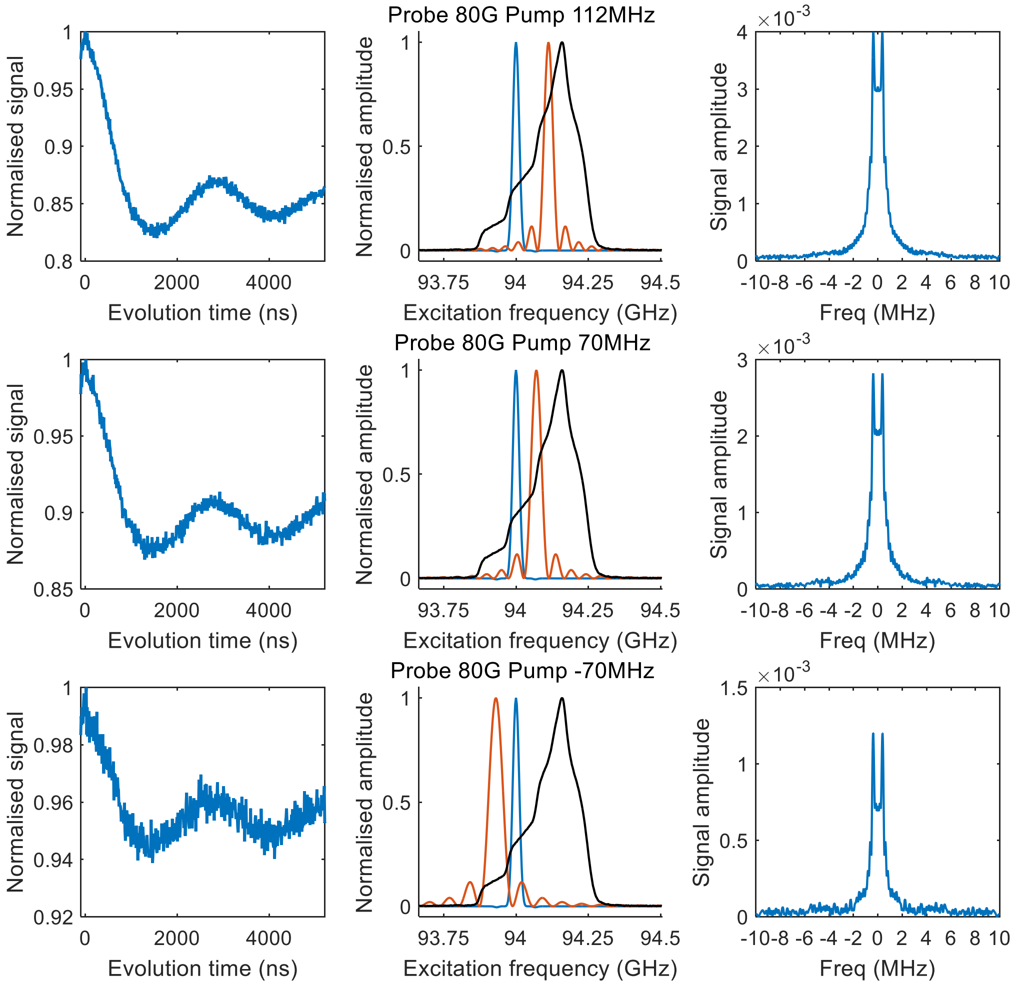

Figure 5.7.2 *Experimental PELDOR signal (left), pulse excitation overlaid on the Rx spin label spectrum (middle) and FFT of the PELDOR signal (right) are shown for each W-band orientation selective PELDOR experiment of sample RX19-20 shown in the same order as* ***Figure 5.7.5****.*

gxx	2.0091
gyy	2.0072
gzz	2.00341
Axx (MHz)	14.7
Ayy (MHz)	16
Azz (MHz)	97.8
Main coil field (Gauss)	33435

Table 5.7.1 *The values of the g-tensors and hyperfine coupling (MHz) for sample RX19-20 were found by fitting to pulsed W-band field-swept echo spectra obtained using selective*

pulses with the Pi pulse length being 100 ns to reduce excitation and thus instantaneous diffusion effects. The fitting was performed using the high performance EasySpin package.

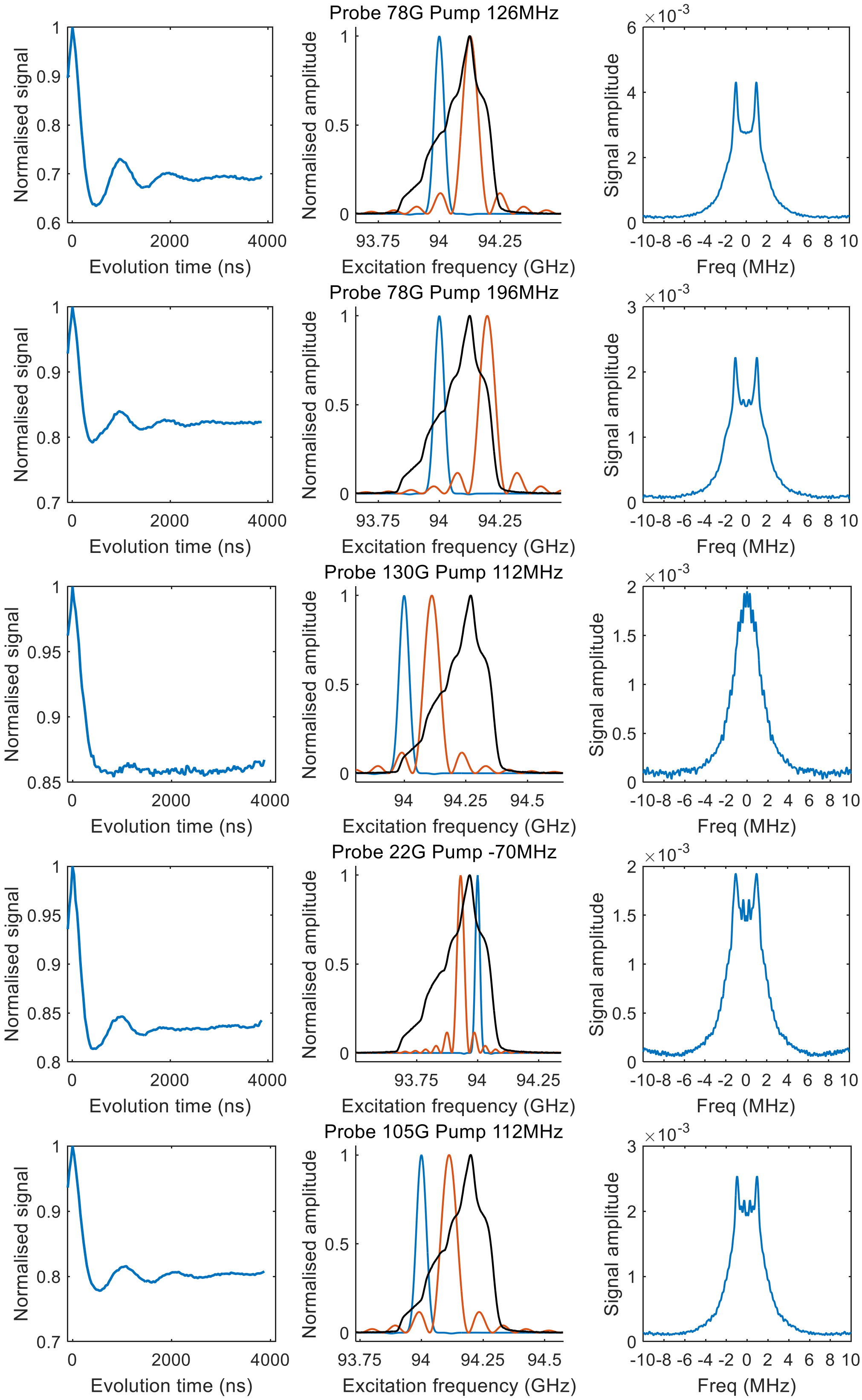

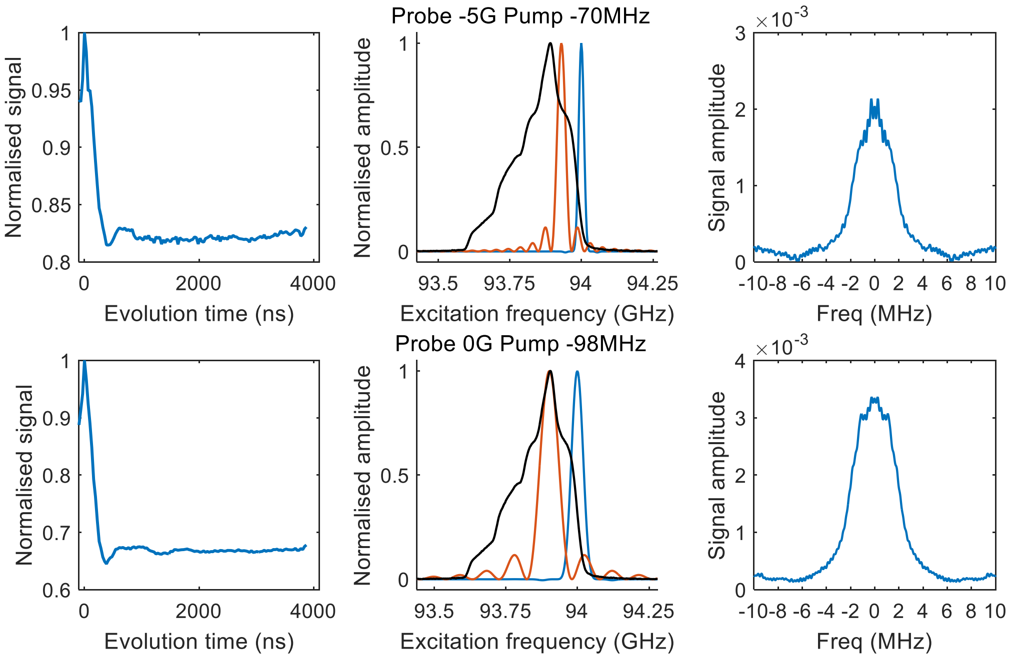

Figure 5.7.3 *Experimental PELDOR signal (left), pulse excitation overlaid on the Rx spin label spectrum (middle) and FFT of the PELDOR signal (right) are shown for each W-band orientation selective PELDOR experiment of sample RX26-27 shown in the same order as* ***Figure 5.7.5****.*

gxx	2.0091
gyy	2.0072
gzz	2.00341
Axx (MHz)	14.7
Ayy (MHz)	16
Azz (MHz)	97.8
Main coil field (Gauss)	33425

Table 5.7.2 *The values of the g-tensors and hyperfine coupling (MHz) for sample RX26-27 were found by fitting to pulsed W-band field-swept echo spectra obtained using selective pulses with the Pi pulse length being 100 ns to reduce excitation and thus instantaneous diffusion effects. The fitting was performed using the EasySpin simulation package.*

The analysis of the orientation selective PELDOR signals was two part. The first was the analysis of the signal modulation depths by way of a library fitting method, the second was the fitting of the background corrected PELDOR signal to a general model of two spin labels. The modulation depths, for the experimental conditions used, depend only on the relative rotation between the spin labels, and this can be used to derive the three Euler angles described earlier independently of the two relative position angles and the separation distance. This simplifies the problem and the rotation angles found from the modulation depth analysis can be used as initial values for the fitting algorithm.

A library of PELDOR modulation depths was simulated for a uniformly distributed array of rigid spin-spin orientations. The modulation depth of a PELDOR signal is the value around which the dipolar modulation is oscillating. As long as the observer pulse is suitably selective, such that it can be assumed to excite on average only one spin, the modulation depth should depend only on the correlated excitation of pairs of spins, which can be expressed as a three dimensional rotation angle set. In this work the ZYZ Euler convention is used as previously described. A root mean square deviation (RMSD) comparison between the libraries and the experimental measurement was first conducted to gain an insight into the relative angles between the spin label pairs. This has been plotted for the gxx vector rotations in **Figure 5.7.4** for both of the Rx spin labelled samples. Overlaid on these plots are the gxx molecular dynamics simulation results. Due to experimental symmetries there are 16 possible relative angle solutions and the lowest RMSD values for each of these relative angles is shown in **Table 5.7.3**.

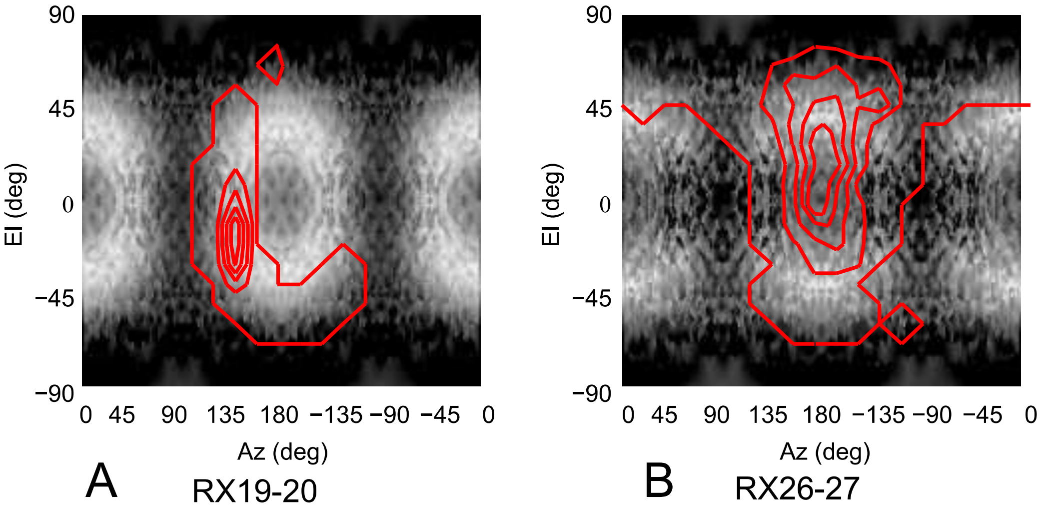

Figure 5.7.4 *Two-dimensional greyscale plots showing the RMSD values between a library of simulated relative spin label orientations and the experiment measured modulation depth values. The scale is normalized such that white corresponds to the smallest RMSD value and black corresponds to the largest. Overlaid is a red contour plot of the density of relative orientations derived from the MD simulations. (A) Rx19-20 result (B) Rx26-27.*

Alpha (Z)	Beta (Y)	Gamma (Z)
135.0	41.0	-135.0
48.8	130.0	-138.8
-41.2	50.0	-131.2
-135.0	139.0	-135.0
135.0	139.0	-45.0
48.8	50.0	-41.2
-45.0	139.0	-45.0
-135.2	41.3	-45.3
135.2	41.3	45.3
45.3	139.2	45.3
-45.3	41.3	45.3
-135.2	139.2	45.3
135.2	139.2	135.2
45.3	41.3	135.2
-45.3	139.2	135.2
-135.2	41.3	135.2

Alpha (Z)	Beta (Y)	Gamma (Z)
-146.3	129.0	-146.3
33.7	129.0	-146.3
-33.7	51.0	-146.3
146.3	51.0	-146.3
-146.3	51.0	-33.7
-33.7	129.0	-33.7
33.7	51.0	-33.7
146.3	129.0	-33.7
-146.3	129.0	33.7
-33.7	51.0	33.7
33.7	129.0	33.7
146.3	51.0	33.7
-146.3	51.0	146.3
-33.7	129.0	146.3
33.7	51.0	146.3
146.3	129.0	146.3

Table 5.7.3 *All the angles corresponding to the RMSD minimum found in the analysis of the RMSD values between a library of simulated relative spin label orientations and the*

experiment measured modulation depth values. 16 Solutions are found which is consistent with experiment symmetry.

The molecular dynamics are in agreement with the residue 19-20 results with the density peak of spin label rotation lying over an RMSD minimum in the modulation depth results. There is a difference between the density peak of the spin rotation and the RMSD minimum in the modulation depth for the residue 26-27.

Using these modulation depth derived rotation angles as initial search points the PELDOR signals were fitted to the previously described model of two spin labels, this will be the second part of the PELDOR signal analysis. By using a global minimization fitting routine a best fit value of the relative angles between the spin labels and a distribution around these angles was found. The distance distribution was included into the model as a Gaussian distribution where the initial mean and width values were chosen from the Tikhonov regularized distance solution to the weighted average of the experimental W-band PELDOR signals [106]. The fitting model distance distribution width and mean value was allowed to vary from the initial values within a range of initial value +-10Å. The fitting model rotation angle values were allowed to vary within the full range of valid rotation angles for the Euler ZYZ angle convention. The algorithm used performs an iterated simulation and fitting to the experimental trace values, generating penalty values (RMSD) that were then fed back into the refinement. The global minimization used a genetic algorithm, with a population size of between 100 and 200 steps, to reduce the chance of settling in local minima. The algorithm was run independently for each of the 16 symmetric starting points as initial values to ensure that a common minimum was found. The rotation angle solution found by the fitting algorithm with the closest agreement to the x-ray crystallography model are shown in **Table 5.7.4**. These selected angles when used as structural constraints in the XPLOR-NIH structure determination package were found to give the energy minimum for docking of the dimer, discussed in a later chapter 5.8.

	Alpha (Z)	**Beta (Y)**	**Gamma (Z)**
RX19-20	135.0 (8.6)	139.0 (42.8)	135.0 (8.0)
RX26-27	33.7(13.5)	129.0(40.4)	33.7(1.1)

Table 5.7.4 *Euler angles, mean values, derived from the fitting analysis results. Numbers in brackets are the standard deviations of a normal distribution around the mean values.*

To assess the fitted model the measured PELDOR signals are plotted with the PELDOR signals simulated using the molecular dynamics simulation model, a random orientation PELDOR signal with the distance derived from the Tikhonov fit and the PELDOR signals from the fitted model. These PELDOR signal comparisons are shown in **Figure 5.7.5**. Spherical density plot of relative spin-spin N-O vector directions for the fitted distribution is shown in **Figure 5.7.6** along with the equivalent distribution obtained from the MD frames. It is noted that the contours are equally spaced normalized to the maximum of the distribution. For both attachment sites there is a reasonable overlap between the contours derived from the MD frames and the contours derived from the fitting routine.

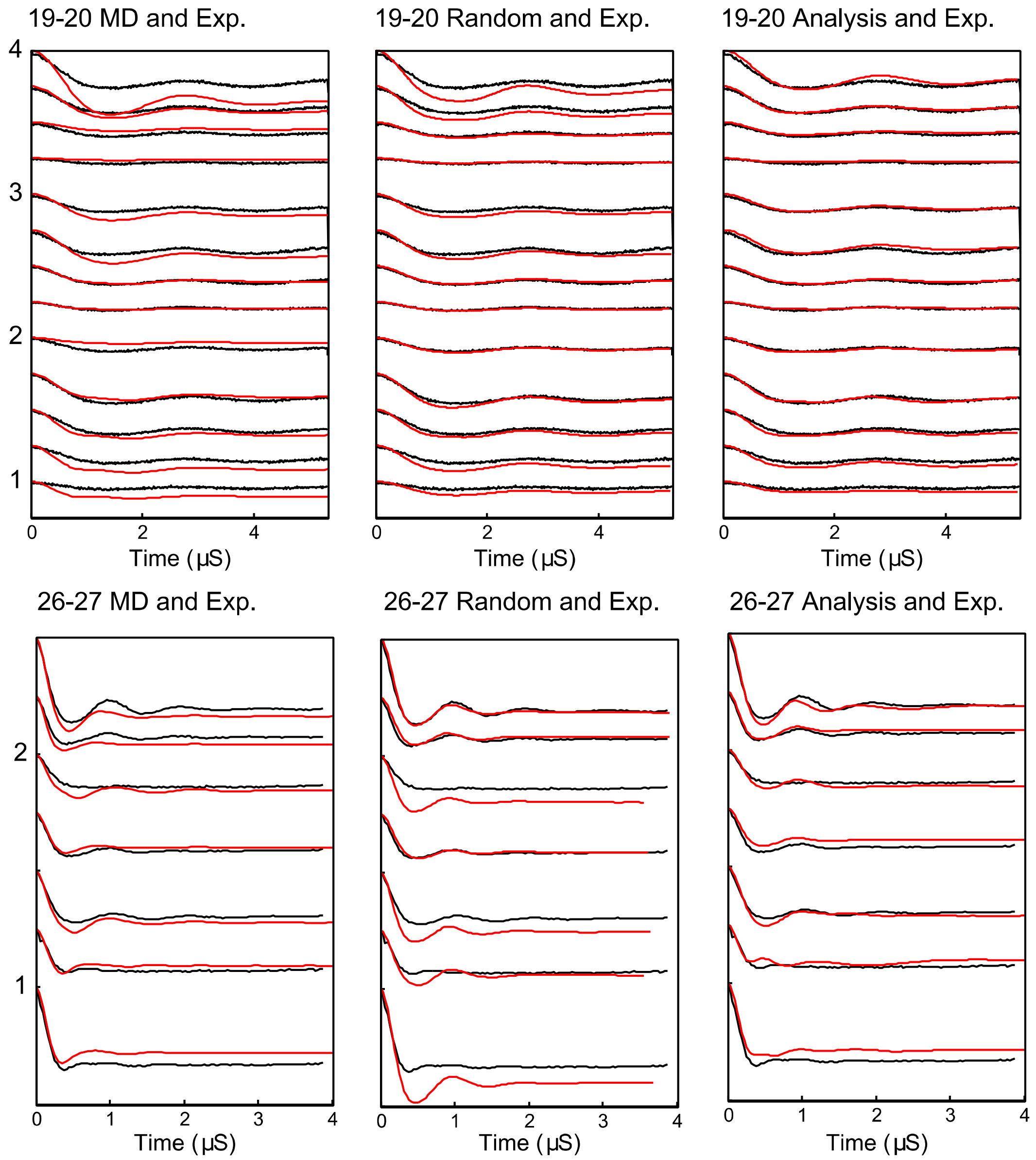

Figure 5.7.5 *Simulated PELDOR signals for Rx26-27 and Rx19-20 are shown in red for the cases of left: simulated PELDOR signals for the MD predicted relative label distribution centre: simulated PELDOR signals for a uniform distribution with no defined relative label orientation and right: the PELDOR signal result of the fitting analysis. The experimental PELDOR signal is shown in black. Excitation profiles and FFT of traces for each experiment is shown in* ***Figure 5.7.2*** *and* ***Figure 5.7.3****.*

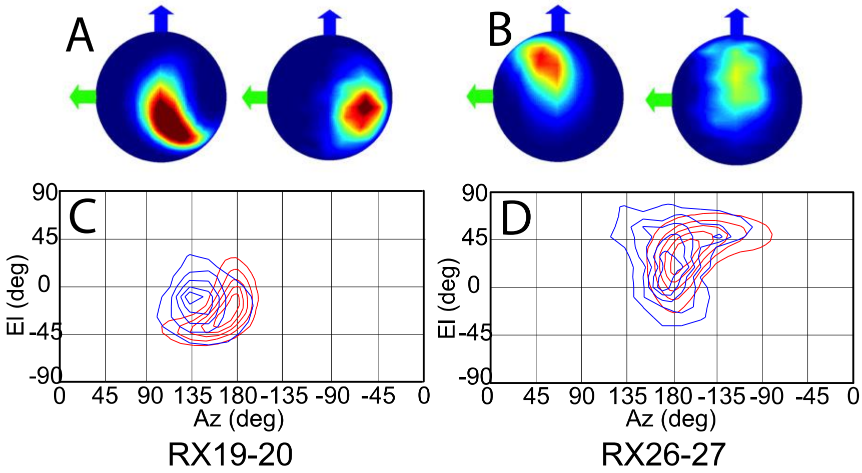

Figure 5.7.6 The result derived from the fitting analysis and the MD are shown as spherical plots where the colour-scale shows the density of relative NO bond directions for (A) Rx19-20 and (B) Rx26-27, for each pair the left image represents the fitting analysis results and the MD results on right. Blue and green arrows indicate the gyy and gxx axes respectively. The same data is presented as 2D contour plots with the fitting analysis is shown in red and the MD results in blue for (C) Rx19-20 on the left and (D) Rx26-27.

The resulting PELDOR signal fits show good agreement with the experimental measured PELDOR signal. For Rx19-20 the MD does not predict the larger spread in the orientations that is experimentally observed. It is noted that the simulated PELDOR signals from the MD fit has a worse fit to the experimental data than the random orientation case. It can be seen in **Figure 5.7.6** that the distribution of the relative NO vector angles is smaller for the MD simulations compared to the fitting result. It is also noted from **Figure 5.7.6** that the MD distribution predicted for Rx19-20 is smaller than that predicted for the Rx26-27 case. For Rx26-27 the simulation of the MD derived PELDOR signal has, by contrast, a better fit to the experiment PELDOR signal than the random orientation, and the distribution of NO vector angles shown in **Figure 5.7.6** shows similarity between the MD and fitted results. In all cases the fitting results give the best fit to the experimental signal.

5.8. USING ORIENTATION PELDOR RESULTS AS CONSTRAINTS IN XPLOR-NIH

Although no method presently exists to directly refine a structure within molecular dynamics structure refinement packages, using the measured orientations as restraints. It was possible to use the XANG restraint within XPLOR-NIH to refine the positions of each nitroxide spin-pair. As the protein in is a dimer in this case the problem is posed as a docking problem, where the relative angle solutions found from the orientation PELDOR are used to dock unit A of the dimer to unit B. A set of polar angle restraints were calculated for each of the spin-pairs and the relative orientations could be refined for individual pairs. Combined refinement of both i-i+1 spin-pairs was only possible by extrapolation of spin-orientation within each monomer using standard helical geometries. The angles calculated for refinement using the XANG restraint within XPLOR-NIH are given in **Table 5.8.1** and an overlay cartoon view of the docked molecule against the crystallography structure is shown in **Figure 5.8.1**. The rigid body docking was conducted applying constraints to the two chains in the dimer, with their backbone molecules harmonically restrained and sidechain atoms allowed to freely move under the applies constraints.

	Az deg	**El deg**
19-20 label on unit A of dimer structure	0	0
26-27 label on unit A of dimer structure	-10.41	6.6
19-20 label on unit B of dimer structure	172.04	-27.64
26-27 label on unit B of dimer structure	-178.61	33.86

Table 5.8.1 *Angles derived from the orientation selective PELDOR results, selected with the aid of the molecular dynamics results. These angles were implemented using the XANG restraint in XPLOR-NIH.*

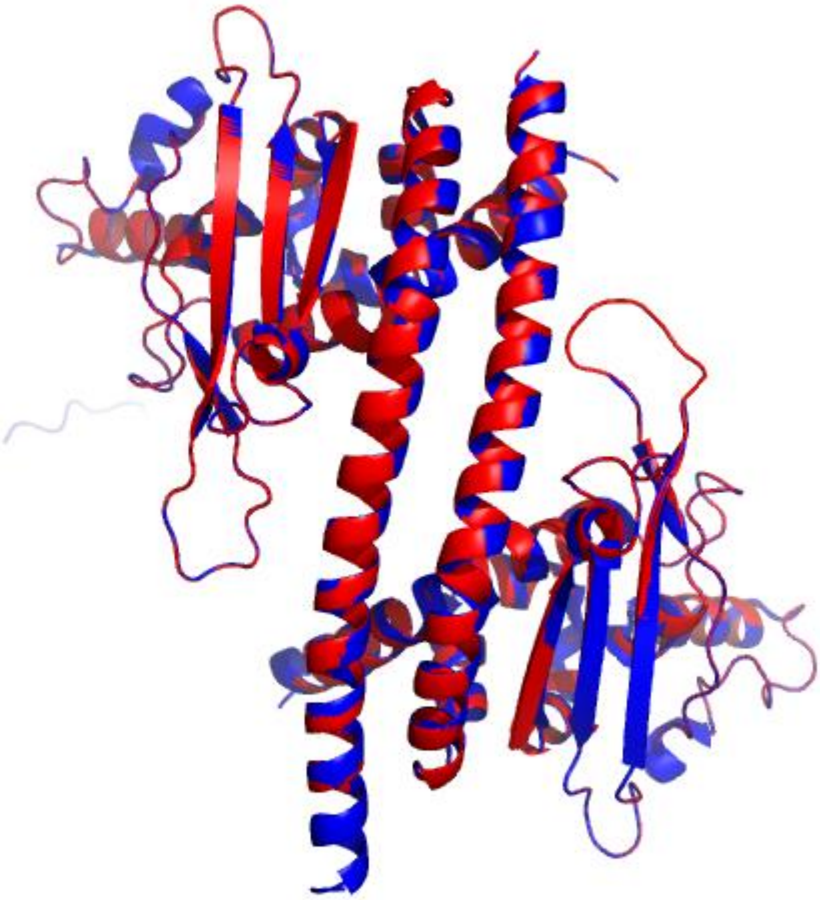

Figure 5.8.1 *Structure of the docked molecule of the dimer Vps75 shown (Red) over the crystallography structure (PDB 2ZD7) (Blue). The docking was a rigid body docking and the backbone of each chain was kept rigid. The minimization included the angles and distances obtained by the orientation PELDOR study.*

As discussed earlier the orientations, which can be extracted from the PELDOR signal analysis are subject to experimental symmetries and so robust methods of incorporating such restraints into molecular refinement must still be developed. The force-field described as XANG in XPLOR-NIH is able to partially utilize such restraints by considering only the relative angles of the nitrogen-oxygen bond direction of the spin label, as shown. Trials of the different angle solutions have to be made to such that the minimum energy solution is found using the structure minimisation. In the case of this work the choice of angles were based on the closest solutions to the minimum energy solution of the molecular dynamics with all of the angles references to one principal spin label attached to sites 19-20 of unit A in the dimer.

One possible method of integrating the PELDOR signal as restraints into a structure refinement package for rigid body docking problems such as this is to integrate a PELDOR signal simulation into the step penalty calculation of the minimizer. For each step in a molecular dynamic minimisation the PELDOR signal is calculated, by use of a precomputed library, and the RMSD between the simulated signal and experimentally measured signal is in addition to the penalty from the force fields and other restraints. It is hoped that an investigation into this will form part of a future project.

5.9. CONCLUSIONS

In this work an exploration of the applicability of the bi-pedal spin label Rx for orientation selective PELDOR studies was made. This involved the analysis of molecular dynamics simulations, obtaining simulated relative rotations which are directly comparable to those which are obtained by orientation selective PELDOR signal analysis. The relative rotation results of the molecular dynamics simulations are presented for several attachment sites which were produced and used to select the most promising attachment sites for orientation selective PELDOR studies. A general model for two spin labels was presented which could be used with PELDOR signal simulation code to fit the model parameters for a given set of experimentally obtained PELDOR signals. Results for fits of this model to two cases of spin labelled dimeric protein Vps75, with different attachment sites are given and compared to the PELDOR signals associated with the molecular dynamics simulation of each case and the special case of no defined relative orientation between the spin labels, the so called random orientation case. The results show good agreement between the fitted model solution and the molecular dynamics solution. An attempt was made at using the fitted model angles in a structure determination package XPLOR-NIH and a brief discussion on potential implementation of orientation PELDOR signals as a restraint in structure determination packages is given.

Chapter 6 HIGH FIELD STUDIES OF MEMBRANE PROTEIN MSCS WITH MULTIPLE SPIN LABELS.

Studies have estimated that around 60% of the proteins in every genome are homo-oligomers [107] and the majority of structures in the Protein Data Bank (PDB) [108] are oligomers. Due to the size of these proteins and the desire to characterise those proteins in a membrane environment there is great difficulty in deriving molecular structures by either X-ray crystallography or nuclear magnetic resonance (NMR) which are well establish tools for solving protein structure. It is therefore of great importance to develop tools capable of characterising such systems that do not rely upon having to produce protein crystals, and that are relatively insensitive to the overall size of the protein. The PELDOR experiment previously described, chapter 2.4, is identified as one such tool due to the relatively long range 2-10 nm distance measurements which can be made using this experiment. The ability to introduce a limited number of spin labels in a site specific way can also simplify problems in otherwise large and complicated molecules. Despite the advantages and an increased interest in utilising PELDOR for solving oligomeric proteins there is still no clear experiment protocol and there has been evidence of experimental artefacts being introduced to the measured signal which have unobvious origins [64].

Chapter 6 High field studies of membrane protein MscS with multiple spin labels.

This chapter will present an investigation into PELDOR experiments of homo-oligomer proteins using the W-band HiPER spectrometer. A feasibility study was undertaken to investigate the measurement of relative orientation angles and distances between spin labels introduced to the mechanosensitive channel protein MscS, and a measurement program was conducted to make these measurements. Due to a series of anomalous measurement results that suggested that the signals measured could not be described by the commonly used simplified PELDOR signal expression for multiple dipole coupled spins, an investigation into the influence of the protein environment on the measured PELDOR signal was made.

6.1. THEORY

The general orientation selective PELDOR analysis is considerably more complex in a large multi-spin system and is only tractable, if there is strong symmetry in the system. By considering an isolated system of N spins, where any spin can take the role of either a pumped spin or an observer spin, (or not be excited) we can express the PELDOR signal V(t) at time t analytically as:

$$V(t) = \frac{V(0)}{N} \sum_{obs=1}^{N} \prod_{\substack{pump=1 \\ obs \neq pump}}^{N} 1 - \lambda_{pump}^{obs} \left[1 - \cos\left(\omega_{dd}{}_{pump}^{obs} t \right) \right]$$

Equation 6.1.1

where

$$\omega_{dd}{}^{obs}_{pump} = \frac{\mu_0}{4\pi\hbar}\frac{g_{obs}g_{pump}\mu_B}{r_{obs\leftrightarrow pump}{}^3}\left[1 - 3\cos^2\left(\theta^{obs}_{pump}\right)\right]$$

Equation 6.1.2

and $V(0)$ is the signal at zero time, λ^{obs}_{pump} is the fraction of observer spins, excited by the observer (probe) pulses, that have a partner spin that is separately excited by the pump pulse, $r_{obs\leftrightarrow pump}$ is the spatial separation between the observer and pump spins and θ^{obs}_{pump} is the angle between the dipolar vector and the magnetic field.

This signal will be a powder average such that the dipolar vector can take any relative angular position with respect to the magnetic field. The analysis is best considered by specifying suitable frames of reference and rotations for each spin and the whole cluster of spins relative to the laboratory frame defined by the axis of the magnetic field. To calculate λ^{obs}_{pump} and θ^{obs}_{pump} for each spin, in a given experiment, it is also necessary to consider the exact excitation profile of each pulse, the symmetry of the system of spins and the effects of all the anisotropies of the spin system. The profile of the pulse is calculated from first principles as described in Chapter 4 , and from a system calibration as described in Chapter 3 , although it is worth reminding the reader that the measurement spectrometer has a relatively flat frequency response.

When considering the PELDOR signal for more than two interacting spins, unlike the two spin case, there will be coupling contributions associated with all the different spin interactions. This complicates the analysis as it is no longer possible to solve for distances directly as can be done in a two spin system. This can be clearly seen by expanding the signal expression for the relatively simple case of a symmetrical trimer.

$$\begin{aligned}V(t) = 1 &- \frac{2\lambda_1^2}{3} + \frac{2}{3}\mathrm{Cos}[t\omega\mathrm{dd}_1^2]\lambda_1^2 - \frac{2\lambda_1^3}{3} + \frac{2}{3}\mathrm{Cos}[t\omega\mathrm{dd}_1^3]\lambda_1^3 + \frac{1}{3}\lambda_1^2\lambda_1^3 \\ &- \frac{1}{3}\mathrm{Cos}[t\omega\mathrm{dd}_1^2]\lambda_1^2\lambda_1^3 - \frac{1}{3}\mathrm{Cos}[t\omega\mathrm{dd}_1^3]\lambda_1^2\lambda_1^3 + \frac{1}{6}\mathrm{Cos}[t\omega\mathrm{dd}_1^2 \\ &- t\omega\mathrm{dd}_1^3]\lambda_1^2\lambda_1^3 + \frac{1}{6}\mathrm{Cos}[t\omega\mathrm{dd}_1^2 + t\omega\mathrm{dd}_1^3]\lambda_1^2\lambda_1^3 - \frac{2\lambda_2^3}{3} \\ &+ \frac{2}{3}\mathrm{Cos}[t\omega\mathrm{dd}_2^3]\lambda_2^3 + \frac{1}{3}\lambda_1^2\lambda_2^3 - \frac{1}{3}\mathrm{Cos}[t\omega\mathrm{dd}_1^2]\lambda_1^2\lambda_2^3 \\ &- \frac{1}{3}\mathrm{Cos}[t\omega\mathrm{dd}_2^3]\lambda_1^2\lambda_2^3 + \frac{1}{6}\mathrm{Cos}[t\omega\mathrm{dd}_1^2 - t\omega\mathrm{dd}_2^3]\lambda_1^2\lambda_2^3 + \frac{1}{6}\mathrm{Cos}[t\omega\mathrm{dd}_1^2 \\ &+ t\omega\mathrm{dd}_2^3]\lambda_1^2\lambda_2^3 + \frac{1}{3}\lambda_1^3\lambda_2^3 - \frac{1}{3}\mathrm{Cos}[t\omega\mathrm{dd}_1^3]\lambda_1^3\lambda_2^3 - \frac{1}{3}\mathrm{Cos}[t\omega\mathrm{dd}_2^3]\lambda_1^3\lambda_2^3 \\ &+ \frac{1}{6}\mathrm{Cos}[t\omega\mathrm{dd}_1^3 - t\omega\mathrm{dd}_2^3]\lambda_1^3\lambda_2^3 + \frac{1}{6}\mathrm{Cos}[t\omega\mathrm{dd}_1^3 + t\omega\mathrm{dd}_2^3]\lambda_1^3\lambda_2^3\end{aligned}$$

Equation 6.1.3

The later terms also now include sum and difference dipolar frequencies, which can appear as spurious distances or broadening if analysis methods only designed for two spins are applied. The detailed expression for a heptameric system contains considerably more terms. Experimentally, the higher order terms can be made small, reducing λ_{pump}^{obs}, by selectively exciting small fractions of spins, but only at the cost of signal to noise. To a certain extent, a reduction in λ_{pump}^{obs} happens automatically in an orientational PELDOR experiment at high fields as both the pump and observer pulse are necessarily more bandwidth selective to be more angularly selective, and there is a technical requirement that pulses should not overlap. The effects of the higher order terms can also be reduced, using the standard PELDOR analysis, by first power scaling the form factor according to the number of spins [63]. This has been shown to work well for systems up to 5 spins, but becomes less useful for larger spin systems. In the analysis presented here the full expression for seven spins is used in the modelling.

6.2. MODELLING HOMO-OLIGOMERIC PROTEIN SYSTEMS WITH CYCLIC SYMMETRY FOR ORIENTATION SELECTIVE PELDOR EXPERIMENTS

In this chapter a principle for modelling homo-oligomeric spin labelled protein systems is presented. It is applicable generally for homo-oligomeric protein systems with cyclic symmetry but here we will focus on the case of the heptameric homo-oligomer mechanosensitive channel protein of small conductance (MscS) that has C7 cyclic symmetry. In these systems, in principle, if a spin label is attached to one monomer unit of this protein then all 7 units will have a spin label, subject to labelling efficiency. A figure of the x-ray crystallography resolved structure for the open form of MscS (PDB 2VV5) is shown in **Figure 6.2.1**.

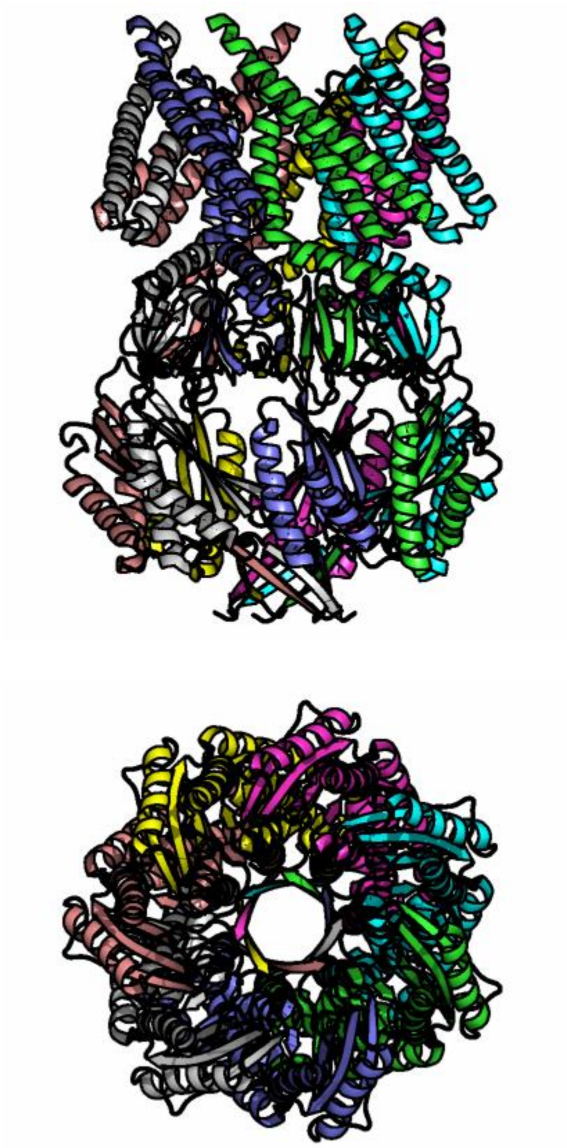

Figure 6.2.1 *Crystal structure of membrane protein mechanosensitive channel of small conductance (MscS) PDB 2VV5.*

It is expected that each of the units in the homo-oligomer will behave in the same mechanical and structural way. A consequence of this will be that if a spin label is attached to one unit and has a particular set of conformers related to the local environment of the label, then this will be the same set of conformers for all of the other units. If we were now attempting to find the relative orientation of the spin labels this will greatly simplify the problem, as we are only solving for one conformation set. It is also the case that if we have a number of spin labels attached to the cyclically symmetric molecule then we can instead of solving for each of the distances between the spin labels as shown in **Figure 6.2.2** we can solve for only the radius distance which connects all the spin labels to the centre of the oligomer.

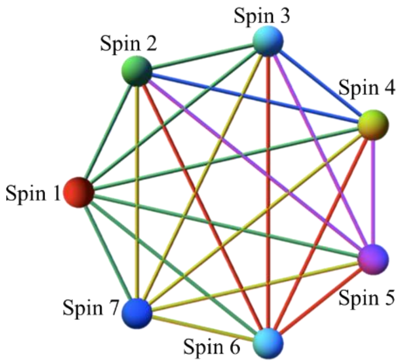

Figure 6.2.2 *Illustration of the inter spin label distances of a heptamer structure.*

We now have a model for the homo-oligomer which has the variables of; number of spins, radius of polygon and conformation set of a single unit. To model the spin label conformation there have been several elaborate approaches previously suggested, however to minimise complexity in this fit a 'vector and angle' approach has been used. A description of the model is as follows. First the number of units in the cyclically symmetric oligomer is chosen by the user or by the minimisation algorithm, in this example of MscS it is relevant to choose a heptamer which has 7 units. Next a distribution of radii are chosen, and in the simulation code this has been a normal distribution such that it is defined by a mean and width value. To define the angular distribution an angle in spherical coordinates is chosen, this is the centre of the angle distribution, and an angle of rotation around this central vector is also chosen. Along with this central vector direction a solid angle is defined the width of this distribution and an angular value is chosen that defines the rotation angle distribution. The rotation angle distribution is a uniform distribution with a range around the central value. A diagram showing the model parametrisation is shown in **Figure 6.2.3**, where r is the mean of the radial distribution Δr is the width of the distribution, (θ,φ) are the spherical coordinates for the centre of the cone distribution to which the x-axis is rotated and Ω is the solid angle of this cone and α is the rotation around the cone vector, effectively rotating the z and y axis around the new position of the x axis. The initial frame which the unit conformation set is defined has the x axis point radially outwards from the centre of the polytope is shown as a red arrow in the figure, the z axis points perpendicular out of the plane of the polytope shown as green a green arrow in the figure and the y axis is constrained accordingly pointing perpendicular shown as a blue arrow. The axes here represent the principal axes of the spin label for both the g-tensor anisotropy and the hyperfine anisotropy, such that for a nitroxide spin label the Nitrogen-Oxygen vector points along the x axis and the z axis is perpendicular to the plane of the nitroxide ring.

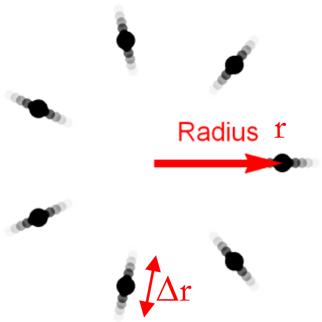

1) Define the radius distribution to

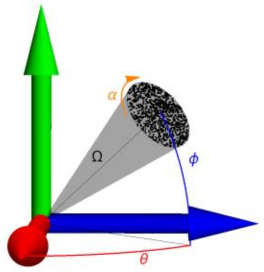

2) Define the angular conformations in the frame of one of the oligomer units and then give this spin label conformation set to all spin centre points.

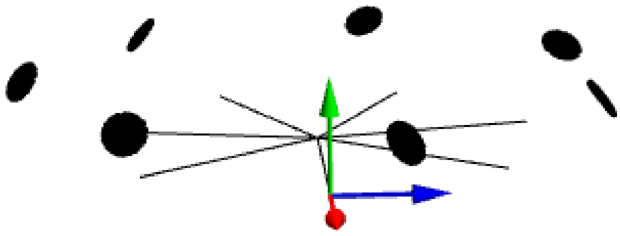

Figure 6.2.3 *Model used for cyclic symmetric oligomer spin labelled structures, parameterised with the radius of the polygon, the centre and distribution width of a cone and a rotation angle around the vector with a distribution.*

This model can now be used to calculate the associated PELDOR signal as we can easily calculate a set of rotation matrices which relate the three dimensional rotation angles of each spin to each other and calculate the inter-spin distances for each spin. Using the PELDOR simulations we can also fit a model to experimental PELDOR measurements using a global minimisation algorithm. However there are several assumptions to this model, and it has to be considered if it will be valid under the relevant experimental conditions. First each monomer unit must behave in an identical way such that we can treat the model as being one conformer with cyclic symmetry. It also assumes that the radially distribution of the monomers relative to the centre is a mono-distribution. Finally it assumes that the orientation distribution can be approximately described as a cone surface distribution and again a mono-distribution. In the case of the spin labelled mechanosensitive protein MscS, the biomolecule of interest in this work, the model assumptions were expected to be small perturbations on the expected results based on evidence from CW EPR indicating that at certain labelling sites the spin label mobility is strongly restricted and spin label conformation predictions based on past X-Ray crystallography results which indicated small distributions of the spin at these sites. These results will be presented and discussed in detail in a later sub chapter.

Several test cases were simulated using a simulator written with the MATLAB 2014b package to observe differences in the PELDOR signals for different geometries of a heptamer. The first case is the rigid single conformer pointing radially relative to the centre of the heptamer. It is observed that the modulation depth has a strong dependence the orientation of the spin label in the model, and also the pulse excitation selections. This indicates that the signal has a dependence on the orientation of the spin label and, at least in the very rigid case, suggests that this could be experimentally observed.

The experimental parameters were chosen to be reasonably spread across the nitroxide spectrum particularly targeting the principal axes of gxx, gyy and gzz based on analysis of the excitation profiles of the pulses.

6.3. ANALYSIS ALGORITHMS FOR CYCLICALLY SYMMETRIC MULTIPLE SPIN SYSTEMS

Several attempts were made at reducing the time required to analyse the orientation selective multi spin PELDOR signals. The time is long because of the long times required to directly fit experimental data to the described model using a general global minimisation routine. Several signal analysis techniques have been described for other spectrographic methods with principal component analysis being a routinely used mathematical tool [109-111]. The underlying idea of principle component analysis is to transform observations made with a large number of variables, and these variables can have a large amount of correlation, into a new set of variables which are uncorrelated. This has a huge applicability to data reduction where a large library of observations can be reduced to just a few observations where the principal component variables have large variation. Observations which don't have large variation in the principal components can be said to contain very little information compared to the other observations and are disregarded. This process was utilised in this case where a large library of precomputed PELDOR signals were generated using an optimized algorithm and then this library was reduced down to only some 10's of PELDOR signals which were generated by principal component analysis. Similar methods using other data reduction techniques have been previously reported for PELDOR signals at X-band [17]. The algorithm will now be described and examples given, although as will be discussed in more detail later, various experimental challenges meant the algorithm could not be used for processing experimental PELDOR signals.

For a given radius r a library of PELDOR signals is generated for each unique angular position of the spin label (in 5 degree steps) for each angular correlation, assuming C7 symmetry, and fully taking into account all the higher order terms associated with interactions between the spins using the model described earlier. This results in 193 unique PELDOR signals for each correlation (not counting symmetry related solutions).To simplify the analysis the signals are then decomposed into a smaller number of principal components that each contain a weighted average of all the signals. The optimum number of principal components depends on the signal to noise of the experimental PELDOR signals, but in the cases discussed here, with relatively good signal to noise, around 50-100 components were found to give good results. A figure describing the data reduction process is shown in **Figure 6.3.1**.

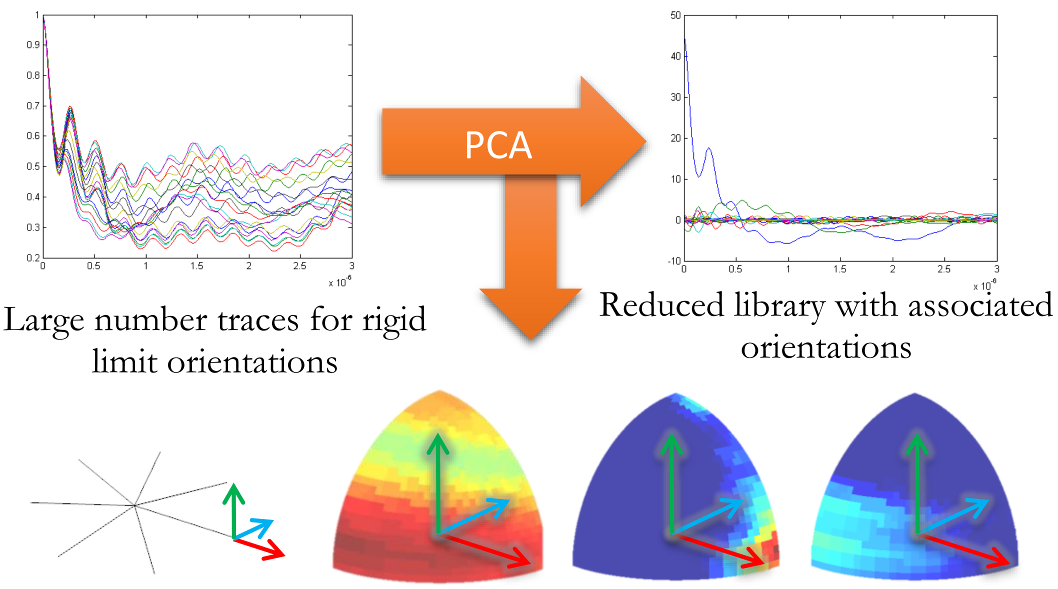

Figure 6.3.1 Diagram of the library reduction method for orientation PELDOR signals from cyclic symmetric oligomer label.

Each of the principal components will now contain frequencies corresponding to a range of distances between the nitroxide spins that also depend on their relative Euler angles. These principal components are then fitted simultaneously to the six experimental correlated PELDOR signals for a given radius r. This provides the most likely distribution of Euler angles for a given radius r. Fitted spectra are then calculated for each of the PELDOR experiments for that radius r and the calculated angular distribution. Obviously in many cases the fits will be poor as there will be little correlation with the observed spectra, but these will not contribute to the final fit.

This process is then repeated across a range of radii r, with a radial increment of either 0.25 or 0.5 Angstrom. This generates a library of correlated signals for different radii r each containing the most likely angular distribution of the spin labels for that radius r. We then use a Tikhonov regularization process to least squares fit this library of spectra to each experimental PELDOR traces simultaneously. The best fit then provides a data set where the angular distribution and the radial distance distribution are strongly correlated. The calculated distance distribution then corresponds to the radial distance r from the symmetry axis to the mid-point of the NO bond. It is then possible by considering the underlying geometry to calculate the inter spin label distances by calculation.

Note this last fitting step is similar to the calculation in the DEERAnalysis package, except we are now simultaneously fitting to six separate spectra and we have pre-calculated the most likely angular distributions for each distance, instead of assuming the relative orientations of the spin labels are uniform. As with standard two-spin PELDOR, it is still an ill posed problem, and we note it is still possible to both over-fit and under-fit the data and sensible choices still need to be made with regard to angular and distance resolution and the number of principal components – that all depend on the available signal to noise – and is informed by an associated L-curve.

In practice the calculation of the library of traces and its principal components for a symmetrical seven spin system, takes several days using a standard desktop PC. However, in principle the same library can be used again for a different measurement as long as the excitation pulses, the B_1 field and the spin Hamiltonian of the nitroxide spin label remain the same.

To test the algorithm several orientation test cases were used where the radius was kept fixed at 2.5 nm and a rigid single conformation was rotated to simulate the case of the nitrogen-oxygen bond of a nitroxide spin label, its gxx direction, being rotated from pointing out of the centre of the heptagon in the plane to pointing upwards perpendicular to the plane of the heptagon. Rotation in this example was limited to rotation around the gyy axis of the spin label. In each case the analysis derived orientation and distance matched within and error of ±10 degrees, and several examples are shown in **Figure 6.3.2**.

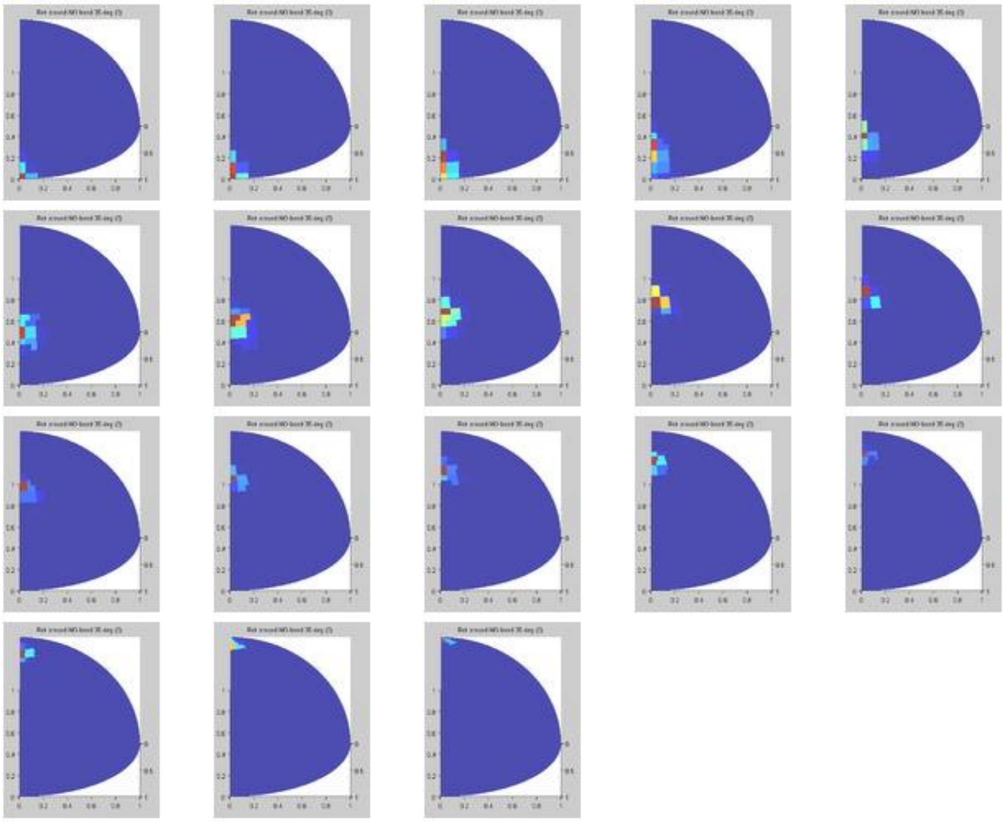

Figure 6.3.2 *Test of cyclic symmetric oligomer analysis algorithm, analysing different simulated cases of spin label being rotated from pointing straight out of the polygon plane rotating until perpendicular out of the plane.*

To test the analysis algorithm in the case where the conformation was no longer rigid orientation conformation, such as the cases used to build the library, but a cone spread such as what we might expect in a physical system. Again we get good agreement for the centre of the distribution as before, although the error in the width of the distribution is larger at ±15 degrees and this is shown in **Figure 6.3.3**.

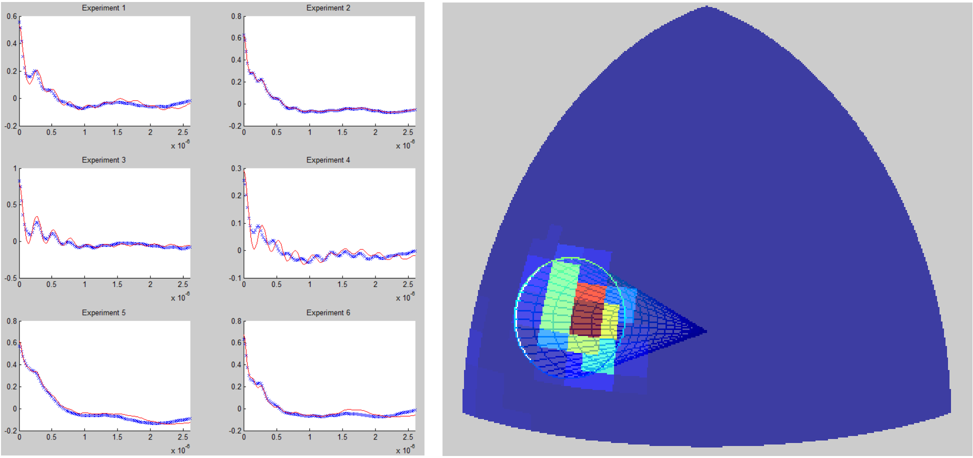

Figure 6.3.3 *Test case of analysing a cone distribution showing (left) the PELDOR signals simulated in blue and fitted result overlaid in red (right) the colour scale analysis result on a quarter sphere, where red indicates a predicted conformation angle and blue no conformation. Overlaid on the quarter sphere is the cone distribution inputted to simulated the test PELDOR signals.*

6.4. THE ANALYSIS OF ORIENTATION SELECTIVE PELDOR MEASUREMENTS OF MTSSL ON MSCS CHANNEL PROTEIN

The MscS sample was mutated to have spin labelling sites at several residues, and the ones which were prepared as part of the high-field EPR study were residues D67, L124 and S196 as shown in **Figure 6.4.1**. Further to this the samples were prepared to be in different environments, with the environments used in this study being bicelle and n-dodecyl-β-D-maltopyranoside (DDM) detergent. The bicelle is a model membrane layer which is formed of a lipid bilayer and DDM is a stabilised membrane environment which allows for the membrane protein to be suspended in solution. Due to availability of time and samples during the course of my study on this project the samples selected for orientation PELDOR study were the labelled sites S196 and L124. These sites were selected for their restricted spin label conformations, predicted using the available crystal models. The MscS sample spin labelled at site D67 was studied as a comparison to labelled site S196 for relaxation effect studies as residue D67 is in the transmembrane region, which sits inside the membrane, whilst residue S196 and L124 are outside of this region.

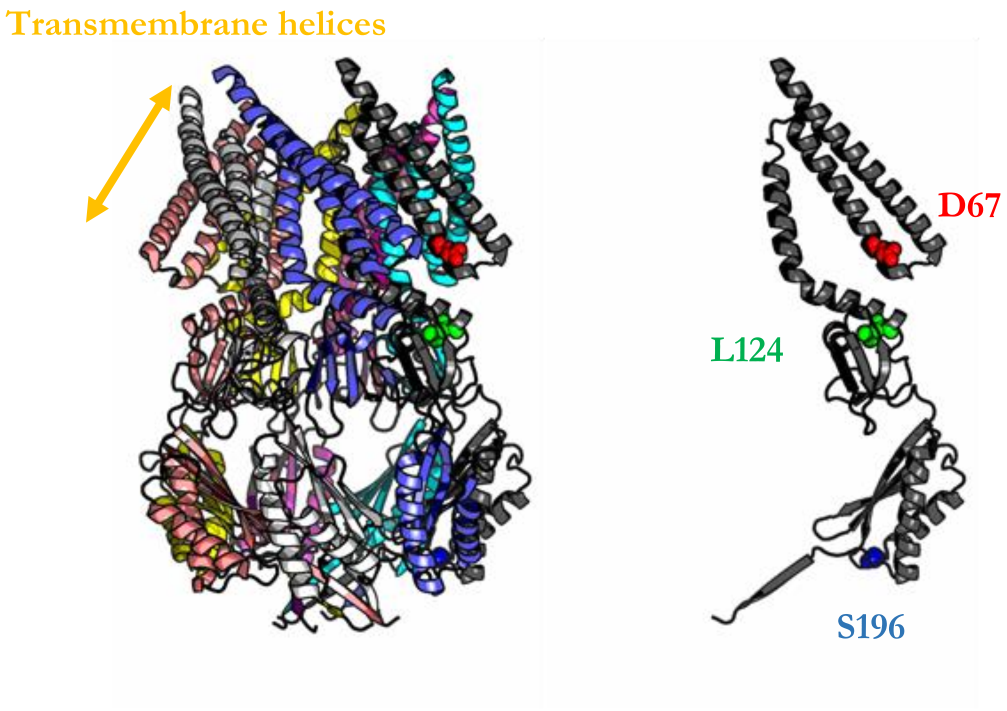

Figure 6.4.1 *Spin labelling sites for the MscS molecule, in this case the crystal model for the open form (PDB 2VV5). The label site label colours are consistent with* ***Figure 6.4.2****.*

CW data showed that the three sites in DDM environment have different mobility, most noticeable in how well resolved the two components of the axially symmetric hyperfine splitting A⊥ and A|| are, with nitroxide labelled at the D67 and S196 sites giving the most mobile CW spectrum and the L124 site being the least mobile spectrum seen in **Figure 6.4.2**. Another quantitative measure of spin label mobility is the so-called 2Azz' [112] which is the width of the EPR spectrum from the peak on the low field side to the trough on the high field side, where the higher value indicates a lower spin label mobility. It is also possible to use least squares fitting with the Budil-Freed MOMD model [113] which was done using the software package MultiComponent developed by Dr. Christian Altenbach from University of California, Los Angeles, California. The fitted CW lineshape reveals a value for the rotational correlation time of the nitroxide spin label, which is the average length of time it takes a spin label to rotate one radian. When the spin label has a free motion independent of the underlying molecule it will have a shorter rotational correlation time being a small fast moving molecule, but as the spin label motion becomes more strongly related to the motion of the underlying molecule the rotational correlation time will tend towards the longer rotational correlation time of the comparatively large protein. The values of 2Azz' and rotational correlation time for each of the labelling sites are shown in **Table 6.4.1**, with the results agreeing with the original statement of label mobility at each site although the nitroxide spectrum at the D67 site is not so well resolved making it difficult to select a peak for calculating 2Azz'. The spectrum for the

D67 site may be due to a more complicated mobility or mixtures of populations.

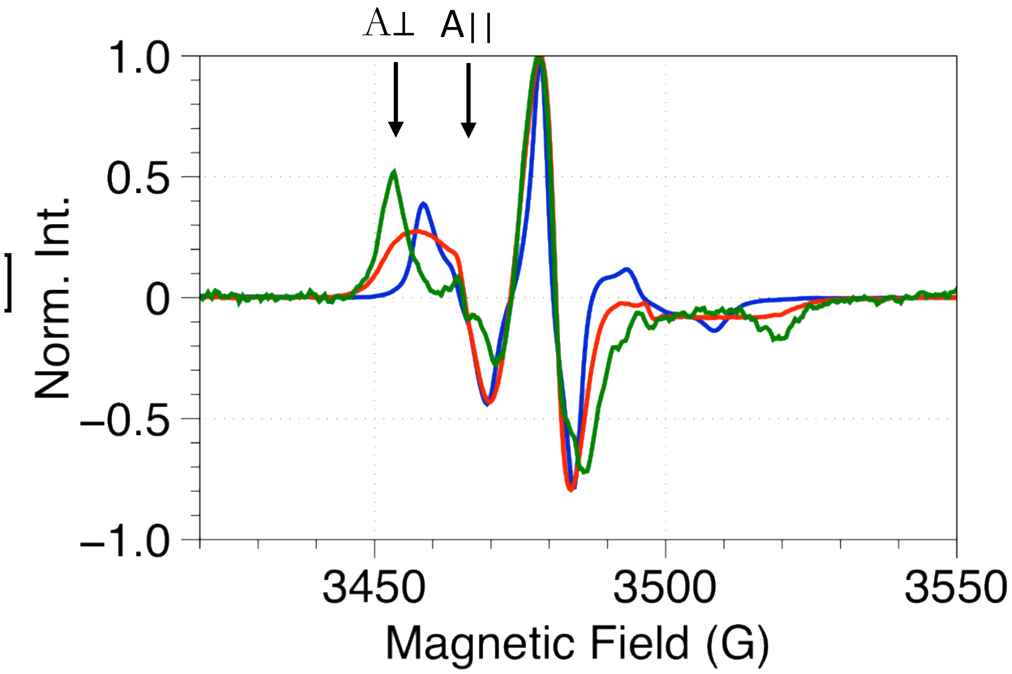

Figure 6.4.2 *CW signals of MTSSL labelled MscS in DDM detergent. (Red) MTSSL labelled to residue site D67 (Green) MTSSL labelled to residue site L124 and (Blue) MTSSL labelled to residue site S196.*

Labelling residue site	2Azz' (Gauss)	Correlation time (ns)
D67	53	4.78
L124	62	9.27
S196	51	3.61

Table 6.4.1 *Analysis of the CW signals for comparing mobility of the MTSSL label using 2Azz method and fitting of the CW signal to find the motion correlation time.*

From the CW data it is suggested that the labelling site L124 would yield the most restricted spin label conformation, with the S196 and D67 appearing to give a broader spin label conformation set. These are all measurements of the rotational motion of the spin labels made at room temperature and do not necessarily relate directly to the frozen sample spin label conformation set, although it will be a strong indication of the expected range of the conformation set. To further study the potential spin label conformations in the frozen sample state a prediction of the spin label rotamers was made using the MMM software from the Jeschke lab [114]. The prediction was made using the x-ray crystallography structure of the open form of MscS (PDB 2VV5) and the cryogenic temperature MTSSL rotamer library (175 K). It is noted that the temperature difference is 66% of the library temperature of 175 K, although it is expected that the prediction will be able to illustrate large conformation set differences between the labelling sites. The MMM predicted spin label conformation set centred on the amino acid backbone for each of the three labelling positions, showing the nitrogen-oxygen atoms for each of the predicted spin label conformations coloured to match the label positions in **Figure 6.4.3**. The MMM results were filtered to only show rotamers which had predicted occupancy of >2% such that small occupancy rotamers are excluded from the plot. It is noted that these spin label conformation predictions were also made using the x-ray crystallography structure of the closed form of MscS (PDB 2OAU) and negligible differences in the predicted conformation to the open form (PDB 2VV5) was seen due to the environment of the molecule are these sites being largely independent of the channel state.

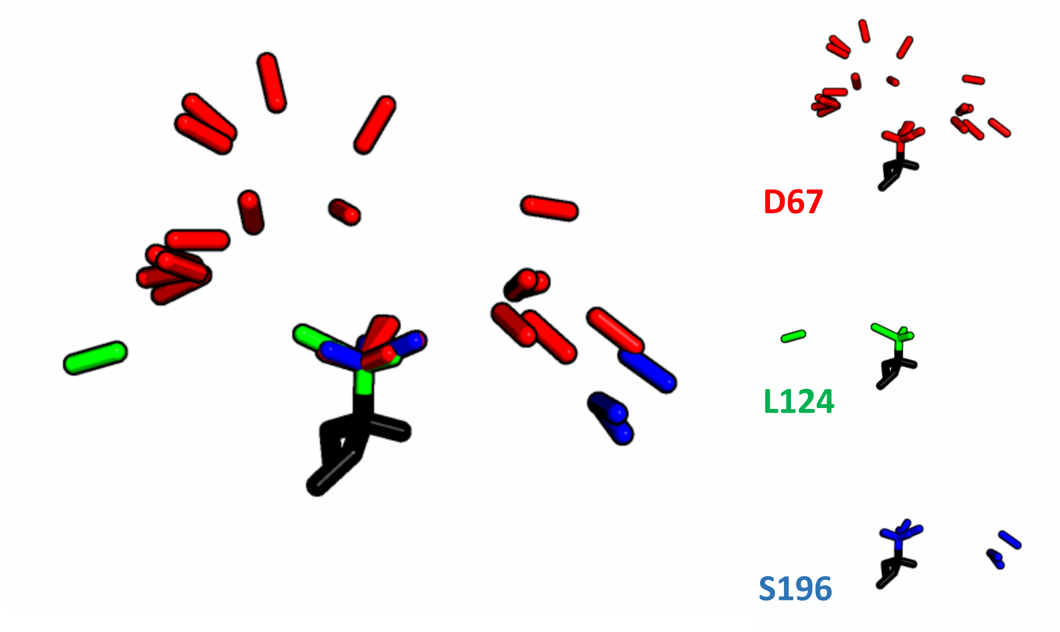

Figure 6.4.3 *Predicted spin label conformations for the MTSSL label attached to the residue sites D67 (red), L124 (green) and S196 (blue) as indicated in the figure using MMM package. (Left) overlaid all three distributions normalised to the atom locations of the underlying protein backbone. The back atom sticks show the common protein backbone atoms to each of the predicted conformations, connected to shown the first bond in the colour corresponding to the labelling site. The cloud of sticks represent the connected positions of the nitrogen and oxygen atoms of the MTSSL label.*

The MMM predictions indicate that the labelling site D67 will have the largest conformation spread for the MTSSL label, which agrees with the motion analysis, and that the site L124 will have the smallest conformation spread for the MTSSL label. However, the predicted spread of the conformations for the labelling sites D67 and S196 have a larger difference than is indicated by their CW lineshape mobility, with D67 site having the larger predicted conformation spread compared with the S196 labelling site which has a comparatively small spread predicted.

Using the CW lineshape analysis together with the rotamer predictions as a guide, the initial orientation PELDOR studies concentrated on the labelling sites S196 and L124 using the MTSSL spin label. PELDOR data was recorded for the largest possible time window yielding a signal to noise such that all of the PELDOR signals could be recorded within the available spectrometer time, in some cases this allowed for only a few PELDOR signals to be recorded, in particular PELDOR data shown for MscS labelled at site S196 in DDM detergent had poor signal to noise which significantly limited the number of different orientation selective experiments made. The recorded PELDOR signals for the different cases with the pulse excitation profiles and the distance distribution solved by Tikhonov regularised spin-pair fitting analysis are shown in **Figure 6.4.4**. Power correction scaling was enabled for 7 spin labels prior to performing the distance distribution fitting.

PELDOR signals for S196 in bicelle

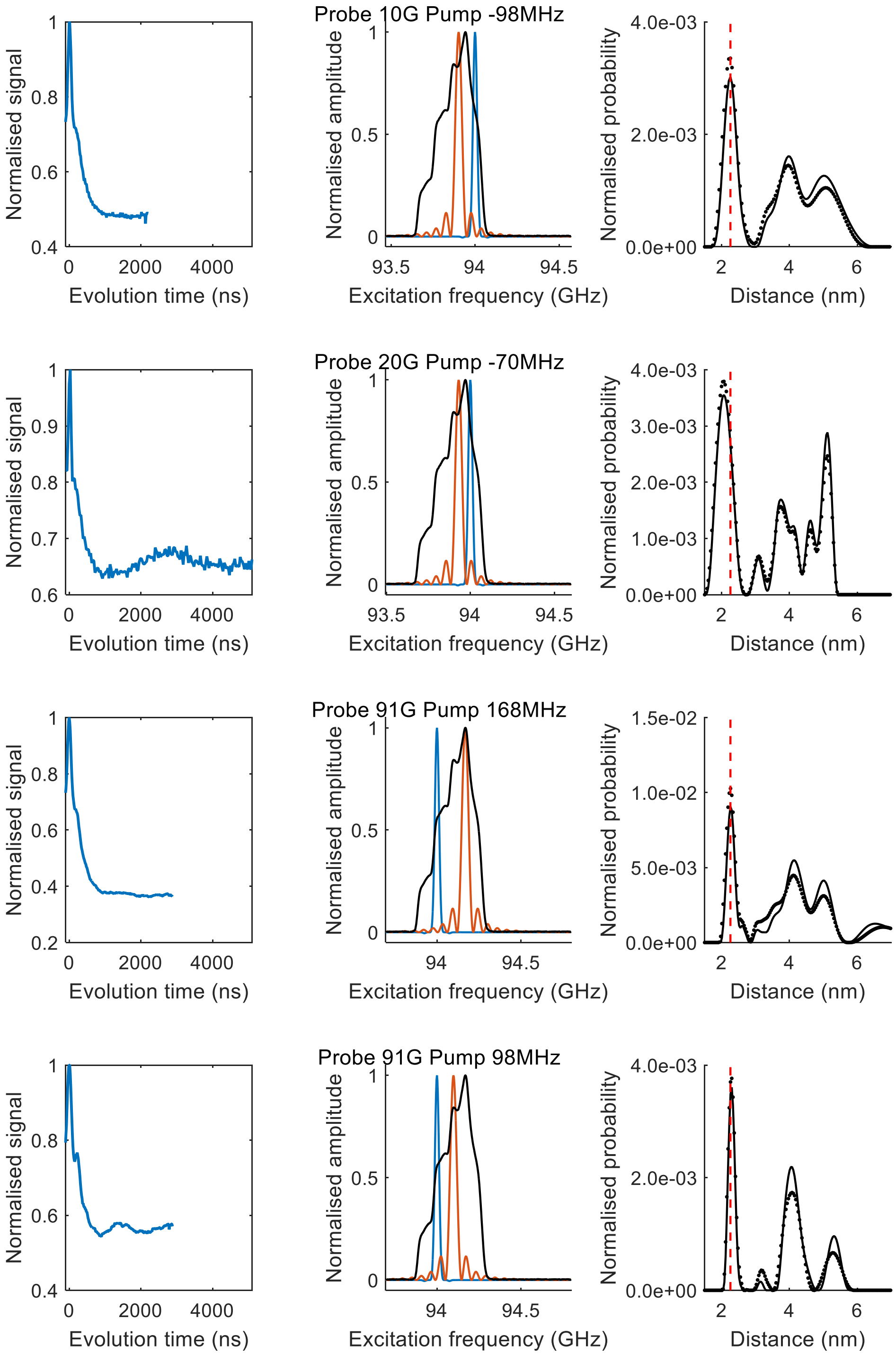

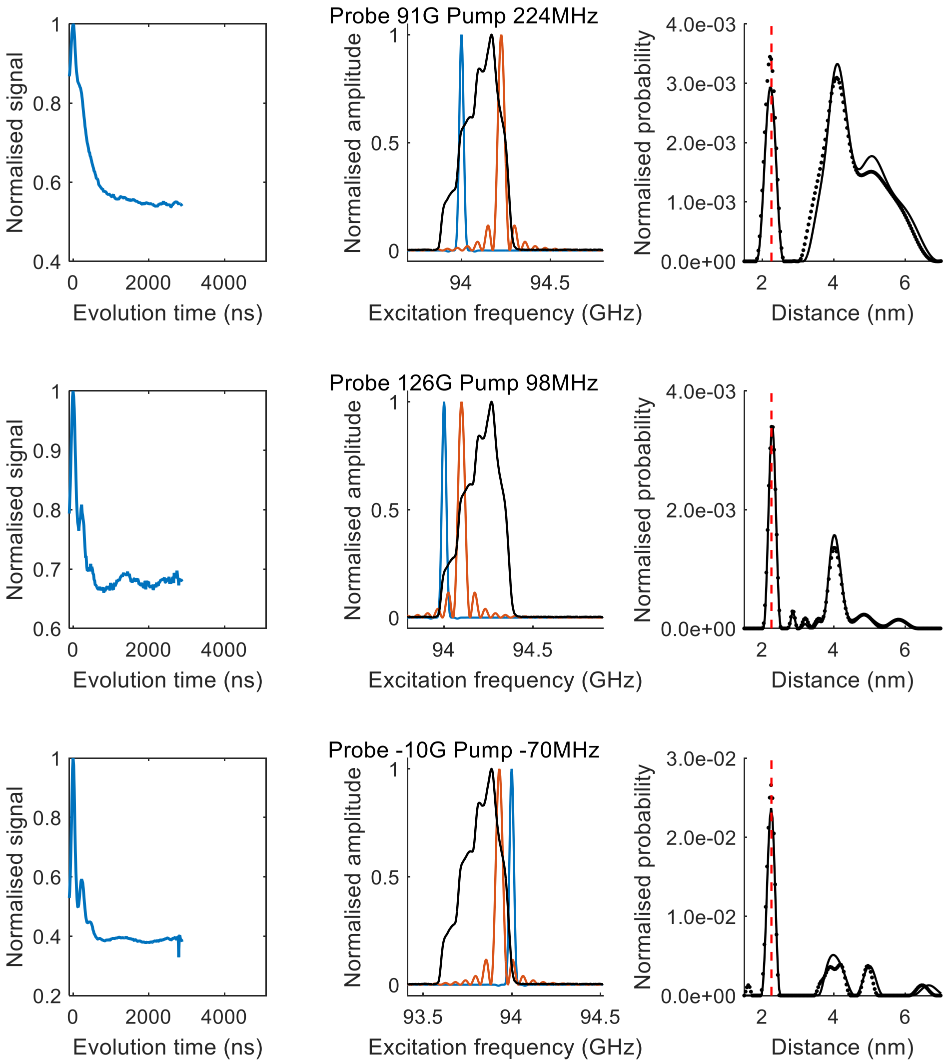

Figure 6.4.4 PELDOR signals for MTSSL labelled site S196 in bicelle (Left) Signal for each PELDOR experiment (Centre) pulse excitation profiles used in each experiment and (Right) the derived distance distribution using DeerAnalysis, solid line using the power scaling correction and dotted line without the correction.

PELDOR signals for S196 in DDM

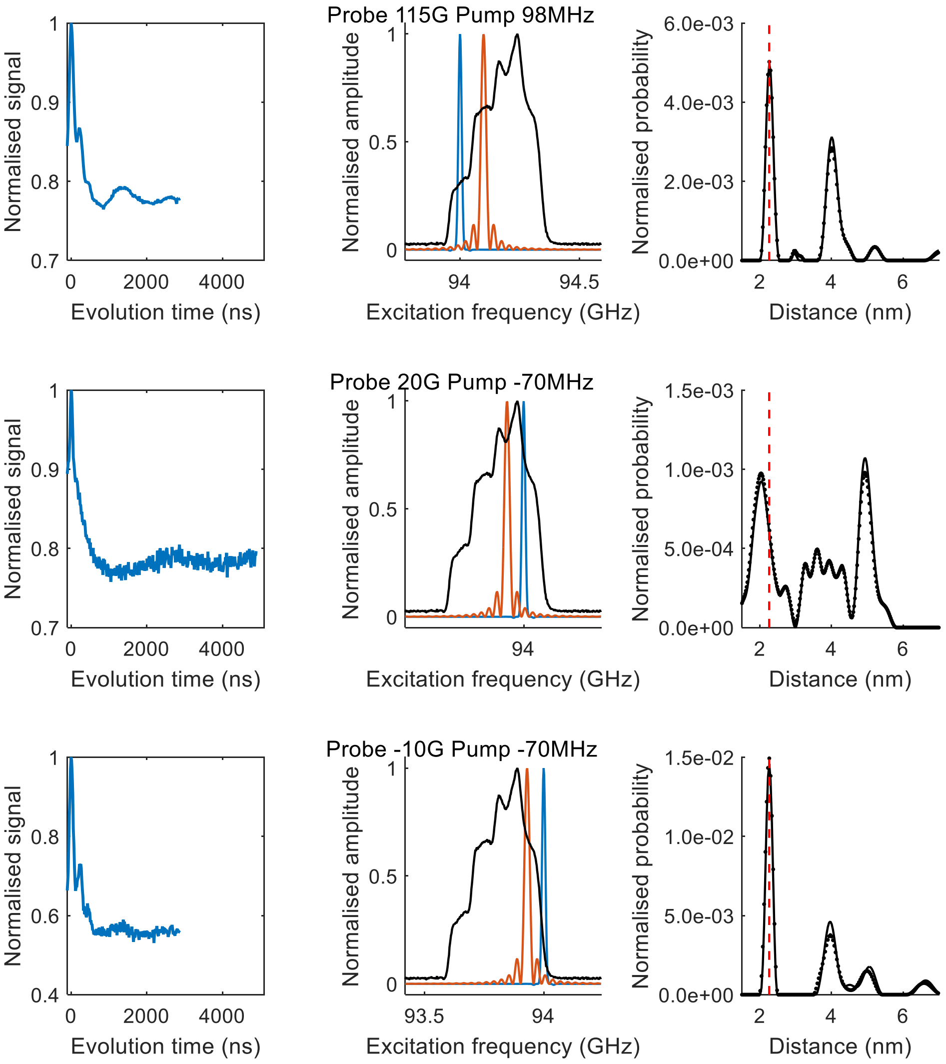

Figure 6.4.5 PELDOR signals for MTSSL labelled site S196 in DDM (Left) Signal for each PELDOR experiment (Centre) pulse excitation profiles used in each experiment and (Right) the derived distance distribution using DeerAnalysis, solid line using the power scaling correction and dotted line without the correction.

PELDOR signals for L124 in bicelle

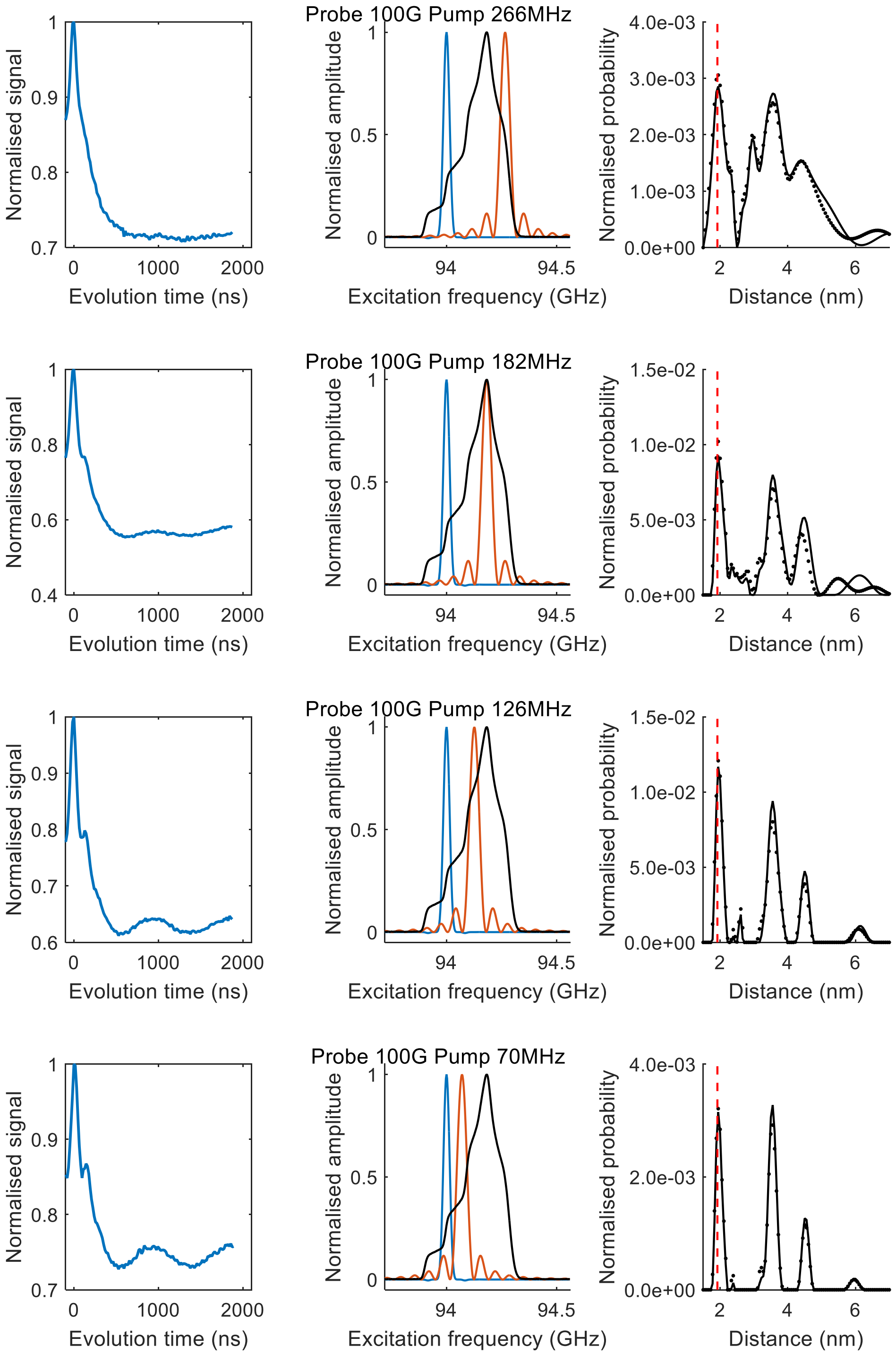

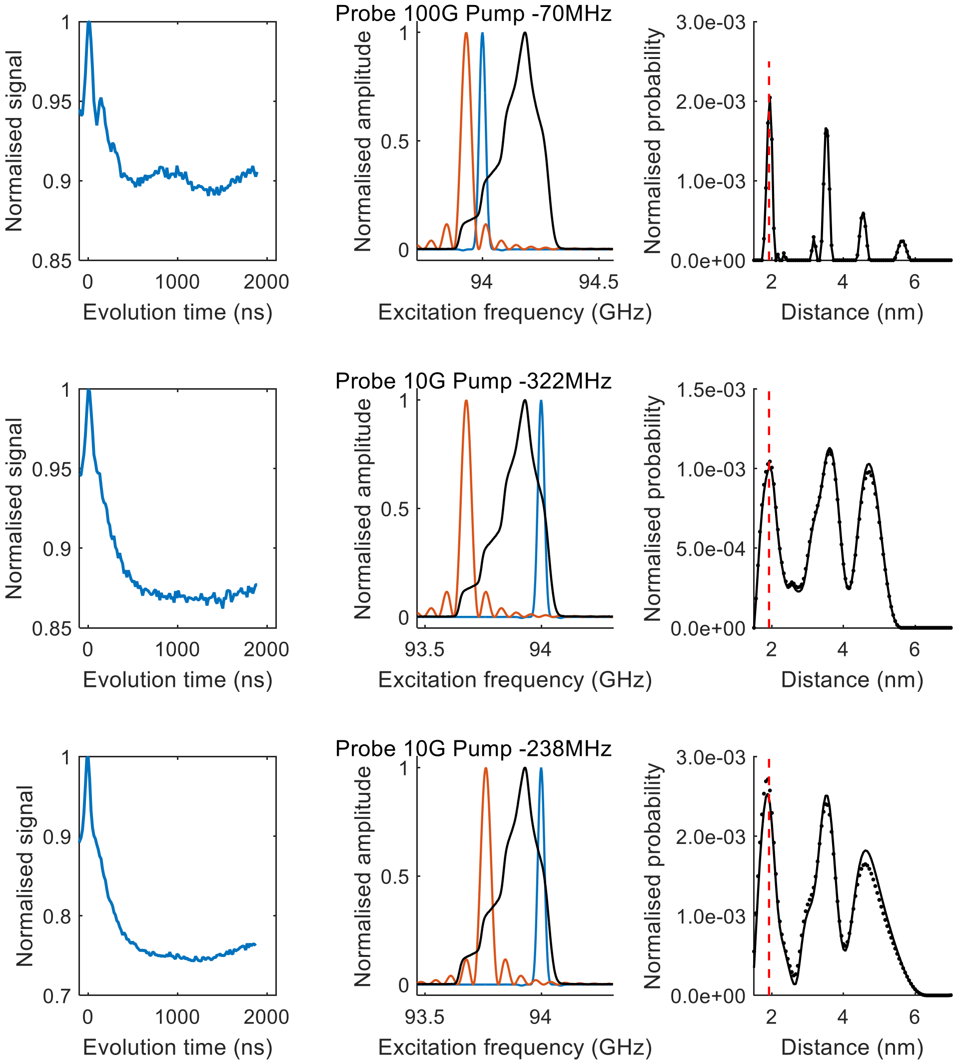
Normalised signal
Evolution time (ns)
0
1000
2000
0.85
0.9
0.95
1
Probe 100G Pump -70MHz
Normalised amplitude
Excitation frequency (GHz)
94
94.5
0
0.5
1
Normalised probability
Distance (nm)
2
4
6
0.0e+00
1.0e-03
2.0e-03
3.0e-03
Probe 10G Pump -322MHz
93.5
94
5.0e-04
1.0e-03
1.5e-03
Probe 10G Pump -238MHz
0.7
0.8
0.9

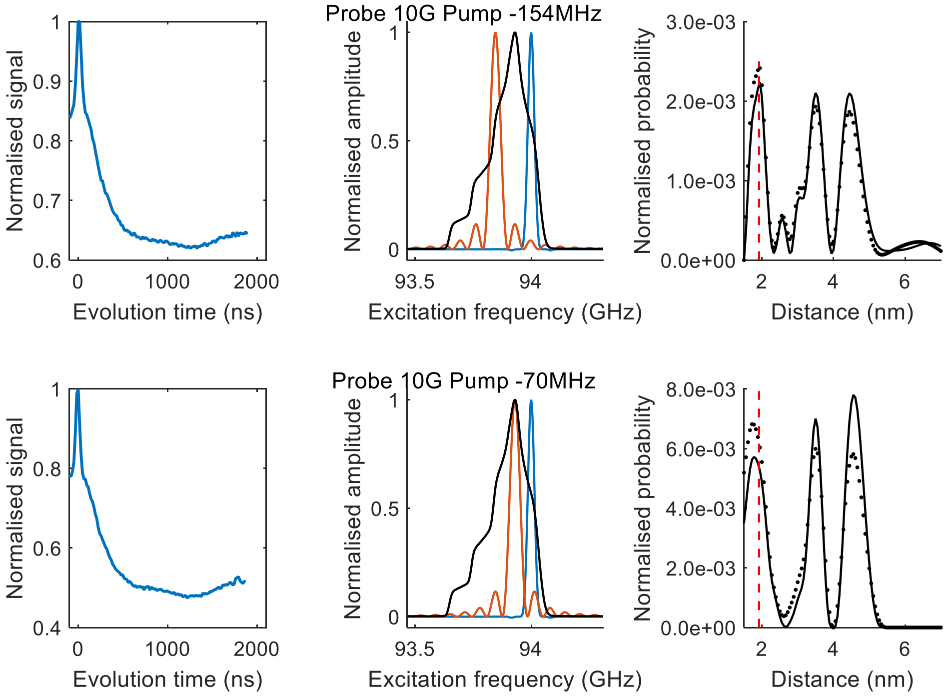

Figure 6.4.6 *PELDOR signals for MTSSL labelled site L124 bicelle (Left) Signal for each PELDOR experiment (Centre) pulse excitation profiles used in each experiment and (Right) the derived distance distribution using DeerAnalysis, solid line using the power scaling correction and dotted line without the correction.*

PELDOR signals for L124 in DDM

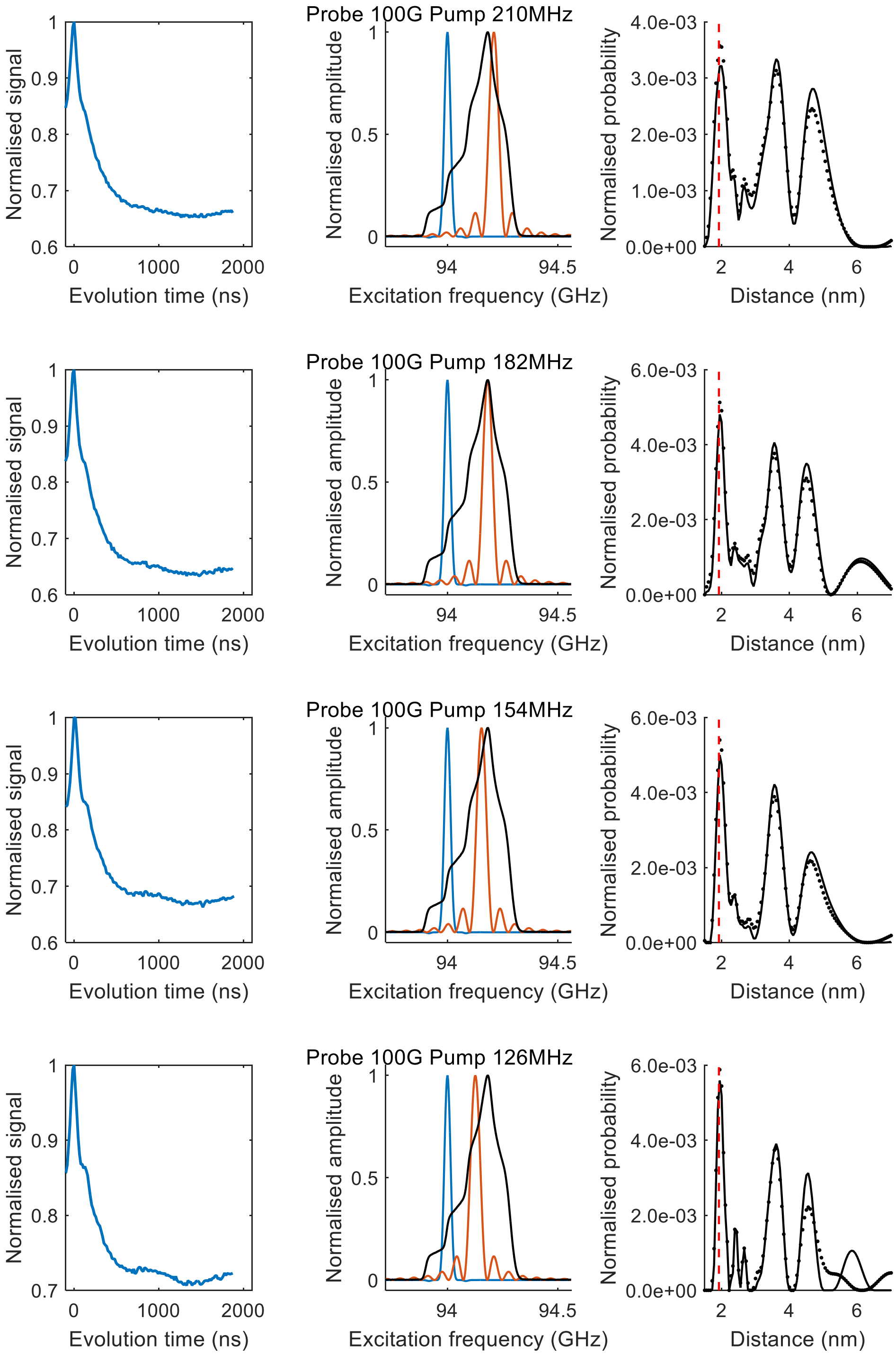

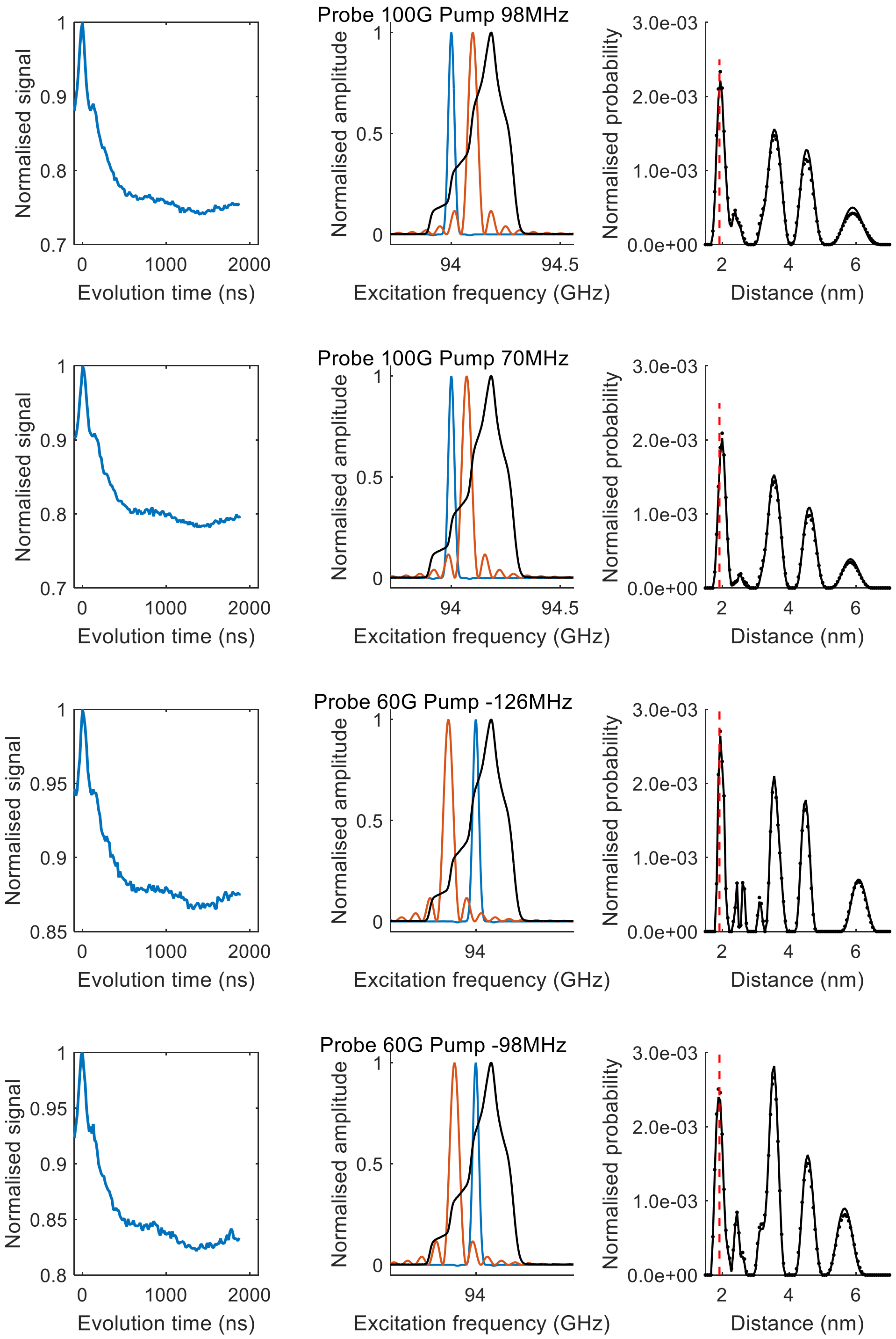
Normalised signal
Evolution time (ns)
0
1000
2000
1
0.9
0.8
0.7
0.95
0.85
Probe 100G Pump 98MHz
Probe 100G Pump 70MHz
Probe 60G Pump -126MHz
Probe 60G Pump -98MHz
Normalised amplitude
Excitation frequency (GHz)
94
94.5
0.5
Normalised probability
Distance (nm)
3.0e-03
2.0e-03
1.0e-03
0.0e+00
2
4
6

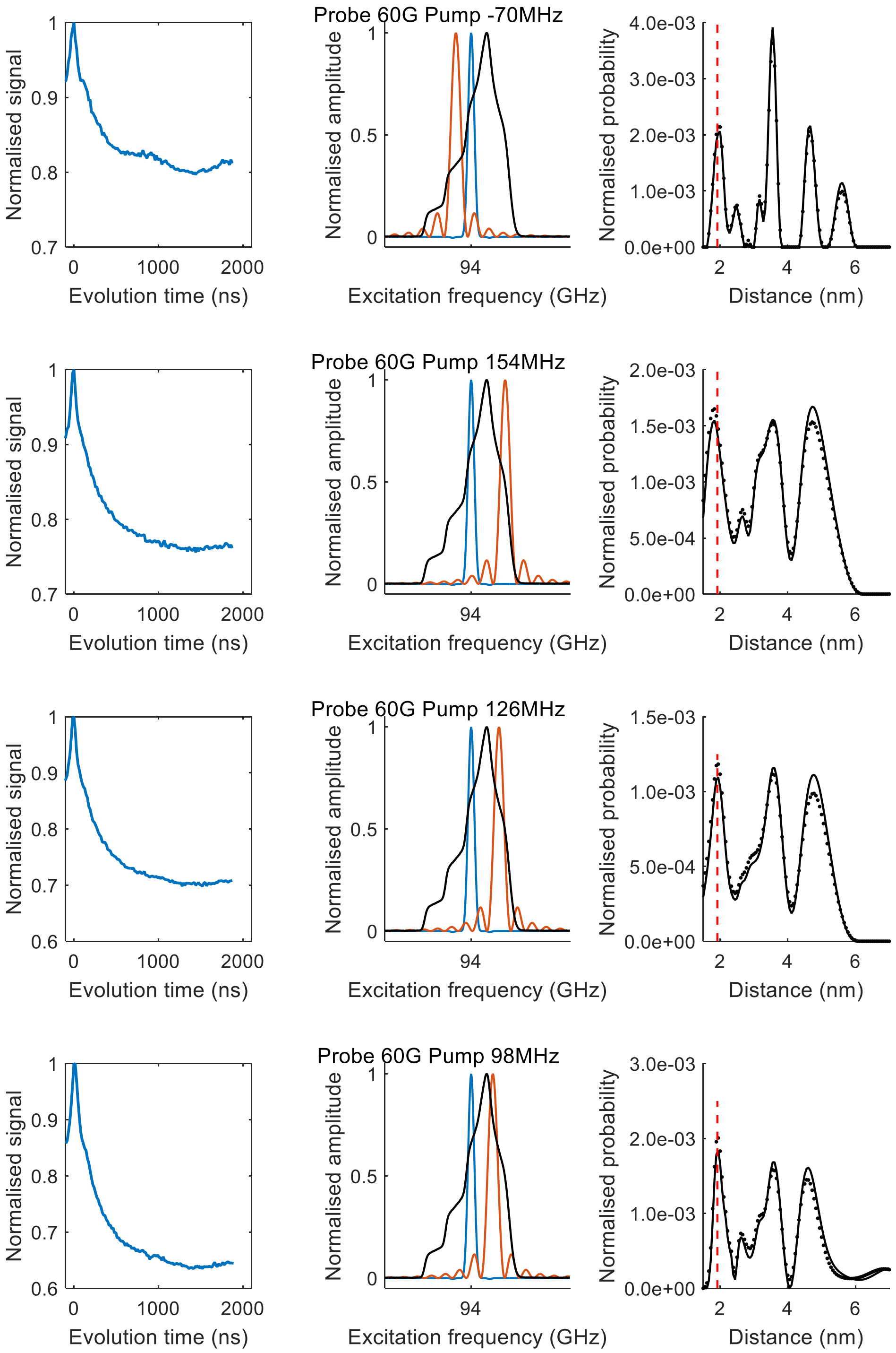
Probe 60G Pump -70MHz
Probe 60G Pump 154MHz
Probe 60G Pump 126MHz
Probe 60G Pump 98MHz
Normalised signal
Evolution time (ns)
0
1000
2000
0.6
0.7
0.8
0.9
1
Normalised amplitude
Excitation frequency (GHz)
94
0
0.5
1
Normalised probability
Distance (nm)
2
4
6
4.0e-03
3.0e-03
2.0e-03
1.5e-03
1.0e-03
5.0e-04
0.0e+00

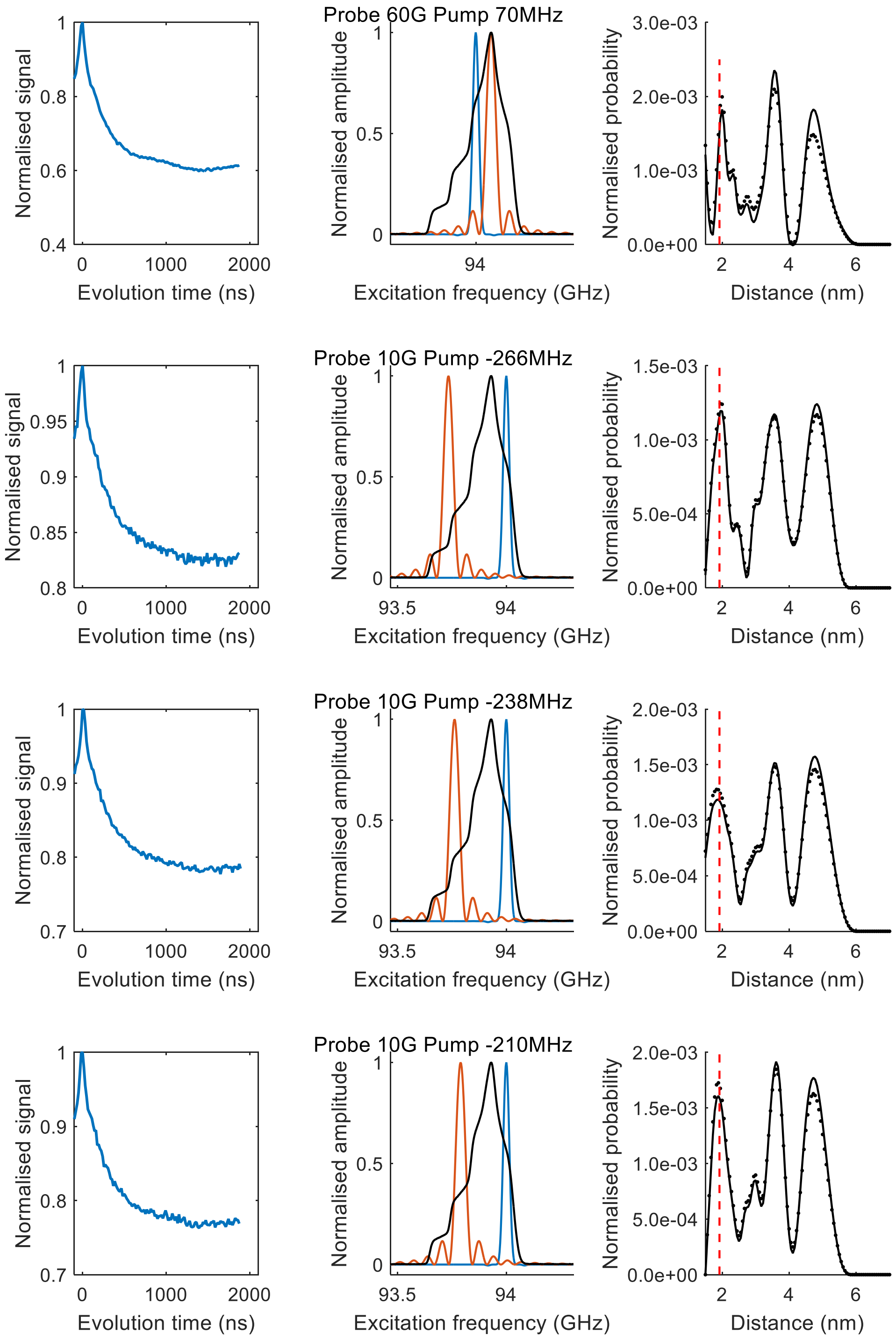
Probe 60G Pump 70MHz
Probe 10G Pump -266MHz
Probe 10G Pump -238MHz
Probe 10G Pump -210MHz
Normalised signal
Evolution time (ns)
0
1000
2000
0.4
0.6
0.8
1
0.85
0.9
0.95
0.7
Normalised amplitude
Excitation frequency (GHz)
93.5
94
0
0.5
Normalised probability
Distance (nm)
2
4
6
0.0e+00
1.0e-03
2.0e-03
3.0e-03
5.0e-04
1.5e-03

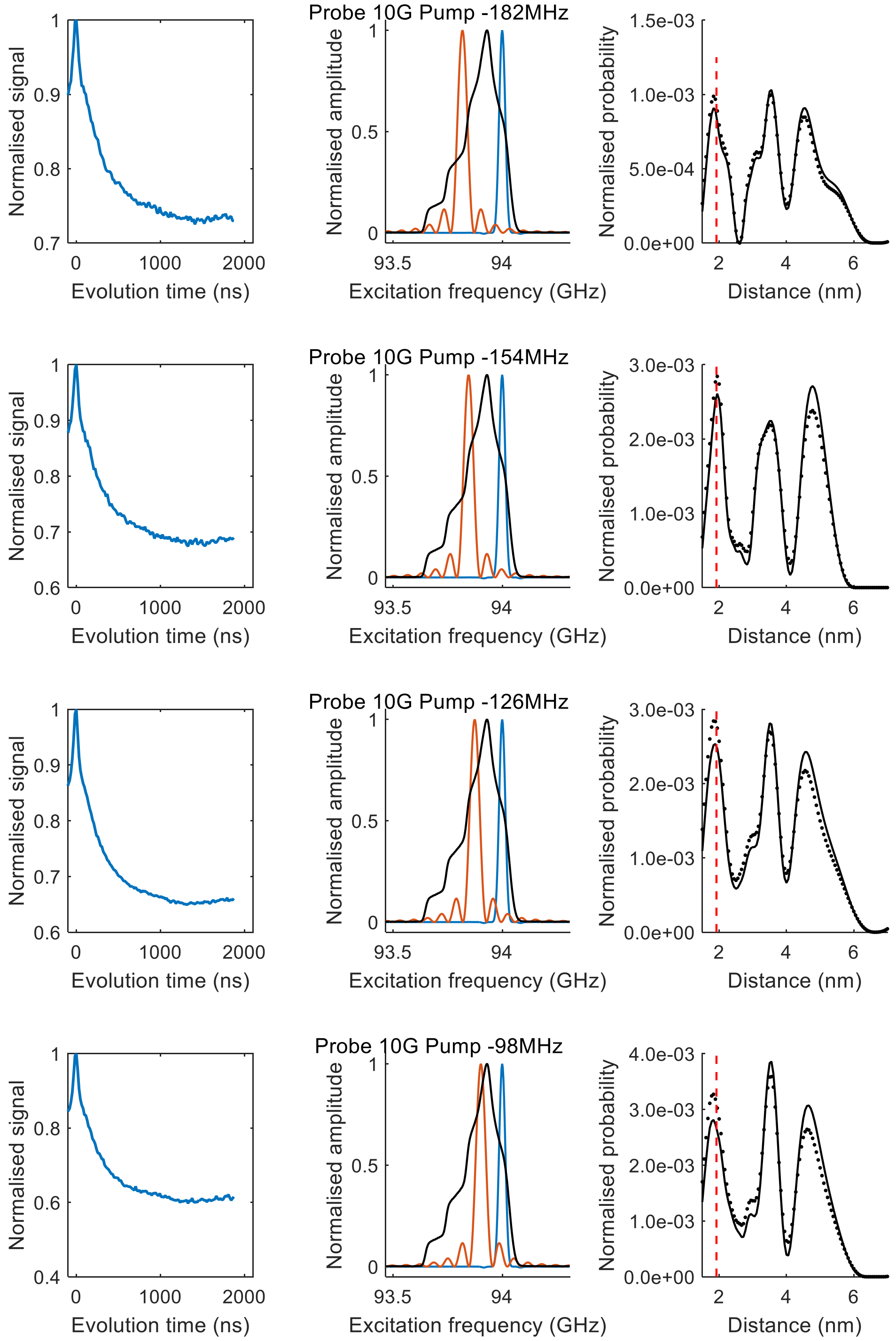
Probe 10G Pump -182MHz
Probe 10G Pump -154MHz
Probe 10G Pump -126MHz
Probe 10G Pump -98MHz
Normalised signal
Evolution time (ns)
0
1000
2000
1
0.9
0.8
0.7
0.6
0.4
Normalised amplitude
Excitation frequency (GHz)
93.5
94
0.5
Normalised probability
Distance (nm)
2
4
6
0.0e+00
5.0e-04
1.0e-03
1.5e-03
2.0e-03
3.0e-03
4.0e-03

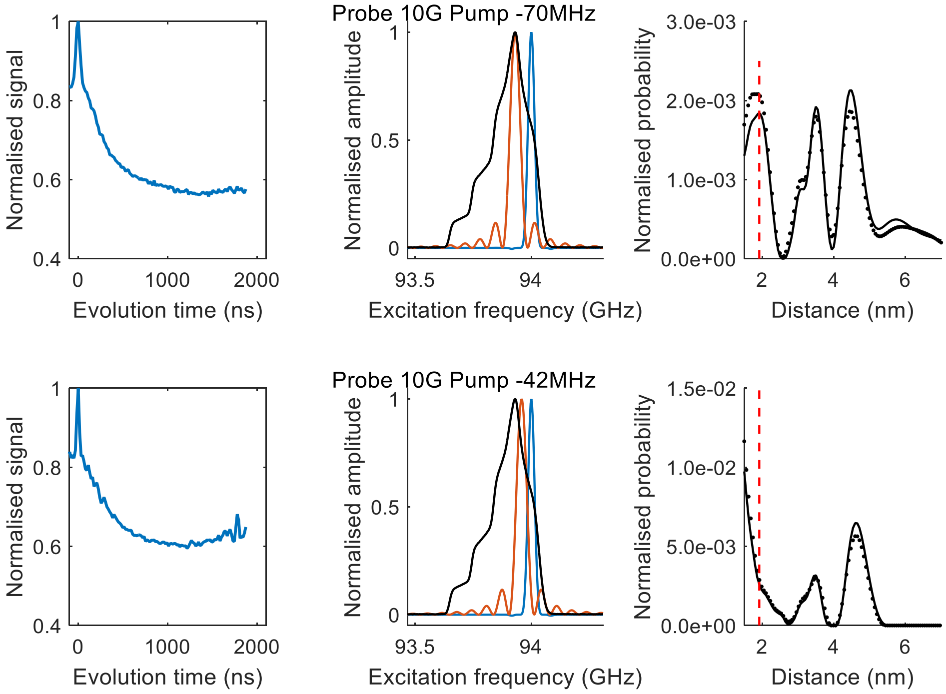

Figure 6.4.7 *PELDOR signals for MTSSL labelled site L124 DDM (Left) Signal for each PELDOR experiment (Centre) pulse excitation profiles used in each experiment and (Right) the derived distance distribution using DeerAnalysis, solid line using the power scaling correction and dotted line without the correction.*

The PELDOR signal modulations for both the S196 and L124 MTSSL labelled sample in bicelle and DDM has a strong dependence on the pulse excitation positions on the spectrum which would be consistent with the expected signal response when the spin labels have strong orientation correlation as suggested by simulations. As an initial analysis the distance of the first peak in the Tikhonov regularised spin-pair fitted distance distribution was averaged across each of the PELDOR signals and found for S196 to be 2.26 nm for both the bicelle and the DDM environment. The bicelle and DDM distances were expected to agree due to limited structure change between open and closed states of MscS based on the open and closed state crystal models. This average distance is labelled for each case and is marked as a line on the distance distributions to illustrate the consistency between the different PELDOR signals. The larger distances are found to vary in intensity and width such that they were not considered reliable.

However, the short distance could still be compared to the average of the shortest distance in the heptagon geometry of the MscS molecule based on the MTSSL spin label rotamer prediction from the MMM software and was also compared to the spin label conformation prediction software MTSSLWizzard [115]. The average of the shortest distance predicted for the closed state crystal model (PDB 2OAU) found by MMM was 2.05 nm (the predicted distribution is bi-modal for the open state with a distance predicted at 1.7 nm and 2.05 nm) and the average of the shortest distance found by MTSSLWizzard was 2.19 nm (2.18 nm for the open state). This is a difference of 0.21 nm between the MMM prediction and the experimental result and 0.14 nm between the MTSSLWizzard prediction and the experimental result. Differences in the prediction approaches and comparison cases of the two techniques have been discussed in depth previously [115].

An attempt was made to input the experimental data into the fitting algorithm previously presented, however, several problems where encountered relating to repeatability of PELDOR signals. PELDOR signals would have different modulation amplitude depending on the pulse timing, with the analysis model assuming that the signal is independent of pulse timing. Strong instantaneous diffusion effects originating from the spins within the molecule were observed which may be causing differential relaxation between molecules in the sample and distorting the PELDOR signal. A change in sample concentration would lead to different modulation depths for the same experiment conditions, even when sample stock was consistent. Further details are presented for each observation.

Due to these problems with results and the significant time required for analysis only the first available PELDOR signals were processed using the algorithm, with the discussed problems being observed during the measurement of those signals. The sample in this case was MscS labelled with MTSSL at residue site S196. These results are presented as an example of the results from the algorithm, although there is doubt over the input PELDOR signals.

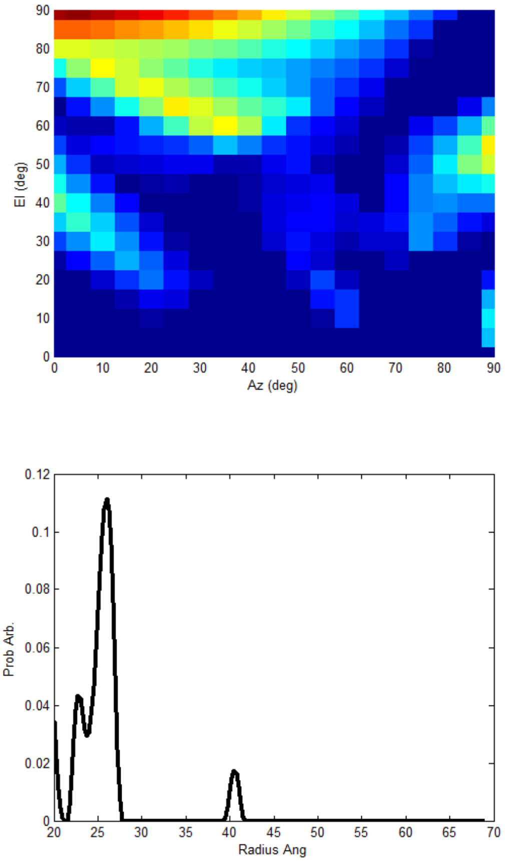

Figure 6.4.8 *Orientation PELDOR analysis results of MscS labelled with MTSSL at residue site S196 in DDM (Top) colour scale plot showing predicted angles of the NO bond of the spin label relative to the frame shown in* ***Figure 6.2.3*** *plotted in the spherical coordinates (bottom) the radius distribution fitted to the experimental data using the analysis described.*

6.5. CONCLUSIONS

An exploration of the measurement and analysis of orientation PELDOR experiments has been made, particularly for the spin labelled membrane protein MscS. The theory of the experiment for multiple spins was discussed and a model for analysis based on principal component analysis is presented. This model uses a large library of computer simulated PELDOR signals and uses data reduction and fitting algorithms, which have been previously applied to other spectroscopy techniques, to determine the relative orientations of spin labels on cyclically symmetric homo-oligomeric structures. The model was tested against computer simulated test cases and gave consistent results which agreed with the input parameters of the simulations. Several PELDOR experiment measurements of the sample MscS were made with the sample in different lipid environments and these measurements are presented in this chapter. First pass analysis of these measured PELDOR signals showed deviations of the signals for the expected range obtained by both signal simulations and investigation of the PELDOR signal approximation. Variations in the PELDOR signal as a function of the spin echo refocussing time of the sequence was also observed which is not predicted by the PELDOR signal approximation. One mechanism which could cause this, and also be consistent with the variations in the PELDOR signals is a relaxation mechanism which depends on the number of spin labels attached to a molecule and the number of spin labels excited by the spin echo stimulated by the PELDOR experiment. A brief investigation into these effects will be made in the next chapter.

Chapter 7 SPIN ECHO RELAXATION STUDIES OF THE MEMBRANE PROTEIN MSCS WITH MULTIPLE SPIN LABELS.

This chapter will investigate and present measurements of the spin echo phase memory time of multiple spin labels attached to the homo-oligomer protein

MscS as presented in Chapter 6. An attempt is made to establish the mechanism which dominates the spin echo phase memory time and compare the measurements between the same protein sample in different environments of detergent and model membrane layers.

7.1. PELDOR SIGNAL DEPENDENCE ON PULSE TIMING

During the PELDOR experiment it was noted that the PELDOR signals had modulations which would vary with the time that the final π refocusing pulse was applied relative to the first π focusing pulse in the observer sequence, that is the time τ2 as shown in **Figure 7.1.1**.

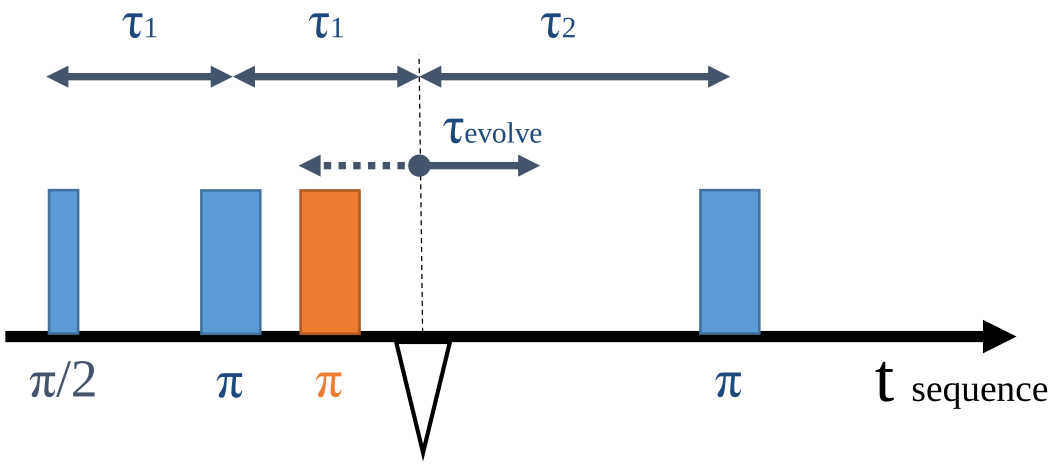

Figure 7.1.1 *4-pulse PELDOR experiment sequence.*

Effects have been previously reported in literature, with the variation being attributed to clustering and differential relaxation, however, in those cases the modulation depth would change by several percent with cases seen in these measurements showing the modulation depths would stay broadly consistent as the time τ2 was changed but the relative amplitude of the frequency components would change, shown in **Figure 7.1.2**.

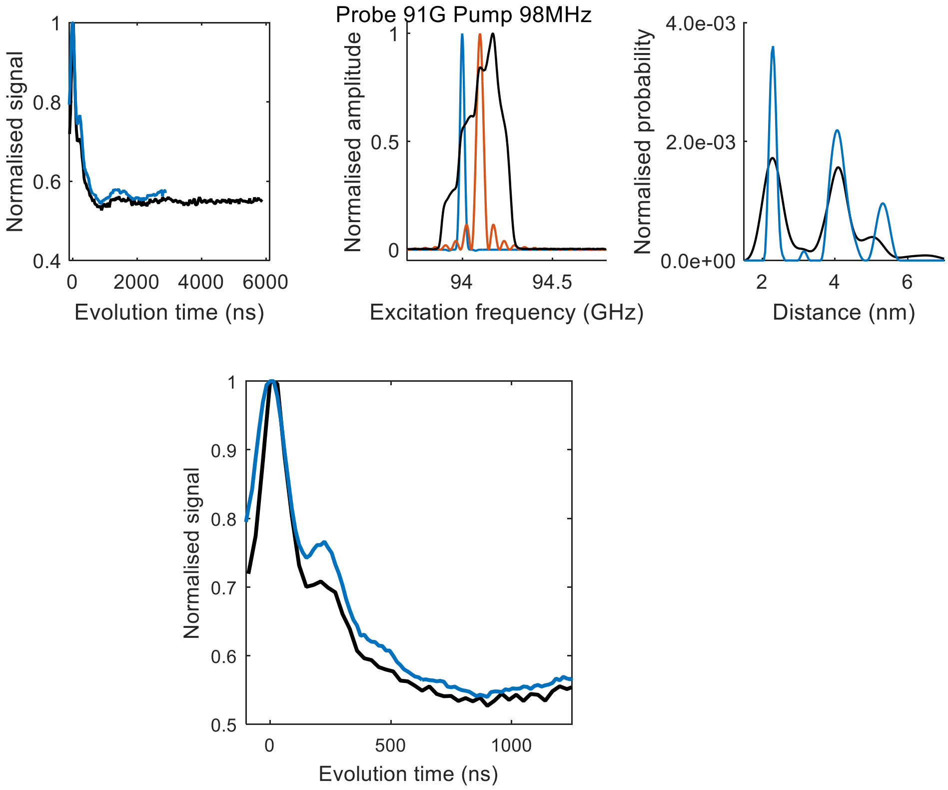

***Figure 7.1.2** Comparison of two PELDOR signals using the same experimental parameters except for τ2 which was varied to give PELDOR signals with evolution times of 3000ns and 6000ns shown in blue and black respectively. (top left) Overlaid PELDOR signals. (top centre) Spin label spectrum with pulse excitation profiles used plotted for the (blue) observer pulses and (red) pump pulse. (top right) distance distributions derived using DeerAnalysis with the power scaling correction enabled and optimal regularisation chosen by L-curve. (bottom) PELDOR signals zoomed to show the amplitude difference of the high frequency components when the pulse timing is changed.*

The zoomed case of the high frequency component shown in **Figure 7.1.2**, which correspond to short distances, highlights differences between the short and long time signals showing that there is a notable dampening of these components as the time window was increased. This is reflected on the spin-pair Tikhonov regularised distance distribution fits. The signals used for the distance distribution had the power scaling correction proposed by Jeschke applied, and this correction requires the modulation frequency components to be at the expected relative amplitudes otherwise the corrected result will not tend toward the spin-pair signal. It is suspected that it is this misbalance of the modulation signals which leads to the difference in the distance distribution, despite comparable signal to noise of the signals and the optimal choice of regularisation parameter chosen by the L-curve method. It was suspected that there may be spin relaxation effects contributing to the changes in PELDOR signal as a function of pulse separation and further experiments were made to test for these conditions. As the modulation depth does not change this is evidence that the spin labelling efficiency is high, as there is an absence of differential spin relaxation normally associated with an inconsistancy in the number of spin labels attached to different molecules in the sample caused by inefficient spin labelling.

7.2. PHASE MEMORY TIME MEASUREMENTS AND EVIDENCE OF INSTANTANEOUS DIFFUSION IN THE HEPTAMER

Phase memory time measurements were measured for the different labelled sites and fitted to recover decay time constants. Three different models were used, (1) a single mono-exponential fit, (2) a mono-exponential plus x=2 stretch exponential and (3) a stretched exponential fit where x is fitted. Model (1) fits the case of dephasing being driven by purely T1 spin-lattice relaxation mechanism, instantaneous diffusion or any other fast mechanism, model (2) fits the case of a fast instantaneous diffusion process described by a mono-exponential and a slower nuclear spin diffusion mechanism described by a stretched-exponential with x=2, and model (3) fits a phenomenological case where the relaxation mechanism is general and x can range from 0.5 to 2 depending on the rate of the mechanism [116]. The equations representing these models are given by,

$$V_{TM}(t) = \exp\left(-\frac{t}{\tau_{\mathrm{ID}}}\right) \qquad (1)$$

$$V_{TM}(t) = A_1 \exp\left(-\frac{t}{\tau_{\mathrm{ID1}}}\right) + A_2 \exp\left(-\frac{t}{\tau_{\mathrm{ID2}}}^{2}\right) \qquad (2)$$

$$V_{TM}(t) = \exp\left(-\frac{t}{\tau_{\mathrm{ID}}}^{x}\right) \qquad (3).$$

Equation 7.2.1

Results of fitting the measured phase memory time T_M are shown in **Table 7.2.1** - **Table 7.2.4** for the two sample cases of the S196 labelled site sample and D67 labelled site, with 95% confidence bounds and adjusted R^2 values representing goodness of fit for each model. In the case of the two exponential fit a weight percentage is given with each decay constant and in the case of the stretched exponential the power is given as x.

The sites are selected as they reside in two distinct regions of the molecule, the transmembrane domain and the cytoplasmic domain. This has a particular relevance when comparing the bicelle environment to the DDM detergent environment where it would be expected that the D67 site being in the transmembrane domain should see a significant local environment change whilst the S196 site should not.

S196 bicelle	**Tm with single Exp (1)**	**Tm with two Exp (2)**	**Tm with stretch Exp (3)**
gxx	τ=2260±49 ns AdjR²=0.9345	82±3% τ=696±22 ns 18±3% τ=6772±98 ns AdjR²=0.9958	x=0.39±0.02 τ=272±2 ns AdjR²=0.9903
gyy	τ=1697±48 ns AdjR²=0.8966	89±2% τ=601±8 ns 11±2% τ=7225±71 ns AdjR²=0.9986	x=0.21±0.02 τ=1±1 ns AdjR²=0.9907
gzz	τ=2811±47 AdjR²=0.961	76±2% τ=841±12 ns 24±2% τ=7053±29 ns AdjR²=0.9974	x=0.54±0.02 τ=1142±124 ns AdjR²=0.9921

Table 7.2.1 *Table of fits to phase memory time measurements of sample labelled at site S196 in bicelle. Each column corresponds to a different model in* ***Equation 7.2.1*** *as indicated. The model which has the most consistent good fits, as indicated by the Adjusted R-squared and discussion in the text, is highlighted in green. Rows correspond to the g-factor component which the echo sequence pulse excited.*

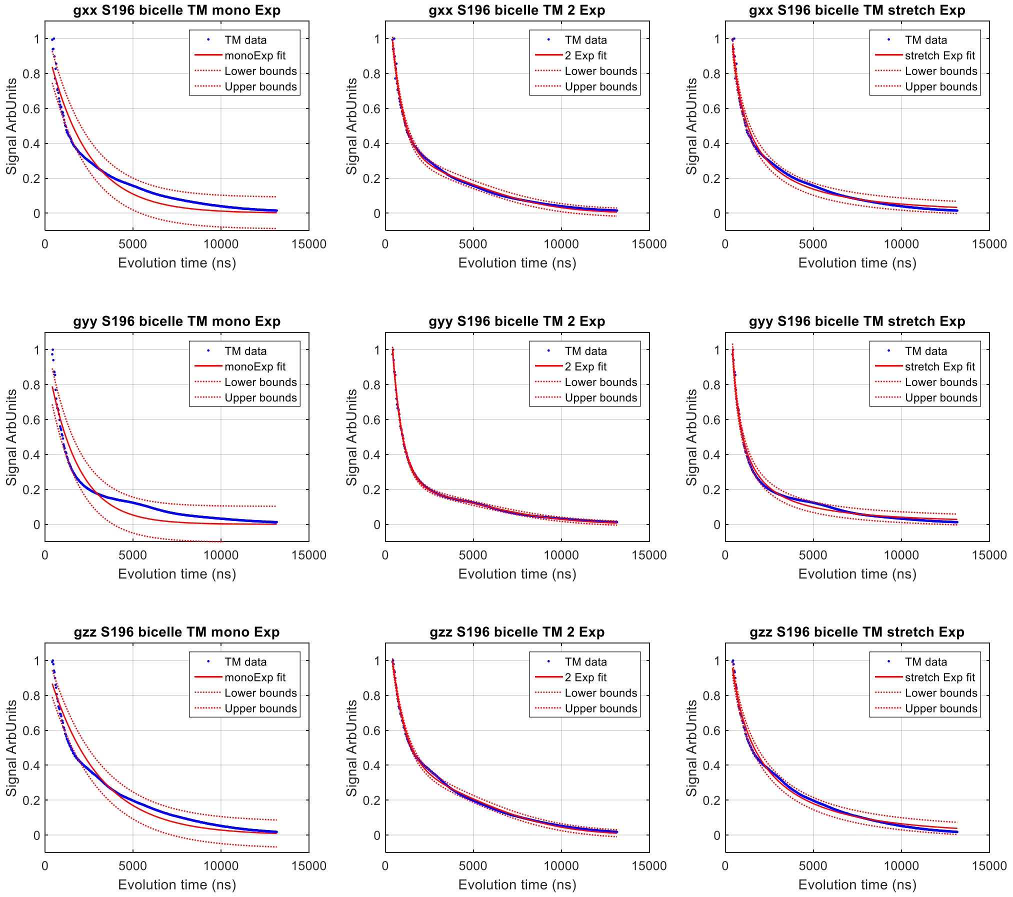

Figure 7.2.1 *Plots of the fits shown in* ***Table 7.2.1*** *shown in red overlaid on the experimental echo decay signals shown in blue. The light red lines surrounding the fit correspond to 95% confidence bounds of the fit.*

S196 DDM	**Tm with single Exp (1)**	**Tm with two Exp (2)**	**Tm with stretch Exp (3)**
gxx	τ=1315±39 ns AdjR²=0.9692	89±1% τ=625±20 ns 11±1% τ=4803±130 ns AdjR²=0.9959	x=0.38±0.02 τ=91±18 ns AdjR²=0.9977
gyy	τ=867±28 ns AdjR²=0.9676	95±3% τ=560±11 ns 5±3% τ=5472±172 ns AdjR²=0.9970	x=0.25±0.02 τ=2±2 ns AdjR²=0.9975
gzz	τ=1826±47 ns AdjR²=0.9756	83±2% τ=710±20 ns 17±2% τ=5165±83 ns AdjR²=0.9977	x=0.50±0.02 τ=450±3 ns AdjR²=0.9973

__Table 7.2.2__ Table of fits to phase memory time measurements of sample labelled at site S196 in DDM. Each column corresponds to a different model in __Equation 7.2.1__ as indicated. The model which has the most consistent good fits, as indicated by the Adjusted R-squared and discussion in the text, is highlighted in green. Rows correspond to the g-factor component which the echo sequence pulse excited.

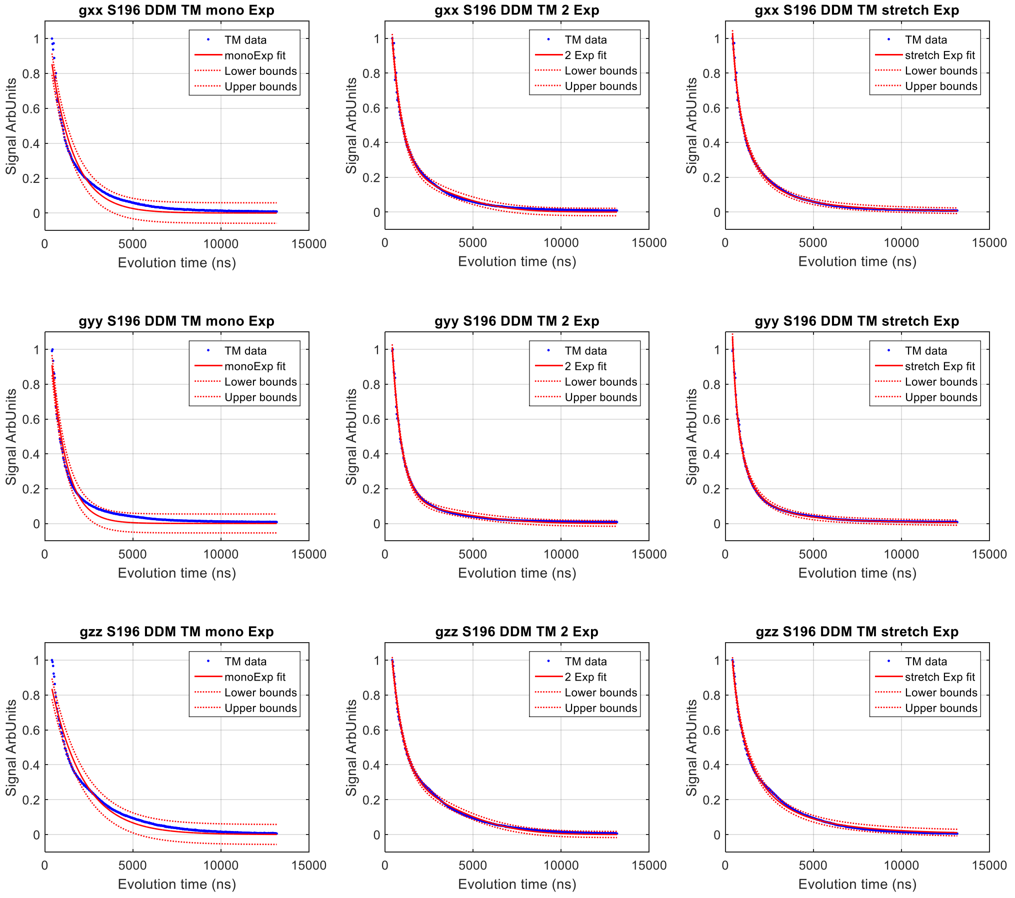

__Figure 7.2.2__ Plots of the fits shown in __Table 7.2.2__ shown in red overlaid on the experimental echo decay signals shown in blue. The light red lines surrounding the fit correspond to 95% confidence bounds of the fit.

D67 bicelle	**Tm with single Exp (1)**	**Tm with two Exp (2)**	**Tm with stretch Exp (3)**
gxx	τ=3046±27 ns AdjR²=0.9971	83±4% τ=2213±202 ns 17±4% τ=7160±294 ns AdjR²=0.9974	x=0.96±0.02 τ=2942±286 ns AdjR²=0.9972
gyy	τ=2235±33 ns AdjR²=0.9929	85±1% τ=1375±37 ns 15±1% τ=6681±152 ns AdjR²=0.9991	x=0.73±0.01 τ=1477±38 ns AdjR²=0.9991
gzz	τ=2802±24 ns AdjR²=0.9975	75±3% τ=1476±44 ns 25±3% τ=6333±74 ns AdjR²=0.9997	x=0.88±0.01 τ=2446±46 ns AdjR²=0.9987

Table 7.2.3 *Table of fits to phase memory time measurements of sample labelled at site D67 in bicelle. Each column corresponds to a different model in* ***Equation 7.2.1*** *as indicated. The model which has the most consistent good fits, as indicated by the Adjusted R-squared and discussion in the text, is highlighted in green. Rows correspond to the g-factor component which the echo sequence pulse excited.*

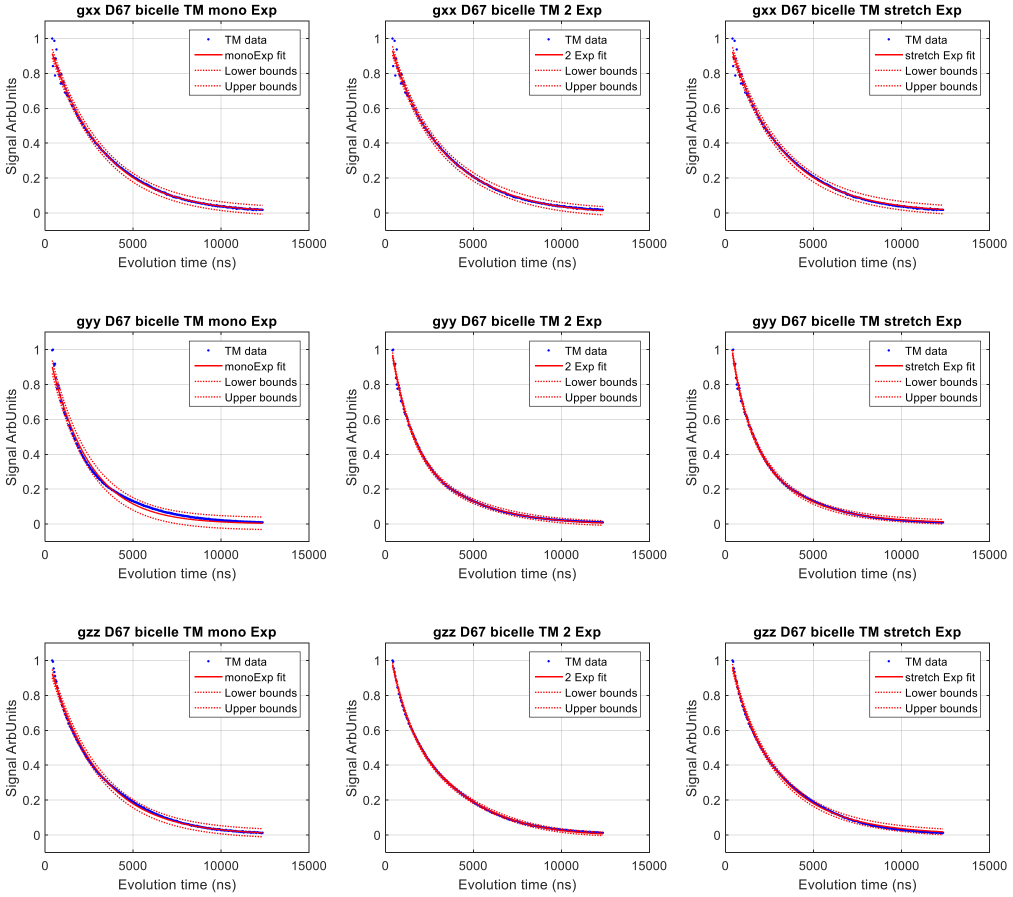

Figure 7.2.3 *Plots of the fits shown in* ***Table 7.2.3*** *shown in red overlaid on the experimental echo decay signals shown in blue. The light red lines surrounding the fit correspond to 95% confidence bounds of the fit.*

D67 DDM	**Tm with single Exp (1)**	**Tm with two Exp (2)**	**Tm with stretch Exp (3)**
gxx	τ=1792±17 ns AdjR^2=0.9970	90±2% τ=1379±78 ns 10±2% τ=5227±291 ns AdjR^2=0.9978	x=0.90±0.02 τ=1578±124 ns AdjR^2=0.9976
gyy	τ=1195±15 ns AdjR^2=0.9951	94±1% τ=943±20 ns 6±1% τ=5154±232 ns AdjR^2=0.9988	x=0.75±0.02 τ=787±39 ns AdjR^2=0.9979
gzz	τ=1750±14 ns AdjR^2=0.9980	84±1% τ=1125±15 ns 16±1% τ=4730±42 ns AdjR^2=0.9999	x=0.85±0.01 τ=1425±23 ns AdjR^2=0.9994

__Table 7.2.4__ Table of fits to phase memory time measurements of sample labelled at site D67 in DDM. Each column corresponds to a different model in __Equation 7.2.1__ as indicated. The model which has the most consistent good fits, as indicated by the Adjusted R-squared and discussion in the text, is highlighted in green. Rows correspond to the g-factor component which the echo sequence pulse excited.

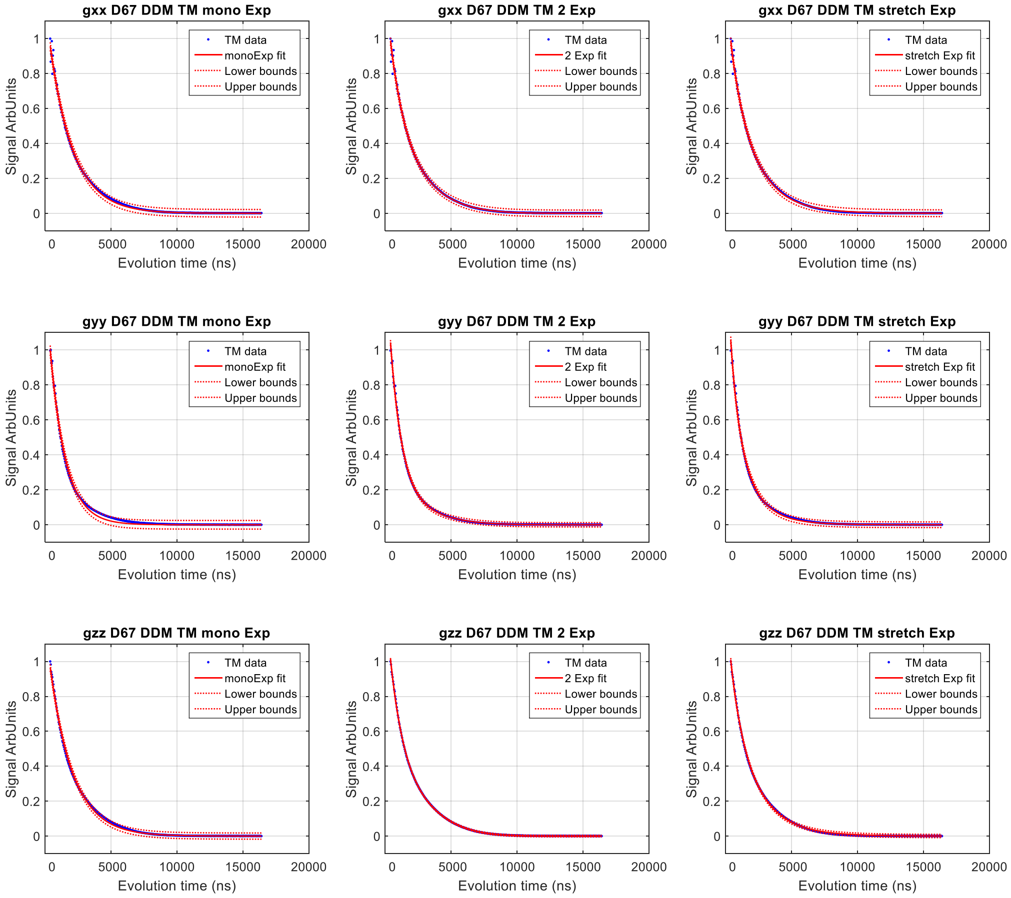

__Figure 7.2.4__ Plots of the fits shown in __Table 7.2.4__ shown in red overlaid on the experimental echo decay signals shown in blue. The light red lines surrounding the fit correspond to 95% confidence bounds of the fit.

The S196 site Hahn echo decays were best described by the two exponential model (2), which suggests that there are two dominating contributions to the spin echo dephasing, intra-molecule instantaneous diffusion with a relatively short decay constant and nuclear spin diffusion with a longer decay constant. The constants for model (2) have been highlighted in green. The D67 site is described well by all of the models, and under this circumstance it is best to analyse the decay with the simple mono exponential model (1) which has the least number of free variables.

The Hahn echo decays of the labelled S196 site are shown to be best described by a two exponential decay model for a mono-exponential and a stretched exponential with x=2. The contribution from the slow component with x=2 is characteristic of nuclear spin diffusion with all of these samples being in non-deuterated medium and proton spin diffusion being the normally dominant mechanism for nitroxide spin label measured at ~50 K in a proton rich environment. The contribution from the fast component has a field dependence on whether the gxx, gyy or gzz component of the anisotropic g-factor is excited by the pulses, with the gyy excitation having a larger proportion of the fast relaxing decay relative to gxx and gyy. This is often a characteristic of instantaneous diffusion, which has a dependence on the fractional excitation of the refocusing pulse in the echo sequence. Instantaneous diffusion is normally associated with the dipolar couplings between, inter-molecule, however, it is also possible for there to be a contribution of signal dephasing due to the spins local to the molecule, intra-molecule. This effect can be particularly strong when there are a larger number of spins in a given molecule increasing the local concentration. This effect will be discussed.

The mechanism of the instantaneous diffusion transverse relaxation is due to local field changes at the observed spin due to pulse induced flips of nearby dipolar coupled electron spins [117]. This makes it dependent on the local distribution of spins. There is a well-established expression for the normally considered case of homogenously distributed spins in three dimensions, which describes the distribution of molecules in a glassy matrix. The common form of this expression [13] is

$$\frac{1}{T_{ID}} = \frac{\pi}{9\sqrt{3}} \frac{\mu_0 g_1 g_2 {\mu_B}^2}{\hbar} c N_A \sin^2(\frac{\beta}{2})$$

Equation 7.2.2

where μ_0 is permeability of vacuum, g_1 and g_2 are the g-factors for the two electron spins, μ_B is the Bohr magneton, c is the molar concentration, N_A is Avogadro's constant and β is the flip angle of the refocussing pulse. At high magnetic field measurement of nitroxides the pulse excitation bandwidth will be smaller than the width of the spectrum, such that effective local concentration will be proportional to the pulse length for a fixed value of β and thus T_{ID} will be proportional to the pulse length for a fixed value of β. In the T_M measurements shown in **Table 7.2.1** - **Table 7.2.4** β was kept constant at π and the pulse length was constant for each given experiment, although the spectrum does not have constant spin density such that the local spin concentration will change as the excitation position changes, with a peak expected at the gyy position.

In these experiments the molecule concentration of the samples is 30μM or less, so we can expect the T_{ID} contribution from the molecule-to-molecule spins to have a decay constant much longer than the measure decay constant of the fast relaxation component. However, there are 7 spins per molecule over a range of <10 nm creating a locally high concentration of spins which can contribute to the phase memory time T_M with a decay constant in the regime of 10^2 ns, and may be contributing towards the fast relaxation. The contribution will depend on the number of spins excited in the molecule, which when ignoring orientation selection will be proportional to the fraction of the spectrum excited by the refocussing pulse. As the spins associated with a single molecule will have a defined set of distances and inter-spin vectors, which influence the dipolar coupling strength, the fraction of spins excited will influence the decay constant T_{ID} in a non-intuitive way, but the magnitude of the contribution should scale closely to the number of spins excited within the molecule.

To test for this localised intra-molecule instantaneous diffusion the relative ratios of the components are shown along with the ratio of the pulse excitation is shown in **Table 7.2.5**. The average of the S196 labelled site in DDM and bicelle was averaged as the effect should be independent of the local nuclear environment.

	Averaged ratio of fast relaxing component	**Ratio of spins excited by the π refocussing pulse**
gxx	93%	61%
gyy	100%	100%
gzz	86%	38%

Table 7.2.5 *Comparison table of the relative amounts of the fast relaxing component fitted with the decay model (2) to S196 echo decay measurements and the relative number of spins excited by the π pulse in each of the echo decay experiments.*

It is seen from the comparison of these ratios that although there is a correlation between the ratios of the spectrum excited by the refocussing pulse and the ratios of the fast relaxing decay component it is not a direct relation. The correlation does however suggest that there is a significant transverse instantaneous diffusion contribution from within the molecule, requiring further experiments to isolate the contribution from other transverse relaxation mechanisms influencing the phase memory time of the measured electron spins.

The labelled D67 site, as previously mentioned, could be expected to see a larger change in local environment between bicelle and DDM being in the transmembrane domain, whilst the S196 site will be more distant from the bicelle lipid layer and experience a smaller local environment change. The results agree with this hypothesis, little change is seen in the decay constants between the two environments for the S196 whilst a significant change is seen for the D67 site. However, the results suggest that the D67 has an increased decay constant for the bicelle environment against the DDM by a factor of ~2, which is against what is typically reported. Further experiment and analysis separating different relaxation mechanisms are required to comment on what the reason for this increase in the echo decay constant in the bicelle. It is also noted for the labelled site D67 that the decay is well characterised by the mono-exponential, model (1), and the stretched exponential, model (3), also shows fits where x≈1. It is not clear what the dominating decay mechanism observed at the D67 labelled site is, mechanisms where x=1 include instantaneous diffusion, rapid methyl spin rotation or fast libration motion. Again a comprehensive relaxation study, which resource did not permit during this project, is required to disentangle the underlying mechanisms.

7.3. CONCLUSIONS

In this work a model suitable for analysis and fitting PELDOR signals to cyclically symmetric oligomers is presented. By using orientation selective PELDOR signal simulation code with the models and analysis methodology is suggested and tested with several simulated example models.

An investigation into the spin labelled channel protein MscS was made looking at three MTSSL labelled sites between the transmembrane region and cytoplasm region, at residue sites D67, L124 and S196. Spin label conformation rotamer prediction and CW signal analysis of these sites revealed that the labelled site L124 was predicted to be rigid with respect to the underlying protein and the CW analysis agrees with this. The labelled site S196 was predicted by the rotamer modelling to have a rigid conformation, however CW analysis suggested that there was a more flexible conformation, or that the underlying secondary structure was more disordered. The D67 site was predicted to have a large conformational range, and the CW analysis gave broad agreement, although the line-shape suggested a more complex label motion. The S196 and L124 sites were selected for orientation PELDOR measurement and application of the presented algorithm.

Complications in the measured PELDOR signals, with modulation depths in poor agreement with the full ranges of simulated values, and a PELDOR signal dependence on the pulse timings used in the PELDOR sequence suggests that the orientation selective PELDOR signal may not be analysed using the simple signal approximation. Previously published results show a dependence of the signal modulation depth on the pulse times, however, in the experiments made on the S196 site of MscS the modulation depths would remain constant, but the amplitude of the modulating oscillations would vary. A suggested mechanism is intra-molecule relaxation resulting in a differential relaxation depending on the number of spins excited in each molecule, complicated by some sites having possible rigid relative orientations.

A study was made to measure phase memory times for the labelled sites S196 and D67 and fitted to relaxation models of, proton spin diffusion, instantaneous diffusion and proton spin diffusion and a stretched exponential.

It was observed that the D67 labelled site had a relaxation best fitted to a stretched exponential corresponding to a non-obvious, faster than proton spin diffusion mechanism. The S196 fitted well to a mixture of fast instantaneous diffusion and slower proton flip-flop spin diffusion mechanism, and although there was a correlation between the fraction of the total spectrum excited by the spin echo pulses and the fraction of the fast instantaneous diffusion component, it was not a direct relationship. This suggests that the relaxation mechanisms of spin echo in the MscS membrane protein is field dependent, in either detergent or model membrane, is not dominated by proton spin diffusion, and it is possible that this could influence the measured echo modulated PELDOR experiments.

These measurements suggest that although there is evidence of orientation dependence of the PELDOR signals measured for the protein MscS, it is not immediately possible to use these in analysis to derive orientation information which could be used in structure refinements. This is due to multiple observed effects: the modulation depths deviate to being less than what is expected based on simulations and the PELDOR signal modulations have a dependence on the total spin echo evolution time of the experiment. These observations may in part be due to differential relaxation of different molecules contributing to the PELDOR signal, evidenced by the observed significant intra-molecule instantaneous diffusion relaxation mechanism which could cause different molecules to relax at different rates depending on the number of spins excited and modifying the measured PELDOR signal. However, this was not the dominant relaxation mechanism measured at all labelled sites of the molecule and the modulation depths were observed in some cases to be independent of pulse sequence timing. There is potential to reduce the contribution of the intra-molecule instantaneous diffusion by reducing the number of spins excited by the observer pulses in the sequence, reducing the number of spins contributing to the measured echo and thus instantaneous diffusion. Although the pulses must still have enough bandwidth to excite the dipolar splitting, such that placing the pulse excitations at the edge of the spectrum with short pulse lengths may be optimal. It will also be of great benefit to reduce the spin labelling efficiency such that the number of spins per molecule will decrease, reducing both the intra molecule instantaneous diffusion and multiple spin effects contributing to the PELDOR signal. This will, however, reduce the number of spins contributing to the signal and require high sensitivity spectrometers, suggesting that these measurements are best performed using high power high magnetic field spectrometers which have increased sensitivity to make the measurements.

Chapter 8 CONCLUSION

This thesis explored the use of the novel HiPER spectrometer for orientation selective PELDOR experiments. To achieve this aim the work has developed through, the investigation and characterisation of the HiPER W-band spectrometer, development of suitable PELDOR signal simulation code, a study of the applicability of the Rx spin label using orientation selective PELDOR and a study into measuring oligomeric membrane protein using W-band PELDOR spectroscopy.

The investigation and characterisation of the HiPER W-band spectrometer showed that the high power bandwidth of the spectrometer is 700 MHz, and that the limitation on the bandwidth originates from the high-power amplifier stage. The other components active stages in the spectrometer are measured to have bandwidths in excess of this and the transmission optics and waveguide also exceed this bandwidth. The high-power EIK amplifier is specified to have a bandwidth of around 1 GHz and a suggested mechanism for limiting the bandwidth is the required input power to achieve saturated output power of the amplifier is likely to vary across the bandwidth, whilst a fixed input optimized for the centre frequency of 94 GHz is used in the spectrometer. It is in the current configuration very difficult to vary the input power to the amplifier in the spectrometers current configuration but with use of arbitrary waveform generators this may become possible. For the applications presented in this thesis of PELDOR experiments using nitroxide spin labels the bandwidth is required to be at least equal to the spectral width of ~400 MHz, which is the case. A calibration of the effective microwave magnetic field amplitude was made as a function of frequency to be used with PELDOR signal simulations. Pulse EPR experiments utilising this full bandwidth revealed that anomalous results were sometimes observed when using quartz EPR sample tubes and that these were consistent with the existence of resonances related to the sample and its container. Simulations of the microwave fields propagating inside the sample holder choosing the sample tube material to be quartz indicated that the tube is likely to excite field modes which can only propagate inside the tube region, creating trapped mode resonances. These simulations were consistent with the resonances observed on the spectrometer. A solution to the problem is to use a tube made from a lower dielectric constant material. One such material from which suitable tube can be manufactured, and is readily available, is FEP. Simulations of the fields in the same sample holder but with the FEP tubes showed a drastic reduction in the tube exciting higher order field modes, and a reduction in resonances. These tubes have now become the standard sample container for use with the HiPER spectrometer.

The analysis of PELDOR signals requires the fitting of these signals to a model, and a signal simulation code was written to enable this. The code was written in a general way such that study specific models could be integrated. The main bottleneck in fitting a model to PELDOR signals is the computation time required to calculate the signals and effort was made to reduce this by writing the code using large multidimensional matrix operations.

A study was made to investigate the suitability and application of the bifunctional Rx nitroxide spin label for orientation selective PELDOR experiments. The study was conducted using the dimer Vps75 as a framework, investigating labelling sites on both α-helix and β-sheet secondary structure. It was observed through MD simulations that the labelling sites on the α-helix which had residue sites next to each other, residue i to residue i+1, had the most suitable mono-modal conformation distributions and the most generally predictable secondary structure attachment positions. These sites were selected for the orientation selective PELDOR measurements. The analysis of these PELDOR signals showed conformations which were in good general agreement with the MD simulations, and a comparison was made to investigate differences. It was shown that by calculating the relative angles between vectors of the spin label it is possible to implement the PELDOR results as XANG constraints in the XPLOR-NIH package. It is highlighted that this only partially utilises the experiment results and further development is still required in integration of these restraints in structure refinement packages. The Rx label is presented as a good candidate for orientation PELDOR studies when attached to the α-helix using adjacent residues.

The application of orientation PELDOR for oligomeric proteins was investigated using the membrane channel protein MscS. A general model is presented which assumes cyclic symmetry and a spin label which is rigid to the underlying structure. This model is suitable for using the general PELDOR simulation code and an analysis methodology is presented based on a data reduction algorithm and fitting. The algorithm is tested with several simulated example models. One case is a cone distribution and the other is the rotation of a rigid spin label by 90 degrees and observing that the results closely match the input simulation model. To experimentally test the methodology several spin labelling residue sites on the protein MscS are investigated by spin label rotamer prediction software and CW lineshape analysis. The site S196 and L124 were selected for orientation selective PELDOR measurements, however the results showed complications in the measured PELDOR signals, with modulation depths in poor agreement with the full ranges of simulated values, and a PELDOR signal dependence on the pulse timings used in the PELDOR sequence suggests that the orientation selective PELDOR signal may not be analysed using the simple signal approximation. A suggested complication to the PELDOR signal analysis may be differential relaxation depending on the number of spins excited in the cluster. A study was made to measure phase memory times for the labelled sites S196 and D67 and fitted to relaxation models of, proton spin diffusion, instantaneous diffusion and proton spin diffusion and a stretched exponential. It was shown that echo decays in either the D67 site in the transmembrane region of the protein or the S196 site in the cytoplasmic region were dominated by proton spin diffusion. The D67 site fitted to a model with a relaxation mechanism faster than proton spin diffusion but not described well by instantaneous diffusion. The S196 site fitted to two dominating mechanisms with different timescales, a fast instantaneous diffusion mechanism and a slower proton spin diffusion. With a more thorough understanding of the PELDOR signals, the presented analysis techniques are promising for fitting and analysis of orientation constrained spin labels in large oligomeric proteins to obtain accurate distance constraints.

BIBLIOGRAPHY

1. Berg, J.M., et al., *Biochemistry*. 2015: W. H. Freeman.
2. Reginsson, Gunnar W. and O. Schiemann, *Pulsed electron–electron double resonance: beyond nanometre distance measurements on biomacromolecules*. Biochemical Journal, 2011. **434**(3): p. 353-363.
3. Hagelueken, G., et al., *PELDOR Spectroscopy Distance Fingerprinting of the Octameric Outer-Membrane Protein Wza from Escherichia coli*. Angewandte Chemie International Edition, 2009. **48**(16): p. 2904-2906.
4. Moraes, I., et al., *Membrane protein structure determination — The next generation*. Biochimica et Biophysica Acta (BBA) - Biomembranes, 2014. **1838**(1, Part A): p. 78-87.
5. *Chapter 2 Principles and Illustrative Examples of High-Field/High-Frequency EPR*, in *High-Field EPR Spectroscopy on Proteins and their Model Systems: Characterization of Transient Paramagnetic States*. 2009, The Royal Society of Chemistry. p. 23-123.
6. Reijerse, E., *High-Frequency EPR Instrumentation*. Applied Magnetic Resonance, 2010. **37**(1-4): p. 795-818.
7. Hubbell, W.L., et al., *Technological advances in site-directed spin labeling of proteins*. Current Opinion in Structural Biology, 2013. **23**(5): p. 725-733.
8. Cruickshank, P.A.S., et al., *A kilowatt pulsed 94 GHz electron paramagnetic resonance spectrometer with high concentration sensitivity, high instantaneous bandwidth, and low dead time*. Review of Scientific Instruments, 2009. **80**(10): p. 103102.
9. Salikhov, K.M., S.A. Dzuba, and A.M. Raitsimring, *The Theory of Electron Spin-Echo Signal Decay Resulting from Dipole-Dipole Interactions between Paramagnetic Centers in Solids*. Journal of Magnetic Resonance, 1981. **42**(2): p. 255-276.
10. Milov, A.D., A.B. Ponomarev, and Y.D. Tsvetkov, *Electron Electron Double-Resonance in Electron-Spin Echo - Model Biradical Systems and the Sensitized Photolysis of Decalin*. Chemical Physics Letters, 1984. **110**(1): p. 67-72.
11. Pannier, M., et al., *Dead-time free measurement of dipole-dipole interactions between electron spins*. Journal of Magnetic Resonance, 2000. **142**(2): p. 331-340.
12. Jeschke, G. and Y. Polyhach, *Distance measurements on spin-labelled biomacromolecules by pulsed electron paramagnetic resonance*. Physical Chemistry Chemical Physics, 2007. **9**(16): p. 1895-1910.
13. Schweiger, A. and G. Jeschke, *Principles of pulse electron paramagnetic resonance*. 2001, Oxford [u.a.]: Oxford Univ. Press.
14. Larsen, R.G. and D.J. Singel, *Double Electron-Electron Resonance Spin-Echo Modulation - Spectroscopic Measurement of Electron-Spin Pair Separations in Orientationally Disordered Solids*. Journal of Chemical Physics, 1993. **98**(7): p. 5134-5146.
15. Godt, A., et al., *EPR probes with well-defined, long distances between two or three unpaired electrons*. Journal of Organic Chemistry, 2000. **65**(22): p. 7575-7582.

16. Margraf, D., et al., *Conformational flexibility of nitroxide biradicals determined by X-band PELDOR experiments.* Molecular Physics, 2007. **105**(15-16): p. 2153-2160.
17. Marko, A. and T.F. Prisner, *An algorithm to analyze PELDOR data of rigid spin label pairs.* Phys Chem Chem Phys, 2013. **15**(2): p. 619-27.
18. Abdullin, D., et al., *Geometric model-based fitting algorithm for orientation-selective PELDOR data.* Molecular Physics, 2014. **113**(6): p. 544-560.
19. Altenbach, C., et al., *Transmembrane protein structure: spin labeling of bacteriorhodopsin mutants.* Science, 1990. **248**(4959): p. 1088-92.
20. Berliner, L.J., et al., *A novel reversible thiol-specific spin label: papain active site labeling and inhibition.* Anal Biochem, 1982. **119**(2): p. 450-5.
21. Klare, J.P. and H.-J. Steinhoff, *Spin labeling EPR.* Photosynthesis Research, 2009. **102**(2-3): p. 377-390.
22. Bordignon, E., *Site-Directed Spin Labeling of Membrane Proteins.* Epr Spectroscopy: Applications in Chemistry and Biology, 2012. **321**: p. 121-157.
23. Fanucci, G.E. and D.S. Cafiso, *Recent advances and applications of site-directed spin labeling.* Current Opinion in Structural Biology, 2006. **16**(5): p. 644-653.
24. Ward, R., et al., *EPR distance measurements in deuterated proteins.* Journal of magnetic resonance (San Diego, Calif. : 1997), 2010. **207**(1): p. 164-7.
25. El Mkami, H., et al., *The spatial effect of protein deuteration on nitroxide spin-label relaxation: Implications for EPR distance measurement.* Journal of Magnetic Resonance, 2014. **248**: p. 36-41.
26. Kuzhelev, A.A., et al., *Room-Temperature Electron Spin Relaxation of Triarylmethyl Radicals at the X- and Q-Bands.* The Journal of Physical Chemistry B, 2015.
27. Savitsky, A., et al., *Bacterial Photosynthetic Reaction Centers in Trehalose Glasses: Coupling between Protein Conformational Dynamics and Electron-Transfer Kinetics as Studied by Laser-Flash and High-Field EPR Spectroscopies.* Journal of Physical Chemistry B, 2010. **114**(39): p. 12729-12743.
28. Corradini, D., et al., *Microscopic mechanism of protein cryopreservation in an aqueous solution with trehalose.* Scientific Reports, 2013. **3**.
29. Meyer, V., et al., *Room-Temperature Distance Measurements of Immobilized Spin-Labeled Protein by DEER/PELDOR.* Biophysical Journal, 2015. **108**(5): p. 1213-1219.
30. Yang, Z., et al., *Pulsed ESR Dipolar Spectroscopy for Distance Measurements in Immobilized Spin Labeled Proteins in Liquid Solution.* Journal of the American Chemical Society, 2012. **134**(24): p. 9950-9952.
31. Fleissner, M.R., et al., *Site-directed spin labeling of a genetically encoded unnatural amino acid.* Proceedings of the National Academy of Sciences of the United States of America, 2009. **106**(51): p. 21637-21642.
32. Kalai, T., et al., *Synthesis of new spin labels for Cu-free click conjugation.* Tetrahedron Letters, 2011. **52**(21): p. 2747-2749.
33. Evans, E.G.B. and G.L. Millhauser, *Genetic Incorporation of the Unnatural Amino Acid p-Acetyl Phenylalanine into Proteins for Site-Directed Spin Labeling*, in *Methods in Enzymology.* Academic Press.

34. Stoller, S., et al., *TOPP: A Novel Nitroxide-Labeled Amino Acid for EPR Distance Measurements.* Angewandte Chemie-International Edition, 2011. **50**(41): p. 9743-9746.
35. Goldfarb, D., *Gd3+ spin labeling for distance measurements by pulse EPR spectroscopy.* Physical Chemistry Chemical Physics, 2014. **16**(21): p. 9685-9699.
36. Martorana, A., et al., *Probing Protein Conformation in Cells by EPR Distance Measurements using Gd3+ Spin Labeling.* Journal of the American Chemical Society, 2014. **136**(38): p. 13458-13465.
37. Igarashi, R., et al., *Distance Determination in Proteins inside Xenopus laevis Oocytes by Double Electron-Electron Resonance Experiments.* Journal of the American Chemical Society, 2010. **132**(24): p. 8228-+.
38. Krstic, I., et al., *Long-Range Distance Measurements on Nucleic Acids in Cells by Pulsed EPR Spectroscopy.* Angewandte Chemie-International Edition, 2011. **50**(22): p. 5070-5074.
39. Azarkh, M., et al., *Intracellular Conformations of Human Telomeric Quadruplexes Studied by Electron Paramagnetic Resonance Spectroscopy.* Chemphyschem, 2012. **13**(6): p. 1444-1447.
40. Holder, I.T., M. Drescher, and J.S. Hartig, *Structural characterization of quadruplex DNA with in-cell EPR approaches.* Bioorganic & Medicinal Chemistry, 2013. **21**(20): p. 6156-6161.
41. Höbartner, C., et al., *Synthesis and Characterization of RNA Containing a Rigid and Nonperturbing Cytidine-Derived Spin Label.* The Journal of Organic Chemistry, 2012. **77**(17): p. 7749-7754.
42. Toledo Warshaviak, D., et al., *Structure and dynamics of an imidazoline nitroxide side chain with strongly hindered internal motion in proteins.* Journal of Magnetic Resonance, 2013. **232**: p. 53-61.
43. Fleissner, M.R., et al., *Structure and dynamics of a conformationally constrained nitroxide side chain and applications in EPR spectroscopy.* Proceedings of the National Academy of Sciences of the United States of America, 2011. **108**(39): p. 16241-16246.
44. *Chapter 3 Instrumentation*, in *High-Field EPR Spectroscopy on Proteins and their Model Systems: Characterization of Transient Paramagnetic States*. 2009, The Royal Society of Chemistry. p. 124-194.
45. Tkach, I., et al., *A dual-mode microwave resonator for double electron–electron spin resonance spectroscopy at W-band microwave frequencies.* Journal of Magnetic Resonance, 2011. **209**(2): p. 341-346.
46. Dubinskii, A.A., et al., *Submicrosecond field-jump device for pulsed high-field ELDOR.* Applied Magnetic Resonance, 2002. **22**(3): p. 369-386.
47. Gromov, I., et al., *Novel MM-Wave EPR Spectrometer ELEXSYS 7th Series: Design and Performance.*
48. Abé, C., et al., *Orientation selective DEER measurements on vinculin tail at X-band frequencies reveal spin label orientations.* Journal of Magnetic Resonance, 2012. **216**: p. 53-61.

49. Schnegg, A., et al., *High-field EPR, ENDOR and ELDOR on bacterial photosynthetic reaction centers.* Applied Magnetic Resonance, 2007. **31**(1-2): p. 59-98.
50. Denysenkov, V.P., et al., *High-frequency 180 GHz PELDOR.* Applied Magnetic Resonance, 2005. **29**(2): p. 375-384.
51. Hertel, M.M., et al., *Pulsed 180-GHz EPR/ENDOR/PELDOR spectroscopy.* Magnetic Resonance in Chemistry, 2005. **43**: p. S248-S255.
52. Reginsson, G.W., et al., *W-band PELDOR with 1 kW microwave power: Molecular geometry, flexibility and exchange coupling.* Journal of Magnetic Resonance, 2012. **216**: p. 175-182.
53. Tkach, I., et al., *High-frequency 263 GHz PELDOR.* Applied Magnetic Resonance, 2014. **45**(10): p. 969-979.
54. Giannoulis, A., et al., *PELDOR in rotationally symmetric homo-oligomers.* Molecular Physics, 2013. **111**(18-19): p. 2845-2854.
55. Bode, B.E., et al., *Counting the monomers in nanometer-sized oligomers by pulsed electron - Electron double resonance.* Journal of the American Chemical Society, 2007. **129**(21): p. 6736-6745.
56. Jeschke, G., et al., *Three-spin correlations in double electron-electron resonance.* Physical Chemistry Chemical Physics, 2009. **11**(31): p. 6580-6591.
57. Polyhach, Y., et al., *Spin pair geometry revealed by high-field DEER in the presence of conformational distributions.* Journal of Magnetic Resonance, 2007. **185**(1): p. 118-129.
58. Hilger, D., et al., *Assessing Oligomerization of Membrane Proteins by Four-Pulse DEER: pH-Dependent Dimerization of NhaA Na+/H+ Antiporter of E. coli.* Biophysical Journal, 2005. **89**(2): p. 1328-1338.
59. Edwards, Devin T., et al., *Determining the Oligomeric Structure of Proteorhodopsin by Gd3+-Based Pulsed Dipolar Spectroscopy of Multiple Distances.* Structure, 2014. **22**(11): p. 1677-1686.
60. Pliotas, C., et al., *Conformational state of the MscS mechanosensitive channel in solution revealed by pulsed electron–electron double resonance (PELDOR) spectroscopy.* Proceedings of the National Academy of Sciences, 2012. **109**(40): p. E2675-E2682.
61. Junk, M.J.N., H.W. Spiess, and D. Hinderberger, *The Distribution of Fatty Acids Reveals the Functional Structure of Human Serum Albumin.* Angewandte Chemie International Edition, 2010. **49**(46): p. 8755-8759.
62. Sahu, I.D., et al., *DEER EPR Measurements for Membrane Protein Structures via Bifunctional Spin Labels and Lipodisq Nanoparticles.* Biochemistry, 2013. **52**(38): p. 6627-6632.
63. von Hagens, T., et al., *Suppression of ghost distances in multiple-spin double electron-electron resonance.* Physical Chemistry Chemical Physics, 2013. **15**(16): p. 5854-5866.
64. Junk, M.J.N., H.W. Spiess, and D. Hinderberger, *DEER in biological multispin-systems: A case study on the fatty acid binding to human serum albumin.* Journal of Magnetic Resonance, 2011. **210**(2): p. 210-217.

65. Ward, R., et al., *Probing the Structure of the Mechanosensitive Channel of Small Conductance in Lipid Bilayers with Pulsed Electron-Electron Double Resonance.* Biophysical Journal, 2014. **106**(4): p. 834-842.
66. Pliotas, C., et al., *Conformational state of the MscS mechanosensitive channel in solution revealed by pulsed electron-electron double resonance (PELDOR) spectroscopy.* Proceedings of the National Academy of Sciences of the United States of America, 2012. **109**(40): p. E2675-E2682.
67. Weil, J.A. and J.R. Bolton, *Electron Paramagnetic Resonance: Elementary Theory and Practical Applications*. 2007: Wiley.
68. Poole, C.P., *Electron Spin Resonance: A Comprehensive Treatise on Experimental Techniques*. 1996: Dover Publications.
69. Levitt, M.H., *Spin Dynamics: Basics of Nuclear Magnetic Resonance*. 2013: Wiley.
70. Kulik, L.V., et al., *Electron dipole–dipole interaction in ESEEM of nitroxide biradicals.* Chemical Physics Letters, 2001. **343**(3–4): p. 315-324.
71. Kurshev, V.V., A.M. Raitsimring, and Y.D. Tsvetkov, *Selection of Dipolar Interaction by the 2+1 Pulse Train Ese.* Journal of Magnetic Resonance, 1989. **81**(3): p. 441-454.
72. Borbat, P.P. and J.H. Freed, *Multiple-quantum ESR and distance measurements.* Chemical Physics Letters, 1999. **313**(1–2): p. 145-154.
73. Milov, A.D., K.M. Salikhov, and M.D. Shirov, *Application of Eldor in Electron-Spin Echo for Paramagnetic Center Space Distribution in Solids.* Fizika Tverdogo Tela, 1981. **23**(4): p. 975-982.
74. Salikhov, K.M. and I.T. Khairuzhdinov, *Four-Pulse ELDOR Theory of the Spin A1/2 Label Pairs Extended to Overlapping EPR Spectra and to Overlapping Pump and Observer Excitation Bands.* Applied Magnetic Resonance, 2015. **46**(1): p. 67-83.
75. Salikhov, K.M., I.T. Khairuzhdinov, and R.B. Zaripov, *Three-Pulse ELDOR Theory Revisited.* Applied Magnetic Resonance, 2014. **45**(6): p. 573-619.
76. Nevzorov, A.A. and J.H. Freed, *A many-body analysis of the effects of the matrix protons and their diffusional motion on electron spin resonance line shapes and electron spin echoes.* The Journal of Chemical Physics, 2001. **115**(6): p. 2416-2429.
77. Jeschke, G., et al., *DeerAnalysis2006 - a comprehensive software package for analyzing pulsed ELDOR data.* Applied Magnetic Resonance, 2006. **30**(3-4): p. 473-498.
78. Tikhonov, A.N. and V.B. Glasko, *Use of the regularization method in non-linear problems.* USSR Computational Mathematics and Mathematical Physics, 1965. **5**(3): p. 93-107.
79. Hansen, P.C., *The L-curve and its use in the numerical treatment of inverse problems.* Computational Inverse Problems in Electrocardiography, 2001. **5**: p. 119-142.
80. Jeschke, G. and H.W. Spiess, *Distance Measurements in Solid-State NMR and EPR Spectroscopy*, in *Novel NMR and EPR techniques*, J. Dolinšek, M. Vilfan, and S. Žumer, Editors. 2006, Springer Berlin Heidelberg. p. 21-63.
81. Jeschke, G., R. Rakhmatullin, and A. Schweiger, *Sensitivity Enhancement by Matched Microwave Pulses in One- and Two-Dimensional Electron Spin Echo Envelope*

Modulation Spectroscopy. Journal of Magnetic Resonance, 1998. **131**(2): p. 261-271.
82. Doll, A., et al., *Adiabatic and fast passage ultra-wideband inversion in pulsed EPR*. Journal of Magnetic Resonance, 2013. **230**: p. 27-39.
83. Schops, P., et al., *Broadband spin echoes and broadband SIFTER in EPR*. J Magn Reson, 2015. **250**: p. 55-62.
84. Lamb, J., *Miscellaneous data on materials for millimetre and submillimetre optics*. International Journal of Infrared and Millimeter Waves, 1996. **17**(12): p. 1997-2034.
85. Kraus, J.D. and D.A. Fleisch, *Electromagnetics: With Applications*. 1999: WCB/McGraw-Hill.
86. Chao, A. and M. Tigner, *Handbook of Accelerator Physics and Engineering*. 1999: World Scientific.
87. Wowk, B., *Thermodynamic aspects of vitrification*. Cryobiology, 2010. **60**(1): p. 11-22.
88. Hogben, H.J., et al., *Spinach – A software library for simulation of spin dynamics in large spin systems*. Journal of Magnetic Resonance, 2011. **208**(2): p. 179-194.
89. Marko, A., et al., *Molecular orientation studies by pulsed electron-electron double resonance experiments*. The Journal of Chemical Physics, 2009. **130**(6): p. 064102.
90. Kunjir, N.C., et al., *Measurements of short distances between trityl spin labels with CW EPR, DQC and PELDOR*. Phys Chem Chem Phys, 2013. **15**(45): p. 19673-85.
91. Fuller, J., *Function to Convert between DCM, Euler angles, Quaternions, and Euler vectors - File Exchange - MATLAB Central*. Matlab Central, 2015.
92. Yuval and J. Tursa, *MMX - Multithreaded matrix operations on N-D matrices - File Exchange - MATLAB Central*. Matlab Central, 2015.
93. Schwieters, C.D., et al., *The Xplor-NIH NMR molecular structure determination package*. Journal of Magnetic Resonance, 2003. **160**(1): p. 65-73.
94. Binder, B.P., et al., *High-resolution helix orientation in actin-bound myosin determined with a bifunctional spin label*. Proceedings of the National Academy of Sciences, 2015. **112**(26): p. 7972-7977.
95. Moen, R.J., D.D. Thomas, and J.C. Klein, *Conformationally Trapping the Actin-binding Cleft of Myosin with a Bifunctional Spin Label*. Journal of Biological Chemistry, 2013. **288**(5): p. 3016-3024.
96. Rayes, R.F., et al., *Dynamics of Tropomyosin in Muscle Fibers as Monitored by Saturation Transfer EPR of Bi-Functional Probe*. Plos One, 2011. **6**(6).
97. Bowman, A., et al., *The histone chaperones Vps75 and Nap1 form ring-like, tetrameric structures in solution*. Nucleic Acids Research, 2014. **42**(9): p. 6038-6051.
98. Lillington, J.E.D., et al., *Shigella flexneri Spa15 Crystal Structure Verified in Solution by Double Electron Electron Resonance*. Journal of Molecular Biology, 2011. **405**(2): p. 427-435.
99. Lovett, J.E., et al., *Structural information from orientationally selective DEER spectroscopy*. Physical Chemistry Chemical Physics, 2009. **11**(31): p. 6840-6848.

100. Endeward, B., et al., *Pulsed Electron-Electron Double Resonance Determination of Spin Label Distances and Orientations on the Tetrameric Potassium Ion Channel KcsA.* Journal of the American Chemical Society, 2009. **131**(42): p. 15246-15250.
101. Stoll, S. and A. Schweiger, *EasySpin, a comprehensive software package for spectral simulation and analysis in EPR.* Journal of Magnetic Resonance, 2006. **178**(1): p. 42-55.
102. Bak, M. and N.C. Nielsen, *REPULSION, A Novel Approach to Efficient Powder Averaging in Solid-State NMR.* Journal of Magnetic Resonance, 1997. **125**(1): p. 132-139.
103. Zaremba, S.K., *Good lattice points, discrepancy, and numerical integration.* Annali di Matematica Pura ed Applicata, 1966. **73**(1): p. 293-317.
104. Cheng, V.B., H.H. Suzukawa, and M. Wolfsberg, *Investigations of a nonrandom numerical method for multidimensional integration.* The Journal of Chemical Physics, 1973. **59**(8): p. 3992-3999.
105. Conroy, H., *Molecular Schrödinger Equation. VIII. A New Method for the Evaluation of Multidimensional Integrals.* The Journal of Chemical Physics, 1967. **47**(12): p. 5307-5318.
106. Godt, A., et al., *How flexible are poly(para-phenyleneethynylene)s?* Angewandte Chemie-International Edition, 2006. **45**(45): p. 7560-7564.
107. Levy, E.D., et al., *3D Complex: A Structural Classification of Protein Complexes.* PLoS Comput Biol, 2006. **2**(11): p. e155.
108. Berman, H.M., et al., *The Protein Data Bank.* Nucleic Acids Research, 2000. **28**(1): p. 235-242.
109. Hagberg, G., *From magnetic resonance spectroscopy to classification of tumors. A review of pattern recognition methods.* NMR in Biomedicine, 1998. **11**(4-5): p. 148-156.
110. Hasegawa, T., J. Nishijo, and J. Umemura, *Separation of Raman spectra from fluorescence emission background by principal component analysis.* Chemical Physics Letters, 2000. **317**(6): p. 642-646.
111. Martin, F.L., et al., *Identifying Variables Responsible for Clustering in Discriminant Analysis of Data from Infrared Microspectroscopy of a Biological Sample.* Journal of Computational Biology, 2007. **14**(9): p. 1176-1184.
112. Freed, J.H., *Theory of Slow Tumbling ESR Spectra for Nitroxides*, in *Spin Labeling: Theory and Applications*. 1979, Academic Press. p. 53-132.
113. Budil, D.E., et al., *Nonlinear-Least-Squares Analysis of Slow-Motion EPR Spectra in One and Two Dimensions Using a Modified Levenberg–Marquardt Algorithm.* Journal of Magnetic Resonance, Series A, 1996. **120**(2): p. 155-189.
114. Polyhach, Y., E. Bordignon, and G. Jeschke, *Rotamer libraries of spin labelled cysteines for protein studies.* Physical Chemistry Chemical Physics, 2011. **13**(6): p. 2356-2366.
115. Hagelueken, G., et al., *MtsslWizard: In Silico Spin-Labeling and Generation of Distance Distributions in PyMOL.* Applied Magnetic Resonance, 2012. **42**(3): p. 377-391.
116. Eaton, S. and G. Eaton, *Relaxation Times of Organic Radicals and Transition Metal Ions*, in *Distance Measurements in Biological Systems by EPR*, L. Berliner, G. Eaton, and S. Eaton, Editors. 2002, Springer US. p. 29-154.

117. Klauder, J.R. and P.W. Anderson, *Spectral Diffusion Decay in Spin Resonance Experiments*. Physical Review, 1962. **125**(3): p. 912-932.
118. Jeschke, G., et al., *Dipolar spectroscopy and spin alignment in electron paramagnetic resonance*. Chemical Physics Letters, 2000. **331**(2-4): p. 243-252.

1. APPENDIX

1.1. HIGH PERFORMANCE FEEDHORNS FOR QUASI-OPTICAL DEVICES

During the course of my PhD I have been involved in several projects on millimetre wave instrumentation. One particular highlight is a project on antenna systems suitable for millimetre wave systems, such as satellites or radar, along with quasi optics used in many EPR instrumentation. Although I have chosen not to include this project as a chapter I have included two first author articles (reproduced under terms allowed by the publisher) I have written and details of patent applications which are pending.

The following articles were written with this author, who contributed significant novel research to their content. A further article is currently in progress to detail the design of an optimized algorithm for generating 'smooth-wall spline feedhorns'.

1.1.1. PREPARED PUBLICATIONS

McKay, J.E.; Robertson, D.A.; Cruickshank, P.A.S.; Hunter, R.I.; Bolton, D.R.; Wylde, R.J.; Smith, G.M., "Compact Wideband Corrugated Feedhorns With Ultra-Low Sidelobes for Very High Performance Antennas and Quasi-Optical Systems," in *Antennas and Propagation, IEEE Transactions on* , vol.61, no.4, pp.1714-1721, April 2013

URL: http://dx.doi.org/10.1109/TAP.2013.2243097

McKay, J.E.; Robertson, D.A.; Speirs, P.J.S..; Hunter, R.I.; Wylde, R.J.; Smith, G.M., " Compact corrugated feedhorns with high Gaussian coupling efficiency and ultra-low sidelobes," in Antennas and Propagation, IEEE Transactions on , Under review June 2015

1.1.2. PATENT APPLICATIONS

Two patent applications have been submitted to protect the intellectual property of the innovative design which was developed. These are filed with the EU and USA, details of these applications are presented here.

1.1.2.1. European patent application:

“Compact corrugated feedhorn”

Publication number	EP2779310 A1
Application number	EP20130158944
Filing date	13 Mar 2013
Inventors	Graham Smith, Johannes McKay
Applicant	University Court of The University of St Andrews

1.1.2.2. US patent application:

“Compact corrugated feedhorn”

Publication number	US20140266948 A1
Application number	US 13/801,041
Filing date	13 Mar 2013
Inventors	Graham Smith, Johannes McKay
Original Assignee	University Court Of The University Of St. Andrews

1.2. MATERIALS AND METHODS

1.2.1. CHAPTER 5

See Electronic Supplementary Information DOI: 10.1039/C5CP04753F .

1.2.2. CHAPTER 6

Protein expression and purification

All *E.coli* MscS single cysteine mutants were grown, expressed, purified and spin labeled with MTSL on the nickel affinity resin as previously described [60]. Wild type MscS was grown, expressed and purified in a similar way, omitting the spin labeling steps.

X-band measurements

The X-band PELDOR measurement on MscS D67R1 at 20 micromolar (85 microlitres) was conducted on a Bruker ELEXSYS E580 spectrometer, operating at approximately 9.8 GHz, with a dielectric ring resonator (ER 4118X-MD5) and a Bruker 400U second microwave source unit. The experiment was carried out at 50K. The video bandwidth was set to 20MHz. The four pulse, dead-time free, constant-time PELDOR sequence was applied [118], with the pump pulse frequency positioned at the center of the nitroxide spectrum; the frequency of the observer pulse was increased by 65 MHz. The first interpulse delay was 380 ns and the second interpulse delay was 3020 ns. The experiment repetition time was 3.06 ms, and 50 shots were taken at each time point. 2-step phase cycling was applied. Proton nuclear modulation averaging was used, which meant varying the first interpulse delay eight times and by 8 ns each time. The experiment took approximately 18 hours and 186 scans were collected.

Experiments to determine the phase memory time (Tm) were performed by measuring the intensity of a Hahn echo as it decayed with increasing inter-pulse delay. The pulses were applied at the centre of the nitroxide spectrum. The pulse sequence used was π /2- t1- π, where the π pulse was 32 ns and the initial time delay t_1 was 200 ns, in addition two-step phase cycling was employed. The inter-pulse delay was increased by 12 ns, which meant that the Hahn echo was detected at an increment of 24 ns, and the number of data points taken was 512, thus providing a time window of approximately 12 μs. The experiment repetition time was 3 ms and 50 shots were taken at each time point.

HiPER measurements

Pulsed EPR measurements were recorded using a home-built W-band EPR spectrometer (HiPER) using a non-resonant sample holder operating in reflection and induction mode, which has been described before [8].

Samples were deposited into an approximately 29 mm long 3 mm diameter fluorinated ethylene propylene (FEP) (Adtech Polymer Engineering Ltd). The liquid Helium flow cryostat (Oxford) containing the transmission waveguide and sample holder was precooled to 150K prior to sample loading. The sample deposited in a FEP tube was flash frozen in liquid Nitrogen before being transferred into the precooled sample holder. The use of FEP sample tubes, rather than quartz, helps to improve glassing of the sample by reducing thermally induced strain in the sample on freezing. This in turn reduces the interaction between the sample and the rf E-field, which is present in the sample holder configuration used in this spectrometer. Two pulse echo decay measurements were performed using π /2- τ- π sequence with 16ns π pulse length, starting delay τ_0 =200ns stepped in 20ns steps, 2ms shot repetition time and 401 data points. PELDOR experiments were conducted using the dead-time free 4 pulse variant based around refocused echo. The first delay τ_1 was set to 200ns and τ_2 was generally extended to the maximum time window yielding suitable signal to noise. The typical π pulse length used for the PELDOR experiments was 16ns for both probe and pump pluses. The shot repetition time was set to 2ms. The primary coherent oscillator was kept at 94 GHz and the secondary ELDOR oscillator was tuned to various offsets to achieve selection of different portions of the Rx spin label spectrum. The field was simultaneously tuned by the use of a ±1800 G sweep coil. All the experiments were conducted at 60K.